



THE HONG KONG
POLYTECHNIC UNIVERSITY

香港理工大學

Pao Yue-kong Library

包玉剛圖書館

Copyright Undertaking

This thesis is protected by copyright, with all rights reserved.

By reading and using the thesis, the reader understands and agrees to the following terms:

1. The reader will abide by the rules and legal ordinances governing copyright regarding the use of the thesis.
2. The reader will use the thesis for the purpose of research or private study only and not for distribution or further reproduction or any other purpose.
3. The reader agrees to indemnify and hold the University harmless from and against any loss, damage, cost, liability or expenses arising from copyright infringement or unauthorized usage.

IMPORTANT

If you have reasons to believe that any materials in this thesis are deemed not suitable to be distributed in this form, or a copyright owner having difficulty with the material being included in our database, please contact lbsys@polyu.edu.hk providing details. The Library will look into your claim and consider taking remedial action upon receipt of the written requests.

THE HONG KONG POLYTECHNIC UNIVERSITY

DEPARTMENT OF APPLIED PHYSICS

**STUDY OF BARIUM STRONTIUM ZIRCONATE
TITANATE THIN FILMS AND THEIR MICROWAVE
DEVICE APPLICATIONS**

CHAN Ngai Yui

A thesis submitted in partial fulfilment of the
requirements for the Degree of Master of Philosophy

August 2010



THE HONG KONG POLYTECHNIC UNIVERSITY

Certificate of Originality

I hereby declare that this thesis is my own work and that, to the best of my knowledge and belief, it reproduces no material previously published or written, nor material that has been accepted for the award of any other degree or diploma, except where due acknowledgement has been made in the text.

CHAN Ngai Yui (Vincent)



Abstract

Perovskites, in particular the family of barium titanate, have attracted much attention due to their moderate permittivity and high dielectric tunability. $(\text{Ba}, \text{Sr})\text{TiO}_3$ (BST) and $\text{Ba}(\text{Zr}, \text{Ti})\text{O}_3$ (BZT) materials are perovskite based ferroelectrics which have found extensive applications. For ABO_3 perovskite, substituting A and/or B sites by other ions can modify the dielectric behaviour of the material. $(\text{Ba}, \text{Sr})(\text{Zr}, \text{Ti})\text{O}_3$ (BSZT) is a solid solution of BST and BZT. It is expected that the addition of Zr and Sr into BaTiO_3 will result in a modified BSZT ceramics.

$(\text{Ba}_{1-x}, \text{Sr}_x)(\text{Zr}_{0.1}, \text{Ti}_{0.9})\text{O}_3$ ($x = 0, 0.05, 0.15, 0.25, 0.35, 0.45$) ceramics were prepared by a conventional solid state reaction method. The structure, surface morphology, dielectric and ferroelectric properties were investigated. With the increase in Sr content, the Curie temperature decreases linearly. From X-ray diffraction (XRD) analysis, the lattice parameters were found to reduce with the increase in Sr content. Scanning electron microscopy (SEM) was used to reveal the microstructure and it was observed that the grain size decreases with the increase in Sr content. The polarization-electric field loop (P-E loop) shows a decrease in remnant polarization with the increase in Sr content.

We have successfully grown BSZT thin films on different substrates [e.g. LaAlO_3 (LAO), $(\text{La}, \text{Sr})(\text{Al}, \text{Ta})\text{O}_3$ (LSAT), SrTiO_3 and MgO] with different compositions ($x = 0, 0.05, 0.15, 0.25, 0.35, 0.45$). The structure, dielectric and ferroelectric properties are studied. The properties are obtained using coplanar



THE HONG KONG POLYTECHNIC UNIVERSITY

configurations on BSZT thin films, as coplanar electrode is much preferable for microwave applications. Using conformal mapping techniques, dielectric constant values ranging from (180 to 800) are obtained. The in-plane dielectric tunabilities obtained are higher than 40%. Structural characterization shows that the lattice parameter reduces with increasing Sr content. Among all compositions, the Curie temperature of $(\text{Ba}_{0.55}\text{Sr}_{0.45})(\text{Zr}_{0.1}\text{Ti}_{0.9})\text{O}_3$ thin film is below room temperature (10°C), and smallest dielectric dissipation was obtained, giving high Q values. $(\text{Ba}_{0.55}\text{Sr}_{0.45})(\text{Zr}_{0.1}\text{Ti}_{0.9})\text{O}_3$ thin film was chosen as the base composition for microwave devices (ring resonators and phase shifters) fabrication.

Ring resonators are widely used microwave devices and also are tools for material characterization at high frequency (1GHz – 20GHz). Ring resonators have been used to characterize the dielectric properties of $(\text{Ba}_{0.55}\text{Sr}_{0.45})(\text{Zr}_{0.1}\text{Ti}_{0.9})\text{O}_3$ thin film on different substrates in the microwave region. Phase shifters produce various phase shifts in output signal. Ring resonator and coupled microstrip phase shifter (CMPS) have been fabricated on LAO, LSAT and MgO substrates using standard photolithography etching technique. It has been found that, under $12.5 \text{ V}/\mu\text{m}$ electric field, the phase shifter provides 60° of phase shift in the GHz region. This is a preliminary demonstration of the performance of the BSZT phase shifter. It is envisaged that by tuning some processing parameters, better results could be obtained.



List of Publications

1. N. Y. Chan, G. Y. Gao, Y. Wang and H. L. W. Chan, "Preparation and Characterization of $\text{Ba}(\text{Zr}, \text{Ti})\text{O}_3/(\text{Ba}, \text{Sr})\text{TiO}_3$ heterostructures grown on $(\text{LaAlO}_3)_{0.3}(\text{Sr}_2\text{AlTaO}_6)_{0.35}$ single crystal substrates by pulsed laser deposition," *Thin Solid Films*, 518 (2010) e82-e84.
2. N. Y. Chan, Y. Wang, H. L. W. Chan, "Barium strontium zirconate titanate $(\text{Ba},\text{Sr})(\text{Zr},\text{Ti})\text{O}_3$ thin films for tunable microwave applications" submitted to *Ferroelectrics*.
3. N. Y. Chan, S. H. Choy, Y. Wang, H. L. W. Chan, "Structural, dielectric and ferroelectric properties of $(\text{Ba}_{1-x},\text{Sr}_x)(\text{Zr}_{0.1}\text{Ti}_{0.9})\text{O}_3$ ceramics," submitted to *Current Applied Physics*.
4. G. Y. Gao, Y. Wang, Y. Jiang, L. F. Fei, N. Y. Chan, H. L. W. Chan and W. B. Wu, "Epitaxial growth and rectification characteristics of double perovskite oxide $\text{La}_2\text{NiMnO}_6$ films on Nb-SrTiO_3 single crystal substrates," *Thin Solid Films* (accepted).
5. D. Y. Wang, N. Y. Chan, S. Li, H. Y. Tian and H. L. W. Chan, "Enhanced ferroelectric and piezoelectric properties in doped lead-free $(\text{Bi}_{0.5}\text{Na}_{0.5})_{0.94}\text{Ba}_{0.06}\text{TiO}_3$ thin films," *Applied Physics Letters*, 97,212911 (2010).
6. D. Y. Wang, D. M. Lin, K. W. Kwok, N. Y. Chan, J. Y. Dai, S. Li, H. L. W. Chan, "Ferroelectric, piezoelectric and leakage current properties of $(\text{K}_{0.48}\text{Na}_{0.48}\text{Li}_{0.04})(\text{Nb}_{0.775}\text{Ta}_{0.225})\text{O}_3$ thin films grown by pulsed laser deposition," *Applied Physics Letters*, 98,022902 (2011).



Acknowledgements

First and foremost, I would like to express my sincere gratitude to my supervisors, Prof. H. L. W. Chan and Dr. Y. Wang, for their guidance, encouragement and supervision. I am thankful for their patience and perseverance in teaching me the intricacies of being a good researcher. I would like to thank Prof. K.H. Wong, Prof. S.P. Lau, Dr J.Y. Dai and Dr. C.W. Leung in their assistance for my research and coursework studies.

None of my accomplishments would have been possible without the help and supports of my colleagues. I got a chance to work in a great group with experienced seniors, who provide invaluable supports and suggestions.

My genuine thanks go to Dr. D. Y. Wang, despite he is working in Australia, he spent lots of time with me in discussions and gave me advices in preparing thin films, photolithography and dielectric measurements. Thanks are also give to Dr. S. H. Choy for his assistance in ceramics fabrication, to Dr. G. Y. Gao for his assistance in thin film deposition and XRD measurements, to Dr. P. F. Lee for his helpful advices in laser operation and to Dr. Y. M. Hu for teach me the AFM operations.

I wish to thank Mr. M. N. Yeung of the Materials Research Centre for his assistance in equipment operation and Mr. C. S. Lo for teaching me the operating procedures for SEM investigations.



THE HONG KONG POLYTECHNIC UNIVERSITY

I am grateful to all my friends and colleagues in AP for their help and assistance. They include Mr. C. Y. Lo, Mr. Y. Jiang, Mr. H. F. Wong, Miss W. F. Ng, Mr. Y. Y. Hui, Mr. H. K. Lau and Mr. K. Au.

I gratefully acknowledge the financial support from the Department of Applied Physics and the Centre for Smart Materials of the Hong Kong Polytechnic University.

Last but not least, I would like to thank my parents, for their love, support and patience that inspired me to continue my study.



Table of Contents

Certificate of Originality	i
Abstract	ii
List of Publications	iv
Acknowledgements	v
Table of Contents	vii
List of Figures	xi
List of Tables	xviii
List of Acronyms	xx
CHAPTER 1 Introduction And Literature Review	21
1.1 Background	21
1.2 Introduction to ferroelectricity	21
1.3 Relative permittivity of ferroelectrics	23
1.4 Phase transition in ferroelectrics	26
1.5 Dielectric models of the ferroelectric and paraelectric phase	28
1.6 Polarization mechanisms	30
1.7 Structure and properties of BSZT	34
1.7.1 Bulk materials	34
1.7.2 BSZT thin films	36
1.8 Substrates for microwave devices	40
1.9 Frequency agile technologies	43
1.10 Scope of the project	52
CHAPTER 2 Fabrication and Characterization of Barium Strontium Zirconate Titanate Ceramics	54



THE HONG KONG POLYTECHNIC UNIVERSITY

2.1	Introduction	54
2.2	Fabrication of barium strontium zirconate titanate ceramics	55
2.2.1	Preparation of BSZT ceramics	55
2.2.2	Poling procedures	57
2.3	Characterization of BSZT ceramics	57
2.3.1	Density measurement	57
2.3.2	X-ray diffraction and microstructural analysis	59
2.3.3	Dielectric properties	62
2.3.4	Ferroelectric hysteresis loop measurement	66
2.3.5	Piezoelectric properties	69
2.3.6	Tunability measurements	72
2.4	Summary	77
CHAPTER 3 Techniques For Deposition And Structural Characterization Of BSZT		
	Thin Films	79
3.1	Introduction	79
3.2	Deposition of BSZT thin films	80
3.2.1	PLD system and setup	80
3.2.2	Thin film growth modes	84
3.2.3	Deposition of BSZT thin films	85
3.3	Structural characterization of BSZT thin films by X-Ray diffraction	86
3.3.1	X-Ray diffraction	86
3.3.2	Compositional dependence	92
3.3.3	Effect of different substrates	101
3.4	Investigation of surface morphology by atomic force microscopy	107
3.4.1	Atomic force microscopy	107



THE HONG KONG POLYTECHNIC UNIVERSITY

3.4.2	Compositional dependence	109
3.4.3	Effect of different substrates	110
3.5	Summary	113
CHAPTER 4 Barium Strontium Zirconate Titanate Thin Film Characterization		114
4.1	Introduction	114
4.2	Electrode patterning of the BSZT thin films	115
4.2.1	Electrode deposition, photolithography, IDC geometry and extraction of relative permittivity of the film	115
4.2.1.1	Electrode deposition	115
4.2.1.2	Photolithography	116
4.2.1.3	IDC geometry	120
4.2.1.4	Capacitor configurations: parallel plate vs coplanar	120
4.3	Measurement of relative permittivity of BSZT thin films	122
4.3.1	Permittivity as a function of temperature	122
4.3.1.1	Effect of compositions	122
4.3.1.2	Effect of substrates	125
4.3.2	Permittivity as a function of frequency	127
4.3.2.1	Effect of compositions	128
4.3.2.2	Effect of substrates	130
4.3.3	Dielectric tunability of the BSZT thin films	130
4.3.3.1	Effect of compositions	131
4.3.3.2	Effect of substrates	136
4.3.4	Hysteresis measurements	137
4.3.4.1	Effect of compositions	138
4.3.4.2	Effect of substrates	139



THE HONG KONG POLYTECHNIC UNIVERSITY

4.3.5	Summary	140
CHAPTER 5 Barium Strontium Zirconate Titanate Thin Films Based Microwave		
	Devices	142
5.1	Introduction	142
5.2	S-parameters	143
5.3	Issues of microwave measurements	145
5.3.1	Calibration of the system	146
5.4	Microwave characterization of the $(\text{Ba}_{0.55}\text{Sr}_{0.45})(\text{Zr}_{0.1}\text{Ti}_{0.9})\text{O}_3$ thin film on different substrates	147
5.5	$(\text{Ba}_{0.55}\text{Sr}_{0.45})(\text{Zr}_{0.1}\text{Ti}_{0.9})\text{O}_3$ thin film based ring resonators on different substrates	150
5.5.1	Theory	151
5.5.2	Ring resonators on different substrates	153
5.6	$(\text{Ba}_{0.55}\text{Sr}_{0.45})(\text{Zr}_{0.1}\text{Ti}_{0.9})\text{O}_3$ thin film based phase shifters on different substrates	158
5.6.1	Introduction	158
5.6.2	Device structures and basic principle	160
5.6.3	Phase shifters on different substrates	163
5.7	Conclusion	165
CHAPTER 6 Conclusions and Suggestions For Future work		
6.1	Conclusions	167
6.2	Suggestions for Future Work	170
References		172



List of Figures

Figure1.1	Crystal structures of symmetry crystal point groups (Gonzalo and Jiménez 2005).	22
Figure1.2	Structure of BaTiO ₃ .	25
Figure1.3	(a) Cubic structure and (b) tetragonal structure.	26
Figure1.4	Phase transitions of BaTiO ₃ at different temperatures (Murata).	27
Figure1.5	2 nd order paraelectric to ferroelectric phase transition. (a) Temperature dependences of the polarization and inverse permittivity, and (b) the polarization dependent free energy (Uchino 2000).	30
Figure1.6	Polarization (a and c) and permittivity (c and d) dependences on the applied electric field for ferroelectric (a and c) and paraelectric (b and d) (Uchino 2000).	31
Figure1.7	Curie temperature of (a) (Ba _{1-x} Sr _x)TiO ₃ and (b) Ba(Zr _x Ti _{1-x})O ₃ with different compositions (Springer-Verlag 2001).	35
Figure1.8	The electromagnetic spectrum for different frequency bands and the corresponding applications (SURA).	45
Figure1.9	Real and complex permittivities contribution from different polarization mechanism as a function of frequency (PeterP).	46
Figure2.1	Density measurement of the (Ba _{1-x} Sr _x)(Zr _{0.1} Ti _{0.9})O ₃ (x = 0, 0.05, 0.15, 0.25, 0.35, 0.45) ceramics.	58
Figure2.2	Schematic diagram of X-ray diffraction in crystal.	59
Figure2.3	(a) X-Ray diffraction pattern of BSZT ceramics with different amounts of Sr content and (b) X-Ray diffraction pattern of	



	BSZT ceramics (110) peak with different amounts of Sr content.	61
Figure2.4	(a) – (e) SEM micrographs of BSZT ceramics with different concentrations of Sr. (a) $x = 0$, (b) $x = 0.15$, (c) $x = 0.25$, (d) $x = 0.35$, (e) $x = 0.45$.	63
Figure2.5	Temperature dependence of (a) relative permittivity and (b) dielectric loss measured at 1kHz.	65
Figure2.6	Dielectric constant and dielectric loss $\tan \delta$ of the BSZT ceramics measured at 1kHz.	66
Figure2.7	A schematic diagram of the Sawyer-Tower bridge for the hysteresis loop measurement (Sawyer and Tower 1930).	67
Figure2.8	P-E hysteresis loops of the $(\text{Ba}_{1-x}, \text{Sr}_x)(\text{Zr}_{0.1}, \text{Ti}_{0.9})\text{O}_3$ ceramics at room temperature measured at 100Hz.	68
Figure2.9	Schematic diagram of a d_{33} meter.	70
Figure2.10	Piezoelectric constant d_{33} and planar electromechanical coupling factor k_p of the BSZT ceramics.	72
Figure2.11	Schematic diagram of tunability measurements.	74
Figure2.12	Dielectric constant as a function of DC biased electric field of $(\text{Ba}_{1-x}, \text{Sr}_x)(\text{Zr}_{0.1}, \text{Ti}_{0.9})\text{O}_3$ ceramics at room temperature measured at 100kHz.	75
Figure3.1	Schematic diagram of the pulsed laser deposition system.	83
Figure3.2	Thin film growth mode: (i) Volmer-Weber growth, (ii) Frank-van der Merme mode and (iii) Stranski-Krastinov growth mode (Waser 2005).	84
Figure3.3	Layout of the X-ray diffractometer.	87
Figure3.4	Schematic of Bragg- Brentano diffractometer (Cullity 1956).	88



- Figure3.5 XRD θ - 2θ scan pattern of $(\text{Ba}_{0.55},\text{Sr}_{0.45})(\text{Zr}_{0.1},\text{Ti}_{0.9})\text{O}_3$ thin film grown on LSAT(001) at 700°C under an oxygen partial pressure of 200mTorr. 89
- Figure3.6 The out-of-plane lattice parameter of $(\text{Ba}_{0.55},\text{Sr}_{0.45})(\text{Zr}_{0.1},\text{Ti}_{0.9})\text{O}_3$ thin film grown on LSAT(001) substrate fitted to the Nelson-Riley function. 90
- Figure3.7 XRD θ - 2θ scan pattern of $(\text{Ba}_{1-x},\text{Sr}_x)(\text{Zr}_{0.1},\text{Ti}_{0.9})\text{O}_3$ thin film grown on LSAT(001) under the conditions listed in Table 4.1. (a) $x = 0$, (b) $x = 0.05$, (c) $x = 0.15$, (d) $x = 0.25$, (e) $x = 0.35$, (f) $x = 0.45$ (inset: ω - scan of the thin films). 95
- Figure3.8 XRD θ - 2θ scan patterns of $(\text{Ba}_{1-x},\text{Sr}_x)(\text{Zr}_{0.1},\text{Ti}_{0.9})\text{O}_3$ thin film grown on LSAT(001) substrates. 96
- Figure3.9 XRD θ - 2θ scan pattern of $(\text{Ba}_{1-x},\text{Sr}_x)(\text{Zr}_{0.1},\text{Ti}_{0.9})\text{O}_3$ thin film grown on LSAT(001) substrates with $\chi=45^\circ$. 97
- Figure3.10 Tetragonality a/c and unit cell volume a^2c of BSZT thin films deposited on LSAT(001) substrates as a function of Sr content 99
- Figure3.11 Off axis ϕ scan of the (202) diffraction of BSZT thin films deposited LSAT(001) substrates. 100
- Figure3.12 XRD θ - 2θ scan pattern of $(\text{Ba}_{0.55},\text{Sr}_{0.45})(\text{Zr}_{0.1},\text{Ti}_{0.9})\text{O}_3$ grown on LAO(001) substrate. 103
- Figure3.13 Off axis ϕ scan of the (202) diffraction of $(\text{Ba}_{0.55},\text{Sr}_{0.45})(\text{Zr}_{0.1},\text{Ti}_{0.9})\text{O}_3$ thin films deposited on LAO(001) substrate. 103
- Figure3.14 XRD θ - 2θ scan pattern of $(\text{Ba}_{0.55},\text{Sr}_{0.45})(\text{Zr}_{0.1},\text{Ti}_{0.9})\text{O}_3$ grown on LSAT(001) substrate. 104



- Figure3.15 Off axis ϕ scan of the (202) diffraction of $(\text{Ba}_{0.55},\text{Sr}_{0.45})(\text{Zr}_{0.1},\text{Ti}_{0.9})\text{O}_3$ thin films deposited on LSAT(001) substrate. 104
- Figure3.16 XRD θ - 2θ scan pattern of $(\text{Ba}_{0.55},\text{Sr}_{0.45})(\text{Zr}_{0.1},\text{Ti}_{0.9})\text{O}_3$ grown on MgO(001) substrate. 105
- Figure3.17 Off axis ϕ scan of the (202) diffraction of $(\text{Ba}_{0.55},\text{Sr}_{0.45})(\text{Zr}_{0.1},\text{Ti}_{0.9})\text{O}_3$ thin films deposited on MgO(001) substrate. 105
- Figure3.18 Experimental setup of AFM (wikipedia). 107
- Figure3.19 Surface morphology of BSZT thin film deposited on LSAT (001) single crystal substrate. (a) $x = 0$, (b) $x = 0.15$, (c) $x = 0.45$. 110
- Figure3.20 Surface morphology of $(\text{Ba}_{0.55},\text{Sr}_{0.45})(\text{Zr}_{0.1},\text{Ti}_{0.9})\text{O}_3$ thin film deposited on LSAT substrate. 111
- Figure3.21 Surface morphology of $(\text{Ba}_{0.55},\text{Sr}_{0.45})(\text{Zr}_{0.1},\text{Ti}_{0.9})\text{O}_3$ thin film deposited on LAO substrate. 112
- Figure3.22 Surface morphology of $(\text{Ba}_{0.55},\text{Sr}_{0.45})(\text{Zr}_{0.1},\text{Ti}_{0.9})\text{O}_3$ thin film deposited on MgO substrate. 112
- Figure4.1 Schematic diagram of magnetron sputtering setup. In this system, the power supply can be either RF or DC. The cooling system is to prevent the target from overheating. 116
- Figure4.2 Process flow of the photolithographic technique. 119
- Figure4.3 Steps for fabricating pattern by photolithography. 119
- Figure4.4 Schematic diagram showing the interdigital capacitor (IDC) used for dielectric and hysteresis measurement. 120
- Figure4.5 (a) Parallel plate capacitor, and (b) coplanar capacitor. 121



- Figure4.6 Temperature dependence of the relative permittivity of BSZT thin films on LSAT measured using IDC. 123
- Figure4.7 Temperature dependence of the relative permittivity of BSZT thin film on LSAT. 124
- Figure4.8 Relative permittivity as a function of temperature of $(\text{Ba}_{0.55}, \text{Sr}_{0.45})(\text{Zr}_{0.1}, \text{Ti}_{0.9})\text{O}_3$ thin films deposited at 700°C on LAO and MgO substrates. 127
- Figure4.9 Frequency dependence of the relative permittivity ϵ and loss tangent of $(\text{Ba}_{1-x}\text{Sr}_x)(\text{Zr}_{0.1}\text{Ti}_{0.9})\text{O}_3$ ($x = 0, 0.05, 0.15, 0.25, 0.35, 0.45$) thin films. 128
- Figure4.10 Frequency dependence of the in-plane relative permittivity and loss tangent of $(\text{Ba}_{0.55}, \text{Sr}_{0.45})(\text{Zr}_{0.1}, \text{Ti}_{0.9})\text{O}_3$ thin films on different substrates 131
- Figure4.11 Relative permittivity as a function of electric field for $(\text{Ba}_{1-x}\text{Sr}_x)(\text{Zr}_{0.1}\text{Ti}_{0.9})\text{O}_3$ ($x = 0, 0.05, 0.15, 0.25, 0.35, 0.45$) grown on LSAT. 133
- Figure4.12 The frequency dependence of dielectric tunability $K(\%)$ of the BSZT thin films under 20MV/m. 135
- Figure4.13 Figure of merit (FOM) as a function of compositions in $(\text{Ba}_{1-x}\text{Sr}_x)(\text{Zr}_{0.1}\text{Ti}_{0.9})\text{O}_3$ ($x = 0, 0.05, 0.15, 0.25, 0.35, 0.45$) thin films. 136
- Figure4.14 Dielectric tunability as a function of electric field for $(\text{Ba}_{0.55}\text{Sr}_{0.45})(\text{Zr}_{0.1}\text{Ti}_{0.9})\text{O}_3$ thin films grown on LAO and MgO. 137
- Figure4.15 Hysteresis loops of $(\text{Ba}_{1-x}\text{Sr}_x)(\text{Zr}_{0.1}\text{Ti}_{0.9})\text{O}_3$ ($x = 0, 0.05, 0.15, 0.25, 0.35, 0.45$) thin films. 138



Figure4.16	Hysteresis loop of $(\text{Ba}_{0.55}\text{Sr}_{0.45})(\text{Zr}_{0.1}\text{Ti}_{0.9})\text{O}_3$ thin films on LSAT, MgO and LAO substrates.	140
Figure5.1	Two port electrical network.	144
Figure5.2	Information of S-parameters.	144
Figure5.3	Photographs of (a) GSG probe tips, (b) GSG probes, (c) Schematic of GSG probes (C.Doan).	146
Figure5.4	Different calibration steps: Microprobes placed on different ISS (C.Doan).	146
Figure5.5	Quality factor contributions from substrate, metal and dielectrics as a function of frequency.	149
Figure5.6	Quality factor of the $(\text{Ba}_{0.55}\text{Sr}_{0.45})(\text{Zr}_{0.1}\text{Ti}_{0.9})\text{O}_3$ thin film on different substrates.	150
Figure5.7	Schematic diagram of a ring resonator.	152
Figure5.8	Electric field distribution on the ring resonator (Liu et al. 2004).	152
Figure5.9	Transmission coefficient S_{21} as a function of frequency for the ring resonator on LAO substrate.	154
Figure5.10	Transmission coefficient S_{21} as a function of frequency for the ring resonator on LSAT substrate.	154
Figure5.11	Transmission coefficient S_{21} as a function of frequency for the ring resonator on MgO substrate.	155
Figure5.12	Simulation and measured result for BSZT thin film on LAO substrates.	157
Figure5.13	Simulation and measured result for BSZT thin film on LSAT substrates.	157
Figure5.14	Simulation and measured result for BSZT thin film on MgO	



- substrates. 158
- Figure5.15 Schematic diagram of eight elements phase shifter.
($W=25 \mu\text{m}$: $s=8 \mu\text{m}$) (Keuls et al. 1999). 161
- Figure5.16 Cross section of the coupled microstripline phase shifter
showing the odd mode configuration. The thickness of the
ferroelectric layer is h_1 , while the host substrate has thickness h_2 161
- Figure5.17 Measured S_{21} phase of the BSZT thin film based phase shifters
on LSAT as a function of frequency, with two different applied
biased voltages. 163
- Figure5.18 Measured S_{21} phase of the BSZT thin film based phase shifters
on LAO as a function of frequency, with two different applied
biased voltages. 164
- Figure5.19 Measured S_{21} phase of the BSZT thin film based phase shifters
on MgO as a function of frequency, with two different applied
biased voltages. 164



List of Tables

Table1.1	Literature survey on BSZT thin films.	38
Table1.2	List of different substrates (Crystec).	42
Table1.3	Comparison between different technology for agile devices (Gevorgian 2009).	47
Table2.1	Lattice constants of BSZT ceramics.	62
Table2.2	List of Curie temperature, remnant polarization, and coercive field of BSZT ceramics.	69
Table2.3	List of the tunability of BSZT ceramics under 20kV/cm.	74
Table2.4	Lattice parameter, Curie transition temperature, remnant polarization, coercive field, tunability, dielectric loss, figure of merit, d_{33} and planar electromechanical coefficient k_p .	78
Table3.1	Deposition conditions of $(Ba_{1-x},Sr_x)(Zr_{0.1},Ti_{0.9})O_3$ thin films by pulsed laser deposition.	86
Table3.2	Lattice parameters of the $(Ba_{1-x},Sr_x)(Zr_{0.1},Ti_{0.9})O_3$ thin film grown on LSAT(001) substrates (with $\chi = 45^\circ$).	98
Table3.3	Lattice parameters of thin films, un-relaxed lattice misfit and actual in-plane lattice misfit strain on various substrates at room temperature.	106
Table3.4	Average grain size of the $(Ba_{1-x},Sr_x)(Zr_{0.1},Ti_{0.9})O_3$ thin film grown on LSAT substrates.	109
Table3.5	Average grain size and roughness of the $(Ba_{0.55},Sr_{0.45})(Zr_{0.1},Ti_{0.9})O_3$ thin film grown on different substrates.	113



Table4.1	Deposition conditions for Au sputtering.	116
Table4.2	Transition temperature of $(\text{Ba}_{1-x}\text{Sr}_x)(\text{Zr}_{0.1}\text{Ti}_{0.9})\text{O}_3$ ($x = 0, 0.05, 0.15, 0.25, 0.35, 0.45$) thin films and bulk ceramics measured at 1kHz.	124
Table4.3	Tunability, loss tangent and figure of merit for $(\text{Ba}_{1-x}\text{Sr}_x)(\text{Zr}_{0.1}\text{Ti}_{0.9})\text{O}_3$ ($x = 0, 0.05, 0.15, 0.25, 0.35, 0.45$) grown on LSAT.	135
Table4.4	The remnant polarization P_r and coercive field E_c of $(\text{Ba}_{1-x}\text{Sr}_x)(\text{Zr}_{0.1}\text{Ti}_{0.9})\text{O}_3$ with ($x = 0, 0.05, 0.15, 0.25, 0.35, 0.45$) thin films.	139
Table4.5	Remnant polarization P_r and coercive field E_c of the $(\text{Ba}_{0.55}\text{Sr}_{0.45})(\text{Zr}_{0.1}\text{Ti}_{0.9})\text{O}_3$ on different substrates.	140
Table5.1	Dimensions of the ring resonators	153
Table5.2	Resonant frequencies on different substrates.	156
Table5.3	List of operating frequency, phase shift and insertion loss of the phase shifters on different substrates.	165



List of Acronyms

<u>Acronyms</u>	<u>Description</u>
BTO	Barium titanate, BaTiO ₃
BST	Barium strontium titanate (Ba Sr) TiO ₃
BZT	Barium zirconate titanate Ba (Zr Ti)O ₃
BSZT	Barium strontium zirconate titanate (Ba Sr)(Zr Ti)O ₃
XRD	X-ray diffraction
FWHM	Full width at half maximum
SPM	Scanning probe microscopy
AFM	Atomic force microscopy
SEM	Scanning electron microscopy
rms	Root mean square
LSAT	Lanthanum strontium aluminate tantalate, (LaAlO ₃) _{0.3} (Sr ₂ AlTaO ₆) _{0.35}
LAO	Lanthanum aluminate, LaAlO ₃
PLD	Pulsed laser deposition
MOCVD	Metal organic chemical vapour deposition
MBE	Molecular beam epitaxy
IDC	Interdigital capacitor
rf	Radio frequency
DUT	Device under test
SOLT	Short-open-load-through
MW	Microwave
UV	Ultraviolet



CHAPTER 1

INTRODUCTION AND LITERATURE REVIEW

1.1 Background

Ferroelectrics, especially complex oxides with perovskite structure, are truly multifunctional materials. The physical properties (relative permittivity, remnant polarization, refractive index, magnetic permeability, etc) of these materials change significantly with temperature, external electrical, magnetic field, especially at temperature near phase transitions (multi phase boundaries), which makes them very attractive for many applications.

Study of the piezoelectricity and ferroelectricity continues extensively, leading to many theoretical and experimental results. There are numerous area of applications, including memory (Gerblinger and Meixner 1990; Cheng 1996; Wu et al. 1996; Qin et al. 2002), transducers (Saito et al. 2004), sensors (Watton and Manning 1998), capacitors (Jaffe et al. 1971; Shaw et al. 1999; Moulson and Herbert 2003) and microwave devices (Kim et al. 2000; Yoon et al. 2002; Cole et al. 2003).

The following Section gives a brief overview of the theory of ferroelectricity, starting by considering the crystal structure.

1.2 Introduction to ferroelectricity

Ferroelectricity is defined as the property of a material to exhibit a spontaneous polarization, which can be reversed by the application of an external electric field

THE HONG KONG POLYTECHNIC UNIVERSITY

(Uchino 2000). Ferroelectrics have two states, polar (ferroelectric, antiferroelectric) or nonpolar (paraelectric). The properties of ferroelectrics under polar and nonpolar state should be studied carefully for real life applications.

The crystal ordering in a lattice, i.e. the symmetry, of a crystal affects both the structural and physical properties. A diagram of different crystal point groups is shown in Figure 1.1.

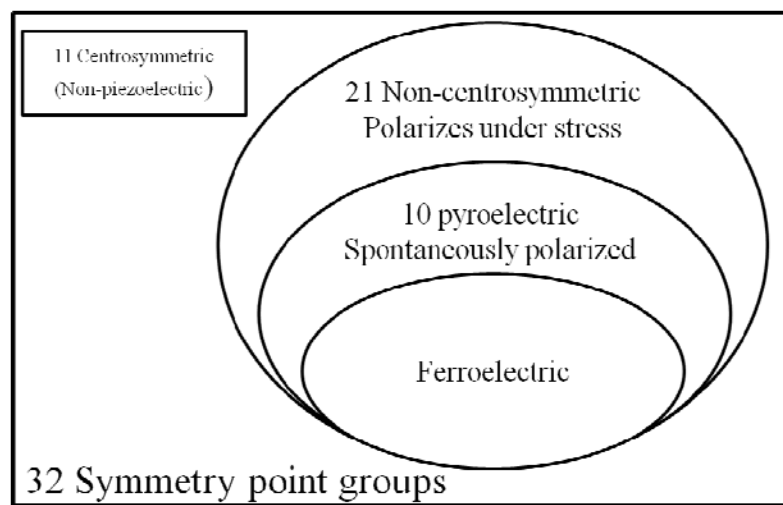


Figure 1.1 Crystal structures of symmetry crystal point groups (Gonzalo and Jiménez 2005).

Consider the 32 crystal classes shown in Figure 1.1, the group can be divided into two categories: centrosymmetric and non-centrosymmetric.

Within the 32 symmetry point groups, 11 of them are centrosymmetric and possess no polarity, which means they lack an inversion center. 21 of them are non centrosymmetric. Non-centrosymmetric materials possess one or more crystallographically unique axes, which is a condition required for piezoelectricity. Within the 21 non-centrosymmetric point groups, 20 of them show piezoelectric effect. The point group 432 is the lone non-centrosymmetric material that is not piezoelectric



THE HONG KONG POLYTECHNIC UNIVERSITY

due to combination of other symmetry elements.

A sub group of non-centrosymmetric point group shows the pyroelectric effect. These 10 crystal classes have only one unique rotation axis and do not have a mirror perpendicular to that axis, which lead them to being referred to as polar materials as well.

These materials possess the unique property to exhibit a remnant polarization. Within this material class are the ferroelectric materials which have permanent electrical dipoles that can be reversed by an electric field.

1.3 Relative permittivity of ferroelectrics

The electric displacement field \vec{D} is a vector field which describes the displacement effects of an electric field on the charges within a dielectric material, it can be expressed as:

$$\vec{D} = \epsilon_0 \vec{E} + \vec{P} \quad (1.3.1)$$

where ϵ_0 is the permittivity of free space, \vec{E} the applied electric field, and \vec{P} is the polarization density of the electric material.

The application of an electric field results in a finite displacement of the positive and negative charges forming electric dipoles. Polarization is considered as the rearrangement of electrical charges under the presence of an external electrical field.

The net polarization can be written in terms of susceptibility as:

$$\vec{P}(E) = \epsilon_0 \chi \vec{E} \quad (1.3.2)$$

Where χ is the dielectric susceptibility.



THE HONG KONG POLYTECHNIC UNIVERSITY

From Eq. (1.3.1), the relative permittivity can be defined in terms of the susceptibility that is directly related to the polarization mechanisms in a material.

$$\vec{D} = \varepsilon_0(1 + \chi)\vec{E} = \varepsilon_0\varepsilon_r\vec{E} \quad (1.3.3)$$

The dielectric constant of a material is dependent on the frequency at which the material is probed. As mentioned earlier, different polarization mechanisms are active at different frequency ranges, and thus the permittivity is intimately related to the associated polarization mechanism within a material, the dielectric constant is then treated in complex form, which is dependent on the frequency (ω).

$$\varepsilon_r(\omega) = \varepsilon_r'(\omega) - j\varepsilon_r''(\omega) = \varepsilon_r'(1 - j \tan\delta) \quad (1.3.4)$$

where

$$\varepsilon_r'(\omega) = \varepsilon_\infty + \frac{\varepsilon_s - \varepsilon_\infty}{1 + \tau^2 \omega^2} \quad (1.3.5)$$

And

$$\varepsilon_r''(\omega) = (\varepsilon_s - \varepsilon_\infty) \frac{\omega \tau}{1 + \tau^2 \omega^2} \quad (1.3.6)$$

where ε_s is denoted as static permittivity.

The real part of the permittivity (ε_r') is the relative permittivity and is determined by the amount of polarization. It determines the amount of electrostatic energy stored per unit volume in a material for a given applied field. i.e. The amount of charge stored in the capacitor. The imaginary component of the permittivity (ε_r'') is called the loss factor and is governed by the phase lag between polarization and the applied field and determines the energy dissipation associated with charge polarization. It represents the energy loss in a material (heat). This energy loss appears as an attenuation of the applied field and is usually measured relative to the dielectric constant in terms of loss tangent.

$$\tan\delta = \frac{\varepsilon_r''}{\varepsilon_r'} \quad (1.3.7)$$

In terms of an equivalent electrical circuit, $\tan\delta$ represents the resistive part of the impedance and is directly proportional to the electrical conductivity. For most dielectrics, the loss angles are very small and nearly constant over a wide range of frequencies. For this reason the loss tangent $\tan\delta$ is usually quoted as a figure of merit of a capacitor. For tunable device applications, the dielectric quality factor Q can be defined as $Q=(1/\tan\delta)$.

From Figure 1.1, the ferroelectric materials can be further divided into several categories. The most technologically important one is the perovskite type, ABO_3 . A schematic diagram of a typical perovskite crystal, barium titanate, $BaTiO_3$ is shown in Figure 1.2.

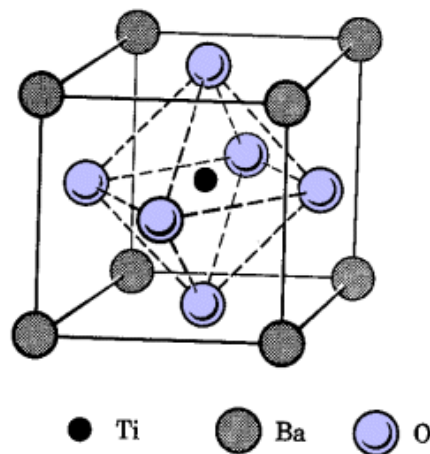


Figure 1.2 Structure of $BaTiO_3$.

A perovskite structure belongs to the space group P_m3_m . The crystal structure is commonly consisted of three species as referred by the chemical notation. Where valence of 1,2 or 3 and valence 3,4 or 5 cation species occupy the A sites and B sites respectively. The O sites are occupied by valence 2 anions. Conventional representation of the perovskite structure has the B sites located in the middle of the

THE HONG KONG POLYTECHNIC UNIVERSITY

cell and surrounded by oxygen octahedral, while the A sites sit in the corners of the cell. The depiction is useful for visualizing the effects of changing the cation radii size of A site on the crystal structure. Assuming a given radius for the B site, there is a given A site radii size which allows for the structure to be cubic. However if the A sites are substituted with larger cations, then the cell structure will shift to a tetragonal structure in order to accommodate the larger species. With the tetragonal distortion, the ion occupying the B-site is forced to move along the elongated axis, which creates a net polarization relative to the oxygen octahedral. The schematic diagrams of cubic and tetragonal perovskite structures are shown in Figures 1.3 (a) and (b).

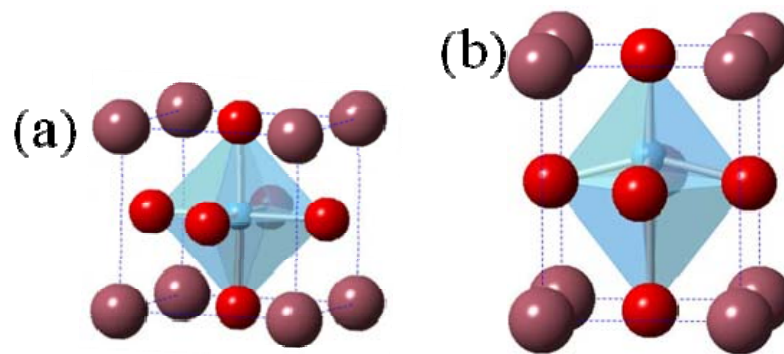


Figure 1.3 (a) Cubic structure and (b) tetragonal structure.

1.4 Phase transition in ferroelectrics

The complex metal oxide ferroelectrics, i.e. perovskites such as titanates (CaTiO_3 , BaTiO_3 etc), tantalites (KTaO_3 etc), niobates (KNbO_3 etc) are characterized by a common chemical formulae, ABO_3 , and have the same crystal structure. Above the polar-to-non polar phase transition temperature their crystal lattice has a cubic structure. In this phase the crystal has no spontaneous polarization. Its permittivity is rather high, and is DC field, temperature and strain dependent.

Below the phase transition temperature the crystal lattice becomes non-cubic, non-centro-symmetric, the centers of the positive and negative charges per unit cell shift and the crystal is characterized by spontaneous polarization. One of the surfaces of a macroscopic crystal is charged positively, while the opposite surface is charged negatively.

The transition temperature from cubic to tetragonal structure is commonly referred to as the Curie temperature T_c . In most case, when the temperature of the material is above T_c , a cubic structure is observed and it does not exhibit ferroelectricity, but, if the temperature is below T_c , the crystal becomes tetragonal and ferroelectricity is observed. In the cubic phase, the material is paraelectric. The characteristic of a paraelectric phase in a ferroelectric material is the absence of spontaneous polarization. If a material exhibits multiple phase transitions, the Curie temperature corresponds to the temperature at which the paraelectric – ferroelectric phase transition occurs. Figure 1.4 shows the phase transition of BaTiO_3 .

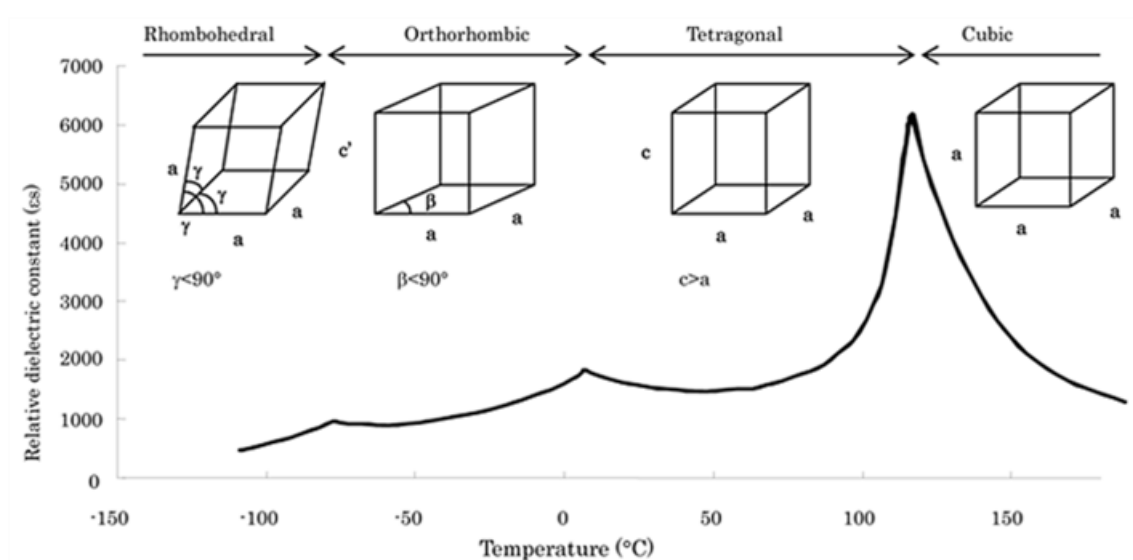


Figure 1.4 Phase transitions of BaTiO_3 at different temperatures (Murata).



1.5 Dielectric models of the ferroelectric and paraelectric phase

Based on the expansion of the free energy of a ferroelectric crystal as a function of polarization P . (Tagantsev 2005)

$$F(P, T) = \frac{1}{2}\alpha P^2 + \frac{1}{4}\beta P^4 + \dots \quad (1.5.1)$$

The higher order terms in this expansion are ignored. It contains only even terms to reflect the fact the free energy of the crystal does not depend on the polarization reversal. The physical meanings of the dielectric permittivity and nonlinear coefficients α and β are described below. Notice that this relationship holds true both for ferroelectric and paraelectric (polar) phases. The first derivative of this function is:

$$\frac{\partial F(P, T)}{\partial P} = E = \alpha P + \beta P^3 + \dots \quad (1.5.2)$$

From the simple relationship between the electric field and polarization it becomes clear that the coefficient α should have a meaning of the inverse permittivity $\alpha = \frac{1}{\epsilon \epsilon_0}$, where ϵ is the relative dielectric permittivity and ϵ_0 is the dielectric constant of vacuum. Furthermore, taking into account the experimentally observed temperature dependence of the permittivity, i.e. the Curie-Weiss law $\epsilon = \frac{C}{T - T_{ph}}$ the coefficient α takes the form:

$$\alpha = \frac{T - T_{ph}}{\epsilon_0 C} \quad (1.5.3)$$

C is the Curie constant and the temperature T_{ph} is equal or lower than the Curie temperature T_c . Its meaning will be clarified below.

In polar (ferroelectric) phase the spontaneous polarization P_s is found when the



THE HONG KONG POLYTECHNIC UNIVERSITY

externally applied electric field $E=0$, i.e. from the equation, $\alpha P_s + \beta P_s^3 = P_s(\alpha + \beta P_s^2) = 0$. The last equation has two solutions: $P_s=0$ and $\alpha + \beta P_s^2 = 0$. From the second equation, P_s can be derived.

$$P_s = \sqrt{\frac{T_{ph} - T}{\beta \epsilon_0 C}} \quad (1.5.4)$$

Which is valid below temperature $T=T_{ph}$. At $T=T_{ph}$ the spontaneous polarization $P_s=0$, i.e. T_{ph} is the phase transition temperature. Below this temperature the ferroelectric is in polar (ferroelectric) phase with $P=P_s$. Above T_{ph} , the ferroelectric is in paraelectric phase with $P_s=0$. In this case the paraelectric to ferroelectric phase transition is of the second order and the phase transition temperature is identical with the Curie Weiss temperature $T_c=T_{ph}$.

$$\epsilon = \frac{1}{\epsilon_0} \frac{\partial E}{\partial P} = \frac{1}{\epsilon_0(\alpha + 3\beta P^2)} \quad (1.5.5)$$

In paraelectric ($T>T_c=T_{ph}$) phase, and without external electric field, i.e $P=0$, from the equation, one gets the Curie Weiss law:

$$\epsilon = \frac{C}{T - T_c} \quad (1.5.6)$$

For ferroelectric, polar phase ($T<T_c=T_{ph}$) the permittivity is found from

$$\epsilon = \frac{C}{2(T_c - T)} \quad (1.5.7)$$

The temperature dependences of the spontaneous polarization and inverse permittivity for a ferroelectric crystal with 2nd order phase transition, defined by Eqs. (1.5.4), (1.5.6) and (1.5.7) are depicted in Figure 1.5(a). Figure 1.5(b) depicts the dependences of the free energy on the polarization Eq.(1.5.1) for ferroelectric ($T<T_c$), paraelectric ($T>T_c$) and phase transition temperature ($T=T_c$). The two minima in ferroelectric phase correspond to two equilibrium states of the spontaneous

polarization,

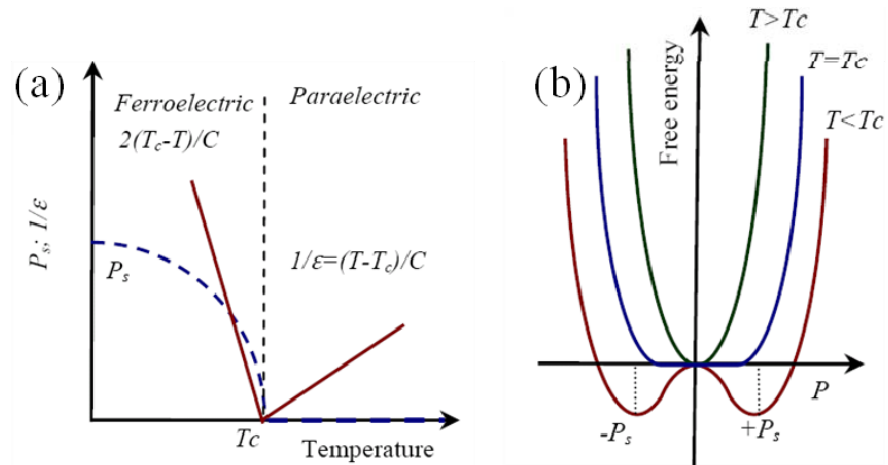


Figure 1.5 2nd order paraelectric to ferroelectric phase transition. (a) Temperature dependences of the polarization and inverse permittivity, and (b) the polarization dependent free energy (Uchino 2000).

1.6 Polarization mechanisms

In ferroelectric phase, the relationship between polarization and electric field is characterized by a hysteresis loop. The presence or absence of spontaneous polarization can be observed by doing either a polarization measurement or a double capacitance – voltage sweep, one voltage sweep for each direction.

From the PE hysteresis loop shown in Figure 1.6(a), several parameters can be identified from the plot, the remnant polarization, P_r , is the polarization value of the material at zero bias, also known as the spontaneous polarization, the saturation polarization, P_s , is the maximum polarization, and the coercive field E_c , is the field necessary to reverse the direction of the net polarization of the material.

The hysteresis with the two equilibrium polarization states is used in nonvolatile

THE HONG KONG POLYTECHNIC UNIVERSITY

memory cells. The corresponding permittivity field dependence is shown in Figure 1.6(c). According to the diagram, the two maxima in permittivity appear at coercive field $\pm E_c$. In principle, this type of butterfly permittivity field dependence may be used in analog tunable microwave varactors provided that the associated losses are small and the required tuning speeds are not high. In this case, the bias field has to be increased from zero or decrease from E_{\max} in order to establish the required permittivity on the given branch of the $\epsilon(E)$ vs E curve. Additionally, in polar phase all ferroelectrics also are piezoelectric and, as such, some of them are used in acoustoelectronic devices.

In paraelectric phase, ($T > T_c$), the spontaneous polarization is zero and the inverse permittivity is a nonlinear function of the applied electric field. At small bias fields the free energy is a parabolic function of the polarization as it appears in Eq. (1.5.5).

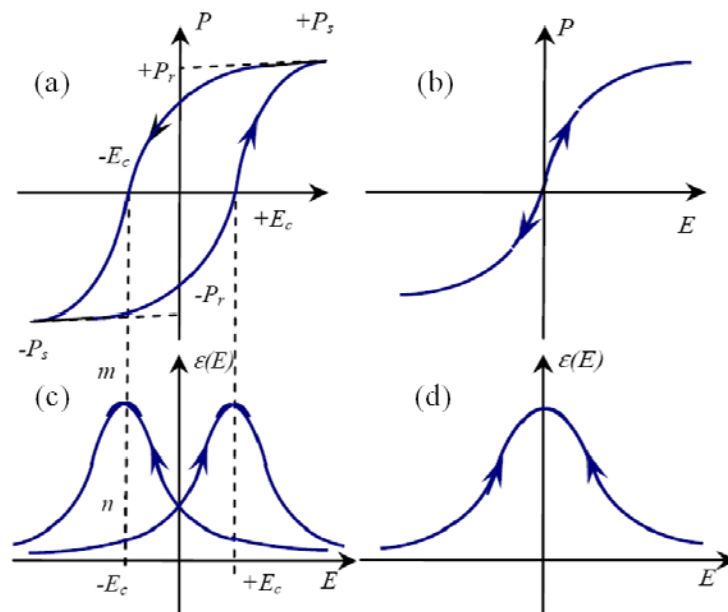


Figure 1.6 Polarization (a and c) and permittivity (c and d) dependences on the applied electric field for ferroelectric (a and c) and paraelectric (b and d) (Uchino 2000).



THE HONG KONG POLYTECHNIC UNIVERSITY

The $P(E)$ dependence in this phase is again nonlinear but without hysteresis loop (Figure 1.6(c)). The $\varepsilon(E)$ performance is also essentially nonlinear (Figure 1.6 (d)) and for small bias field it is characterized with a parabolic dependence, as shown below. In this phase, using the relationship between polarization and applied field, $P = \varepsilon_0 \varepsilon(0)E$, one gets from Eq. (1.5.3). $\varepsilon(0) = \frac{1}{\alpha \varepsilon_0}$. By using Eq. (1.5.5) one arrives at:

$$\varepsilon(E, T) = \frac{\varepsilon(0, T)}{1 + 3\beta \varepsilon_0^3 \varepsilon^3(0, T) E^2} \quad (1.6.1)$$

where the temperature dependence of the permittivity at zero bias field, $\varepsilon(0, T)$ is given by Eqs. (1.5.6) and (1.5.7)

Typically higher permittivity leads to higher tunability. This effect can be clearly observed if we combine Eqs (1.5.3) and (1.6.1).

$$n = \frac{\varepsilon(0)}{\varepsilon(E)} = 1 + 3\beta \varepsilon(0) \varepsilon_0 P_{dc}^2 \approx 1 + 3\beta (\varepsilon(0) \varepsilon_0)^3 E_0^2 \quad (1.6.2)$$

$$n \propto \varepsilon(0)^3 \quad (1.6.3)$$

From Eq.(1.6.3), we can see that the relative tunability has a strong dependence on the permittivity value. However under higher electric field, the dependence slows down. In the limit of very high electric field, where $n \gg 1$, the tunability is directly proportional to the permittivity.

When using dielectric materials the permittivity and the loss are two important parameters to consider when designing a device. However, they are not the only ones, it is also important to consider the resistance of the dielectrics to conduction at different voltages. For a given material, the voltage across the dielectric cannot be infinitely increased. There is an electric field at which the material cannot tolerate,



leading to a significant conduction between the electrodes. This voltage is commonly called the dielectric breakdown. For gaseous and some liquid dielectrics, the breakdown is not necessarily permanent, so if the high voltage is removed, the material can return to insulating behaviour. However for solids, breakdown generally leads to permanent formation of a conduction path, which in most cases renders the material useless.

Dielectric breakdown in solids is an important concern for dielectric research. There are different types of dielectric breakdown mechanism in solids. The intrinsic or electronic breakdown, as the name indicates, is related to the intrinsic property of the material and is caused by the liberation of electrons from interatomic bonds. The most common type of electronic breakdown is due to the electron avalanche breakdown. When a large enough electric field is applied to a material, an electron in the valence band can be accelerated to have enough energy to collide and ionize the host atom of the material. If the energy is large enough, this collision can promote a valence electron to the conduction band, which physically means the breaking of a bond. The initial collision may be followed by further collisions from the primary and secondary electrons, which leads to an electron avalanche, causing a significant flow of current in the material. This breakdown is typically very high, and thus only observed in very perfect materials. Generally, micro-structural defects locally concentrate electric fields which lead to breakdown before this mechanism is globally activated. Other type of electronic breakdowns includes Fowler-Nordheim field emission and tunnelling injection.

Thermal breakdown occurs when elevated temperature accompany conduction



THE HONG KONG POLYTECHNIC UNIVERSITY

and promote localized breakdown and damage. When an electric field is applied, locally elevated temperatures can occur for two reasons: Joule heating and random molecular collisions. If the material cannot efficiently release the heat, then further heating occurs leading to failure in localized spots where the transfer of heat is less efficient, and as these regions grow further, eventually a conductive path is created.

External discharge breakdown is due to the presence of contaminants that have lower dielectric breakdown within the material and thus lead to failure of the material at a lower electric field than normally observed for contaminant free material. Contaminants include: moisture, pollutants, dust, dirt and others. Other dielectric breakdown mechanisms are: electromechanical breakdown and electro-fracture, internal discharge, and insulation aging, these mechanisms are mostly observed in soft materials.

1.7 Structure and properties of BSZT

1.7.1 Bulk materials

Usually, in ABO_3 perovskites, substituting A and/or B sites by other ions can modify electric behaviour of the material. The addition of Sr into the Ba site of barium titanate can shift the ferroelectric to paraelectric phase transition from high temperature to low temperature, resulting in a barium strontium titanate $(Ba_{1-x}Sr_x)TiO_3$ material with high dielectric constant at room temperature. The introduction of the Sr atoms into the barium titanate lattice influences both the crystalline structure and the properties. Moreover, a substitution of Ti by Zr, $Ba(Zr_xTi_{1-x})O_3$ has also been found to be an effective way to decrease the Curie temperature, and exhibits several interesting

THE HONG KONG POLYTECHNIC UNIVERSITY

features in the dielectric behaviour of BaTiO₃ ceramics. Figure 1.7 shows the Curie temperature of BST and BZT with different compositions.

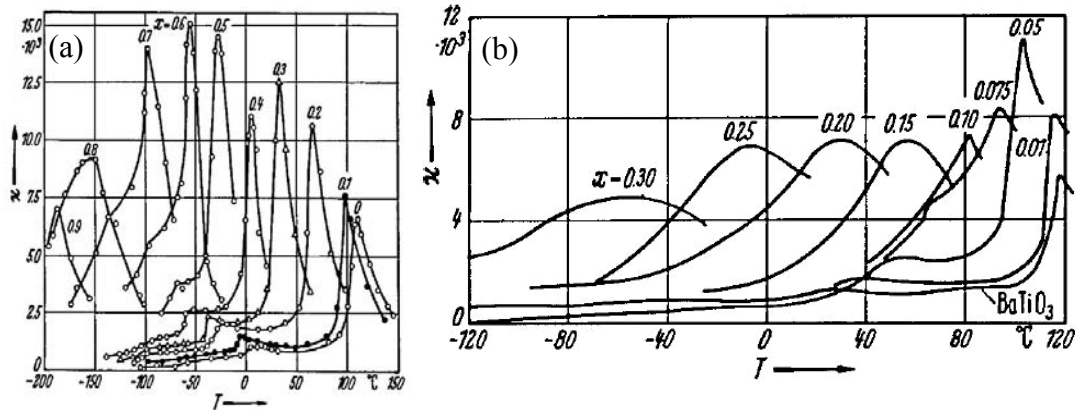


Figure 1.7 Curie temperature of (a) (Ba_{1-x}Sr_x)TiO₃ and (b) Ba(Zr_xTi_{1-x})O₃ with different compositions (Springer-Verlag 2001).

Tetravalent ion such as Zr⁴⁺ is of interest because a different character of dielectric response can be achieved by the substitution of Zr for Ti in the B sites of ABO₃. The Zr⁴⁺ ion is chemically more stable than the Ti⁴⁺ and has a larger ionic size to expand the perovskite lattice. It is reported that Zr doping to barium titanate (BT) resulted in the higher chemical stability and the reduction of the dielectric loss. In order to enhance the electric properties of BST thin film over a large temperature range, it is necessary to broaden the Curie temperature range of BST. It is therefore expected that a solid solution comprising of both BZT and BST would incorporate the features of both Sr and Zr substitution in the BT lattice.

In this project, we attempt to combine the advantages of BST and BZT and to make a new candidate material (Ba,Sr)(Ti,Zr)O₃ with higher dielectric constant and



lower leakage current density.

1.7.2 BSZT thin films

Ferroelectric thin films have attracted a lot of attention in recent years due to their unique properties such as spontaneous polarization, high dielectric constant, low dielectric loss, low leakage currents and high breakdown voltage which make them suitable for various applications.

BST and BZT are materials that have excellent microwave performance due to their large relative permittivity and high dielectric tunability in the microwave regime at room temperature and have been used in frequency or phase agile shifters for applications in phased array antennas. BSZT films are expected to exhibit superior dielectric properties compared to similar materials, such as BST and BZT.

BSZT is obtained by substituting ions at the B site and A site of the BaTiO_3 with Zr and Sr in the perovskite ABO_3 structure. It has been reported that an increase in the Zr content induces a reduction in the average grain size, a decrease in the dielectric constant, and maintains a low and stable leakage current.

Many researchers have studied the growth of epitaxial ferroelectric thin films on lattice mismatched substrates for tunable microwave devices. When the epi-layer of ferroelectric was grown on substrates, it is strained due to the lattice mismatch. Strain is a very significant factor as ionic positions and vibrations in a ferroelectric are modified by the strain, and these changes are coupled to the polarization mechanism in



THE HONG KONG POLYTECHNIC UNIVERSITY

the ferroelectrics. The properties of the films are strongly dependent on the processing techniques. Some properties of the reported BSZT thin films are summarized in Table 1.1.

For optimal performance of the tunable devices, it is important to grow a material with high dielectric tunability, low dielectric loss, low hysteresis, and low temperature dependence of the dielectric permittivity in the operation frequency and temperature range of the device.



Table 1.1 Literature survey on BSZT thin films.

Substrate	Deposition method	Structure	ϵ_r	$\tan\delta$	K(%)	Composition	Leakage current(A/cm ²)	Ref.
Pt(111)/Ti/SiO ₂ /Si(001)	MOCVD	polycrystalline	977	0.04	-----	(Ba _{0.65} Sr _{0.65})(Ti _{0.65} Zr _{0.35})O ₃	10 ⁻⁷ -10 ⁻⁸	(Jae-Dong Byun et al. 2000)
Pt(111)/Ti/SiO ₂ /Si(001)	PLD	(001) orientated	321	0.014	53% (1MHz)	(Ba _{0.75} Sr _{0.25})(Zr _{0.25} Ti _{0.75})O ₃	-----	(Tang et al. 2005)
Pt/TiO ₂ /SiO ₂ /Si	PLD	polycrystalline	160-340	0.04	50% (330kV/cm)	(Ba _{0.8} Sr _{0.2})(Zr _x Ti _{1-x})O ₃ x=0-0.36	10 ⁻³ -10 ⁻⁷	(Cheng et al. 2005)
MgO(001)	PLD	(001) orientated	1000	0.002	25.3% (200V)	(Ba _{0.6} Sr _{0.4})(Zr _{0.1} Ti _{0.9})O ₃	-----	(Ha et al. 2006)
Pt/TiO ₂ /SiO ₂ /Si	PLD	(110) orientated	200-350	-----	~53%	(Ba _{0.8} Sr _{0.2})(Zr _x Ti _{1-x})O ₃ x=0-0.36	-----	(Wang et al. 2004)
Pt/SiO ₂ /Si	RF sputtering	polycrystalline	220-260	-----	-----	(Ba _{0.7} Sr _{0.3})(Zr _{0.1} Ti _{0.9})O ₃	10 ⁻⁸ -10 ⁻⁹	(Chen et al. 2004)
Pt/Ti/SiO ₂ /Si	RF sputtering	polycrystalline	380-525	0.03	-----	(Ba _{0.65} Sr _{0.35})(Zr _{0.35} Ti _{0.65})O ₃	10 ⁻⁷ -10 ⁻⁹	(Park et al. 2001)



Substrate	Deposition method	Structure	ϵ_r	$\tan\delta$	K(%)	Composition	Leakage current(A/cm ²)	Ref.
Pt/SiO ₂ /Si	RF sputtering	polycrystalline	180	-----	-----	(Ba _{0.7} Sr _{0.3}) (Zr _{0.1} Ti _{0.9})O ₃	10 ⁻⁸	(Chen et al. 2004)
Copper foils	Sol gel	polycrystalline	200-307	<0.1	-----	(Ba _{0.7} Sr _{0.3}) (Zr _x Ti _{1-x})O ₃ x = 0.1, 0.2	10 ⁻⁵ -10 ⁻⁴	(Fan et al. 2010)
Pt(111)/Ti/SiO ₂ / Si(001)	Sol gel	polycrystalline	135-365	<0.02	34.8%-54% (500kV/cm)	(Ba _{0.90} Sr _{0.10}) (Zr _x Ti _{1-x})O ₃ x=0-0.40	-----	(GAO Lina et al.)
Platinum substrate	Sol gel	polycrystalline	125-400	<0.02	-----	(Ba _{0.8} Sr _{0.2}) (Zr _x Ti _{1-x})O ₃ x=0-0.5	-----	(Dixit et al. 2007)
Pt/TiO ₂ /SiO ₂ /Si	Sol gel	polycrystalline	190-304	-----	-----	(Ba _{0.9} Sr _{0.1}) (Zr _x Ti _{1-x})O ₃ x = 0.1 0.2	-----	(Kumar et al. 2008)



1.8 Substrates for microwave devices

Important parameters that influence the design of a MW device are the frequency of operation, substrate, thin film, top electrode, and gain and voltage requirements. In this section, the requirements of substrates used in microwave circuit are discussed.

During the mid and late 60s high purity (99.5%) alumina substrates were introduced in MW circuits. It had two attractive properties: moderate dielectric constant ($\epsilon \sim 10$) and smooth surface finish. Alumina substrates with higher purity (99.6%) and smaller particle size were introduced in the MW device market in the 1970s. Today the most widely used alumina substrates have a purity of 99.7% and 99.8%.

Today the microwave circuit designer has many materials to choose from market depending upon the end application. Here it is important to distinguish between two terms that are used for the same purpose in the MW circuit world. These are ‘laminates’ and ‘substrates’. Usually laminates refer to ‘soft’ material such as Teflon (PTFE) which may contain fiberglass or ceramics reinforcement for mechanical integrity. On the other hand, ceramics materials are known as ‘hard’ substrates and are usually Al_2O_3 (polycrystalline alumina or single crystalline sapphire), MgO (magnesium oxide) and LaAlO_3 (lanthanum aluminate)

Important parameters for the substrate used in MW devices are the dielectric constant, loss tangent, CTE (coefficient of thermal expansion), size, cost and availability.



THE HONG KONG POLYTECHNIC UNIVERSITY

Dielectric constant is the ratio of the amount of electrical energy stored in a material by an applied voltage, relative to that stored in vacuum. The wavelength or the velocity of the microwave signal changes when it travels through the substrate. This is given by the following formula:

$$\lambda = c/(f\sqrt{\epsilon}) \quad (1.8.1)$$

where λ is the wavelength, c the velocity of light in vacuum, f the frequency of operation, and ϵ is the permittivity of the material.

Another important factor is the dissipation loss. Dissipation loss $\tan\delta$ is the ratio of the energy dissipated to the energy stored in the material. From the device metrics point of view the dissipation loss in the substrate should be as low as possible to minimize the total loss in the MW device.

CTE (coefficient of thermal expansion) of a material is the parameter that defines how much the material changes its dimensions when it is heated or cooled. It is expressed in parts per million per degree change in temperature. The CTE of the MW substrate should be as close to the CTE of the film deposited on the substrate as possible since a large difference will lead to compressive or tensile strain at the film substrate interface and will lead to film cracking. Hence from the design point of view, CTE of the MW substrate is an important factor while fabricating a MW device.

Another important factor that should be considered from the substrate point of view is the flatness or the surface roughness of the substrate. Flat surfaces are required to ensure proper operation of vacuum fixture during exposure and good contact with the mask during the UV light exposure in photolithography. The surface finish on the



THE HONG KONG POLYTECHNIC UNIVERSITY

substrate decides the limits of the photolithographic process in the fabrication of the MW devices.

Table 1.2 List of different substrates (Crystec).

Substrate	ϵ_r (@1MHz)	$\tan\delta$ (@10Hz)	CTE(/K)	Lattice constant(Å)
MgO	9.8	9×10^{-3}	8.0×10^{-6}	4.212(cubic)
LaAlO ₃	23.5	6×10^{-5}	10×10^{-6}	3.790(cubic)
(LaSr)(AlTa)O ₃	22.7	2×10^{-4}	8.2×10^{-6}	3.868(cubic)
SrTiO ₃	300	2×10^{-2}	9×10^{-6}	3.905(cubic)
DyScO ₃	21	-----	8.4×10^{-6}	a=5.44;b=5.71;c=7.89
NdGaO ₃	20	3×10^{-3}	9×10^{-6}	a=5.43;b=5.50;c=7.71

The quality of thin films is strongly controlled by the quality of the substrate on which they are deposited. For the epitaxial growth of films with perovskite structure, single crystal substrates with the following specifications are required. The lattice constant and thermal expansion coefficient of the substrates should closely match those of the films. Also the substrate should not have phase transitions, which create microtwins. In addition, for many electrical applications, low dielectric constants and dielectric losses are required. And finally, the cost should be relatively low. Many single crystal such as SrTiO₃(STO), LaAlO₃ (LAO), and MgO are used for growth of perovskite films. However, these single crystals satisfy only some of the required substrate specifications mentioned above. Table 1.2 lists some substrates and useful data for references.

Therefore, approaches using new perovskite substrates have been used to meet these requirements. In the search of new substrate for superconductor films,



THE HONG KONG POLYTECHNIC UNIVERSITY

(La,Sr)(Al,Ta)O₃ (LSAT), a 30/70mol% solid solution between LaAlO₃ (LAO) and Sr₂AlTaO₆ (SAT), was fabricated. The new material LSAT eliminates the difficulties of twinning, strain, and anisotropic properties found in pure LAO. In addition, LSAT has low dielectric loss and medium dielectric constant, which makes it suitable for microwave applications. Therefore, LSAT has received increased attention since its introduction and has been used as the substrate of choice in various thin film deposition.

1.9 Frequency agile technologies

For system miniaturization and in terms of adaptability, frequency selective application is one of the areas where agile solutions provide greatest benefits. In frequency agile device, the resonant frequency on the basic element circuit depends on the inductance and capacitance as shown in the following equation:

$$f_o = \frac{1}{2\pi\sqrt{LC}} \quad (1.9.1)$$

where L is the inductance and C is the capacitance. To achieve agile devices, tunable capacitors have been extensively used in RF circuits.(Laskar et al. 2006) There are different technologies that can produce tunable capacitors. Table 1.3 shows the summary of main technologies available at the present moment. (Gevorgian 2009). Hence, by changing either the L or C value, the resonant frequency of the circuit can be changed. A summary of the main technologies available at the present moment is discussed below. (Gevorgian 2009)

MEMS: MEMs are miniature versions of mechanical switches fabricated at micron size ranges. The tuning speed of the device is high and offer very low loss. However,



THE HONG KONG POLYTECHNIC UNIVERSITY

the fabrication and the packaging are rather too complex and the reliability of the device remains an issue.

Magnetic: Based on the external magnetic field, the capacitance of the magnetic based devices can be tuned. Device based on ferromagnetic materials typically exhibit very low loss, high tuning ranges and high selectivity. However, the tuning speed of the magnetic based devices is slow compared with other technologies.

Semiconductor: In a semiconductor based varactor, tunability is achieved by the change in the depletion width when a reverse bias is applied to a PN junction. For frequencies up to 1GHz, the semiconductor based varactor represents the state of the art technology used for tuning microwave devices. However, for frequencies above 10GHz, the loss tends to degrade drastically. For a large array of semiconductor based device, power consumption and heat dissipation became a liability especially in a dense board.

Liquid crystal and optical: These technologies have been tested for potential microwave application. The research of these two technologies for microwave devices is still in the infant stage.

Ferroelectrics have rather high permittivity (for thin films >100), allowing a substantial reduction in the sizes of microwave components. The main advantages of ferroelectric films for microwave applications include frequency independent tunability (up to 50% or more), high tuning speed ($<1.0\text{ns}$), extremely small leakage currents and DC control power, high breakdown field, and radiation hardness. In

microwave devices they are used in the form of single crystals (bulk thin film) and ceramics (bulk, film).

Ferroelectric: the principle of the ferroelectric based varactor is based on the electric field dependent permittivity. Based on the ferroelectric based varactor, the device typically offer high speed, very small power consumption and lower loss compared to the semiconductor based varactors at frequencies above 10GHz. Usually, the ferroelectric based varactor offers high dielectric permittivity, the size of the tunable elements based on ferroelectrics may be smaller in comparison to the other technologies.

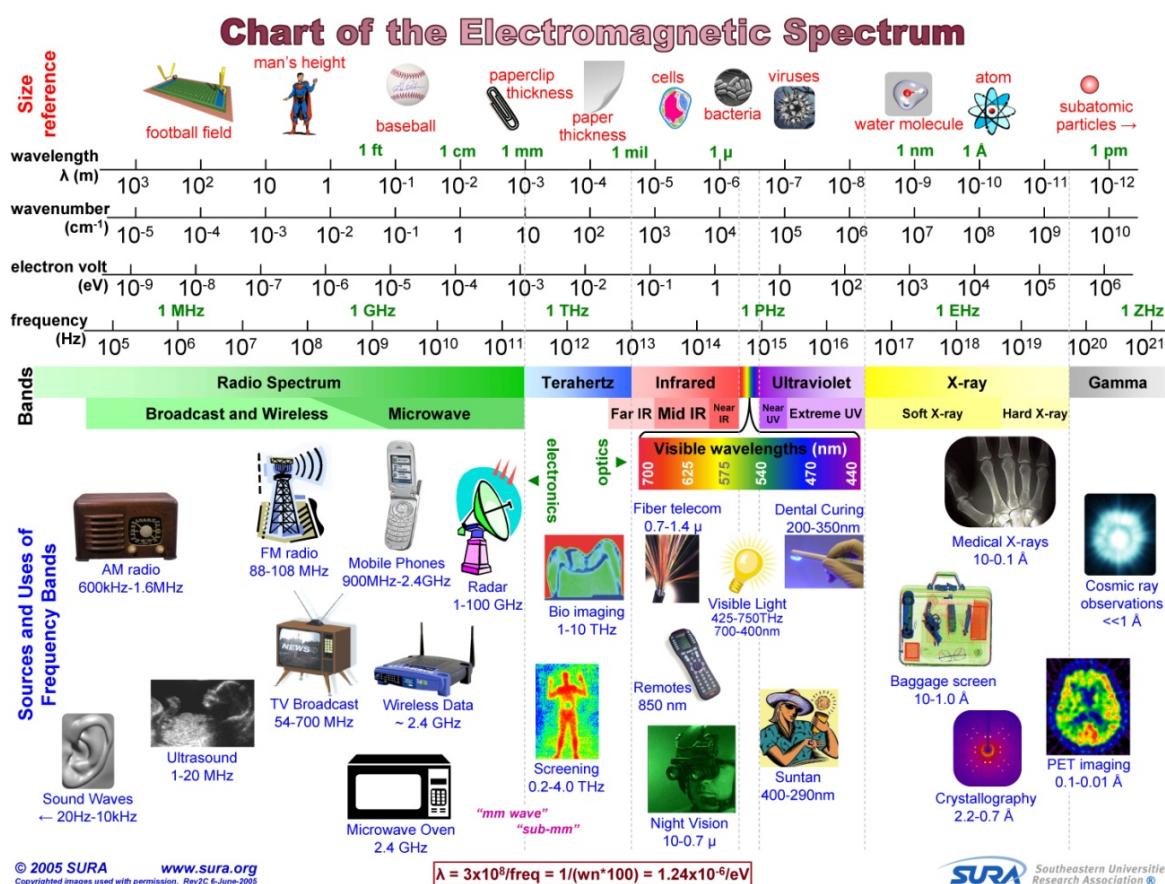


Figure 1.8 The electromagnetic spectrum for different frequency bands and the corresponding applications (SURA).

From the large number of ferroelectric materials known today, only a limited number of them are considered for microwave applications. Both polar (ferroelectric) and paraelectric phases may be useful in tunable microwave devices, provided they have low losses and reasonable tunability. However, the paraelectric phase is preferred since in this phase there is no hysteresis associated with the domains.

The frequency dependence of the permittivity and the loss is due to the different polarization mechanisms active within the material. The permittivity is given by the sum of all the active polarizations at a given frequency, while the loss generally consists of two contributions; one due to conduction and the other due to relaxation effects. The frequency dependence of the real and imaginary parts of the dielectric constant in the presence of the different polarization mechanisms is shown in the following figure (Figure 1.9).

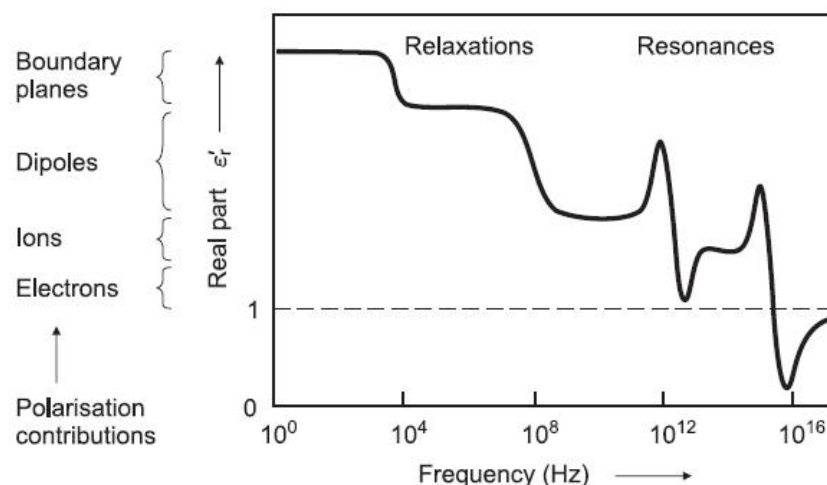


Figure 1.9 Real and complex permittivities contribution from different polarization mechanism as a function of frequency (PeterP).



Table 1.3 Comparison between different technology for agile devices (Gevorgian 2009).

Categories	Technology	Power consumption	Bias	Speed	Q factor at 10GHz
Semiconductor	Schottky (GaAs)	<1mW	<5V	<1ns	200
	Abrupt p-n junction (Si)	<5mW	<30V	<10ns	30
	P-I-N diode	<0.1mW	<10V	<1μs	-----
Magnetic	YIG (variable permeability, ferromagnetic resonance)	High	Current (coil)	<5ms	>3000
	Remnant magnetization	Low	Current (coil)	<5ms	-----
	Magneto-static (spin) wave	Low	-----	<5ms	Low
Ferroelectric	Thin film	Negligible	<30V	<1ns	>100
	Thick film	Negligible	<1000V	<10ns	<100
	Bulk	Negligible	<15kV	<1μs	>500
Liquid crystal	Negligible	-----	<40V	<10ms	<20
Optical	Photoconductivity	<10mW	Current (LD,LED)	10fs-10ms	<10
	Fibre-optical	<10mW	Current (LD,LED)	10fs-10ms	-----
Mechanical	Bulk	High	Current(motor/coil)	>1ms	>1000
	MEM varactor	Negligible	<50V	>10μs	>200
	Piezotransducer	Negligible	>100V	>100μs	>500



As shown in Figure 1.9, the total polarization contribution to the real term of the permittivity is additive. The electronic polarization, which is due to the shifting of the electron cloud with respect to the positive nuclei/core by an applied electric field, is present at all frequencies, for all materials, up to 10^{16} Hz (due to their extremely low mass), beyond this range the material behaves as a vacuum, $\epsilon' \sim 1$, $\chi \sim 0$. The contribution due to the electronic polarization is rather small compared to the other mechanisms due to the small number of polarisable charges present around the atoms and the limited displacement allowed due to the large restoring force. Typical permittivity values for materials with only electronic polarization mechanism are generally around 1 to 5. However for covalent material such as silicon $\epsilon' \sim 11.9$, where the most prevalent contribution to the permittivity is from the electronic polarization, the permittivity value is exceptionally high. This is attributed to the delocalization of the valence electrons, which are not necessarily fixed in their positions. They can tunnel from bond to bond, and thus when an electric field is applied, the negative charges shift with respect to the positive ionic cores rather than a single atom.

Ionic polarization is also present in all materials that are not perfectly covalent. Compared to the electronic mechanism, the ionic polarization responds at a lower frequency, about the infrared frequency, due to the higher mass of the ions. The polarization is the result of the change in bond length due to the shifting of the positive and negative ions under an applied electric field, and for this case the restoring force depends on the ionic bond. Generally, this mechanism contributes to higher permittivity compared to the electronic polarization. A typical ionic material like common salt, NaCl, has a permittivity value close to 6.



For both the ionic and electronic mechanisms, the dipoles are created after an electric field is applied. In the case of orientational or dipolar mechanism, the polarization is the result of the re-alignment of the permanent dipole moments within the material. Some materials, such as water, possess permanent local dipole moments. In liquid such as water, as the dipoles are randomly oriented due to thermal agitation, these results in a net polarization to zero. However, when an electric field is applied, the dipoles are forced to align parallel to the electric field, and thus resulting in a net polarization. This polarization mechanism responds at even lower frequency than the two previously mentioned mechanisms, around 10^6 Hz, partly due of the slow movement of the dipoles within the material. Yet the contribution is larger compared to the other two mechanisms, for example, water has a permittivity of about 80.

The final polarization mechanism is the interfacial or space charge polarization. This mechanism is due to accumulation of charges around a material singularity. e.g. grain boundaries, defect etc. When an electric field is applied to such a crystal, there is a displacement of charges, which move until they encounter an insulating boundary. The accumulation of charges results in a net polarization. Take for example at grain boundary, when an electric field is applied, grain boundaries generally trap charges moving under the applied field which leads to a dipole at the interface of the grain, thus the name interfacial polarization. Generally dipoles involved in this mechanisms are very large in term of mass and also their motion are dramatically slower, so the relaxation time is very long, leading to low frequency response, around 1Hz to 1kHz.

It is generally assumed that for applications in electrically tunable microwave devices, ferroelectrics should be in a paraelectric phase. Ferroelectrics in polar phase



THE HONG KONG POLYTECHNIC UNIVERSITY

have not been considered for applications in tunable microwave devices. The reason is that most of the ferroelectrics in polar phase are also piezoelectric and piezoelectric transformation cause large losses at relatively low microwave frequencies (typically less than 10GHz). Additional losses in the polar phase and at low frequencies are associated with domain wall movements. Hysteresis, which appears in permittivity-DC field dependence, is another reason hindering the application of a ferroelectric in a polar phase.

The dielectric loss is a critical parameter to consider when optimizing the properties of the material. Low loss is almost always desired for electronic applications, especially for high frequency devices, where dielectric loss would lead to signal loss, which decreases the signal to noise ratio.

The dielectric loss mechanism can be broadly categorized into two major contributions: extrinsic and intrinsic. In the case of ferroelectric phase, extrinsic losses arise from several contributions including domain processes, material defects and local polar regions. Large contribution to the ferroelectric loss comes from the motion of the domain walls (Plessner 1956; B.Lewis 1959). Domain walls can be pinned by interactions with point defects and dislocations. The origin of the loss is due to the internal friction from the interaction of domain walls with the point defects.(V.S Postnikov 1968; V.S Postnikov 1970) Additional information about the contribution of domain motion to the ferroelectric losses can be obtained by doing measurement at high frequencies. Decrease in domain wall motion resonance explains the reduction in permittivity and increase in the loss tangent at high frequencies. (C.Kittel 1951; Sannikov 1962)



In case of the paraelectric phase where ferroelectric domains are absent, the loss tangent is substantially lower, which makes it a good candidate for microwave devices. However, the absence of the domain walls does not imply a lack of extrinsic loss in the paraelectric phases. Charged point defects, dielectric relaxation and quasi-Debye contribution induced by random defects are known to contribute to the extrinsic loss. (Sannikov 1962) When an AC field is applied, charged point defects tend to move resulting in the generation of acoustic waves at the frequency of the applied field. The loss contribution from the dielectric relaxation was deduced from the linear frequency dependence of the loss tangent at the microwave and higher frequencies, which is attributed to the proposed universal relaxation law (A.K Tagantsev et al. 1965). The physical nature of this contribution is attributed to a variation in charge transport across barriers such as grain boundaries (Auciello et al. 1995), or to oxygen vacancies (Fukuda et al. 1996) near the interface of the depletion layer.

At microwave frequencies the intrinsic and extrinsic contributions are comparable, so the dominating factor would be determined by the quality of the material, hence for a good ceramic, the loss tangent will be mostly dominated by the extrinsic contribution. However in the presence of an electric bias, most of the defects and impurities in the crystal are ‘frozen’, thus the loss tangent is mostly dominated by the intrinsic contribution. Tagantsev summarized the main loss mechanisms that contribute to the intrinsic loss in paraelectric materials. The source of the intrinsic loss can be attributed exclusively to the interaction of the AC field with phonons in the material.

Typically high permittivity values in ferroelectric materials lead to higher losses. The acceptable amount of loss should be designed according to the particular application. As pointed out earlier, for microwave devices, the common agreement is



THE HONG KONG POLYTECHNIC UNIVERSITY

that lower loss materials are preferred, and most of the reports found in the literature concur that the use of the paraelectric phase is paramount for obtaining high quality devices.

For barium titanate, BaTiO_3 , which is typically in the ferroelectric phase at room temperature, the paraelectric phase, can be achieved by cation substitution of the A-site with strontium atoms. Strontium titanate (SrTiO_3) is an incipient ferroelectric and forms complete solid solutions with barium titanate. Increasing the mol% concentration of strontium in the solution leads to a drop in the Curie temperature of BaTiO_3 with a linear dependence $\sim 3.5^\circ\text{C}$ per mol % of strontium atoms. The highest permittivity, and hence tunability, is observed when approaching the Curie point. So, for a paraelectric phase the ideal BST composition would be the one that exhibit a Curie point just below the room temperature. However, a lower loss is observed when the material is far away from the Curie point. So this is the point where a decision must be made to decide the maximum loss acceptable for the application in mind, and based on that decision, then, a composition is chosen to obtain the highest tunability with an acceptable amount of loss.

1.10 Scope of the project

The main objective of this thesis is to fabricate and characterize barium strontium zirconate titanate $(\text{Ba}_{1-x}\text{Sr}_x)(\text{Zr}_{0.1}\text{Ti}_{0.9})\text{O}_3$ ceramics and thin films. The dielectric, ferroelectric and the structural properties of the BSZT ceramics and thin films were studied. Based on the results, microwave devices of BSZT thin film based microstrip ring resonators and phase shifters were fabricated and characterized.



THE HONG KONG POLYTECHNIC UNIVERSITY

This thesis is divided into six Chapters. Following the introduction given in this Chapter, the fabrication and characterization of $(\text{Ba}_{1-x}\text{Sr}_x)(\text{Zr}_{0.1}\text{Ti}_{0.9})\text{O}_3$ ceramics with ($x = 0, 0.05, 0.15, 0.25, 0.35, 0.45$) by a solid state reaction method are described in Chapter 2.

In Chapter 3, BSZT thin film with various compositions ($x = 0, 0.05, 0.15, 0.25, 0.35, 0.45$) have been deposited by pulsed laser deposition. With the help of X-ray diffraction and the atomic force microscopy measurements, structural properties of the BSZT thin films have been found. BSZT thin films have been also deposited on three different substrates and their structure were studied.

Chapter 4 describes the in-plane dielectric, ferroelectric properties of the BSZT thin films, the properties are measured by the coplanar interdigital capacitors patterned by photolithography. The tunable dielectric properties of the BSZT thin films on different substrates are also presented.

Chapter 5 demonstrates the fabrication and characterization of the BSZT thin film based microwave devices. The performance of the microstrip ring resonator and phase shifters are measured.

Conclusions and suggestions for future work are given in Chapter 6.



CHAPTER 2

FABRICATION AND CHARACTERIZATION OF BARIUM STRONTIUM ZIRCONATE TITANATE CERAMICS

2.1 Introduction

(Ba, Sr) TiO₃ (BST) and Ba (Zr, Ti)O₃ (BZT) materials are perovskite based ferroelectrics which have attracted considerable interest in tunable microwave device applications. For ABO₃ perovskites, substituting A and/or B sites by other ions can modify the dielectric behaviour of the material.

In BST solid solution, the addition of Sr ions into the Ba site of barium titanate (BT) can shift the Curie transition of BT to a lower temperature, the Curie point of BST drops to 0°C with ~34% Sr content, which corresponds to a decrease of 3.8°C per molar % of Sr. (Jaffe et al. 1971; Kumar et al. 2008) BZT has found to be a possible alternative to BST because Zr⁴⁺ (0.087nm) is chemically more stable than Ti⁴⁺ (0.068nm) (Ha et al. 2007). The addition of Zr ions into BaTiO₃ has also been found to be an effective way to decrease the Curie transition temperature. When the Zr content is higher than 20mol%, BZT becomes a relaxor ferroelectrics. For BZT ceramics, the structural, dielectric and ferroelectric properties have been reported in literatures and the characteristics of BZT ceramics depend strongly on the Zr content. (Sen and Choudhary 2004; Chen et al. 2008; Xiong et al. 2008). (Ba,Sr)(Zr,Ti)O₃ (BSZT) is a solid solution of BST and BZT. It is expected that the addition of Zr and Sr into BaTiO₃ will result in a modified BSZT ceramics (Jaffe et al. 1971; Bera and Rout 2007;



THE HONG KONG POLYTECHNIC UNIVERSITY

Xu et al. 2007; Kumar et al. 2008). There are not much work reported on the Sr substituted $\text{Ba}(\text{Zr}_{0.1}, \text{Ti}_{0.9})\text{O}_3$ electroceramics, because of its high dielectric constant and superior ferroelectric properties among the Ba (Zr,Ti) O_3 based compounds (Yu et al. 2002). In this Chapter, investigations of the structural, dielectric, piezoelectric and ferroelectric properties of the $(\text{Ba}_{1-x}, \text{Sr}_x)(\text{Zr}_{0.1}, \text{Ti}_{0.9})\text{O}_3$ ($x = 0, 0.05, 0.15, 0.25, 0.35, 0.45$) ceramics are reported.

2.2 Fabrication of barium strontium zirconate titanate ceramics

Four steps are used to fabricate BSZT ceramics, they include powder preparation, dry pressing, binder burnout and sintering.

2.2.1 Preparation of BSZT ceramics

Raw materials used in powder preparation are reagent grade carbonate powders, including BaCO_3 , SrCO_3 , ZrO_2 and TiO_2 . The powders were weighted and mixed in ethanol using zirconia balls for 12h. Afterwards, the mixture was put in an oven to vaporize the ethanol.

The dried powders were then calcined at 1250°C for 3h. Solid state reaction will happen to form a partially crystallize specimen. The samples were then cooled naturally to room temperature. After calcinations, the powders were ball milled again for 12h in ethanol and dried, to reduce the size of the powders. The powders must be calcined in an oxidizing ambient, otherwise, the amount of oxygen vacancies inside the sample will affect the measurement results. The calcined powders were mixed with 5



THE HONG KONG POLYTECHNIC UNIVERSITY

wt% polyvinyl alcohol (PVA) as binder for granulation.

The powder was put into a stainless steel pressing mould to form disks of 15mm diameter and 1mm thickness under a pressure of 30MPa. It is important to make sure all the equipment is clean enough to avoid any contamination by impurities.

Heat treatment is an essential and important procedure and it is usually carried out in a computer controlled furnace. The green ceramic discs were then put on an alumina plate with BSZT powders placed around the specimens.

The PVA contained in the pressed discs were burned off at 650°C for 3h in a (Linberg/blue) furnace. The organic burnout process was carried out with a low heating rate of 3 °C /min.

After the burnout process, the samples were covered by an alumina crucible. The samples were sintered at 1450°C for 4h in air using a high temperature furnace (Carbolite RHF1400). Sintering is used to densify the ceramics to change the size of the pores between the particles.

Polishing is an essential step for ceramics fabrication since ceramics have shrinkage after the sintering process, and polishing can refine the surface roughness and ensures the two flat surfaces are parallel to each other. Wet abrasive papers were used to polish the ceramics disc until the thickness become uniform. After polishing, a thin layer of silver paste was applied and cured at 600°C for 15 min on both sides of the ceramics as electrodes for subsequent measurements.



2.2.2 Poling procedures

The fabricated ceramic discs do not exhibit any piezoelectric properties without poling. The materials are isotropic and all the domains are randomly orientated. With the application of a DC electric field, the dipoles inside the ceramics are aligned during the poling process. The poling field, temperature and time must be carefully chosen, otherwise, it may damage the sample. After the poling process, the electric field is removed and a remnant polarization appears to make the sample piezoelectric. From the hysteresis loop, the poling field can be estimated. The sample was mounted on a holder and placed in a silicone oil bath during the poling process.

After poling, a lot of surface charges were generated on the surfaces which induced stress on the samples. After a period of time, the piezoelectricity of the sample may be weakened by stress relaxation. To eliminate the surface charge, short circuit was required. The poled sample was wrapped in an aluminium foil and placed at room temperature for 24h.

2.3 Characterization of BSZT ceramics

2.3.1 Density measurement

The density of the ceramics can be determined using the Archimedes principle. The density of the ceramics is an indicator of the quality of the ceramics. It reflects the amount of defects, such as pores. If the density of the ceramics is low compared with the theoretical value, the properties will be degraded. According to the Archimedes principle, dry mass of the sample in air (m_{dry}) and the mass of the sample suspended in



THE HONG KONG POLYTECHNIC UNIVERSITY

water (m_{wet}) are measured using an electronic balance. With those two parameters, density of the sample can be calculated by the following equation:

$$\rho = \frac{m_{dry}}{m_{dry} - m_{wet}} \cdot \rho_{water} \quad (2.1)$$

where ρ is the density of the sample and ρ_{water} is the density of water which is assumed to be 1000kg/m^3 .

By the Archimedes principle, the measured density of BSZT ceramics is shown in Figure 2.1. The density of the sample is around $5500\text{-}5900\text{ kg/m}^3$, the density decreases with increase in Sr content.

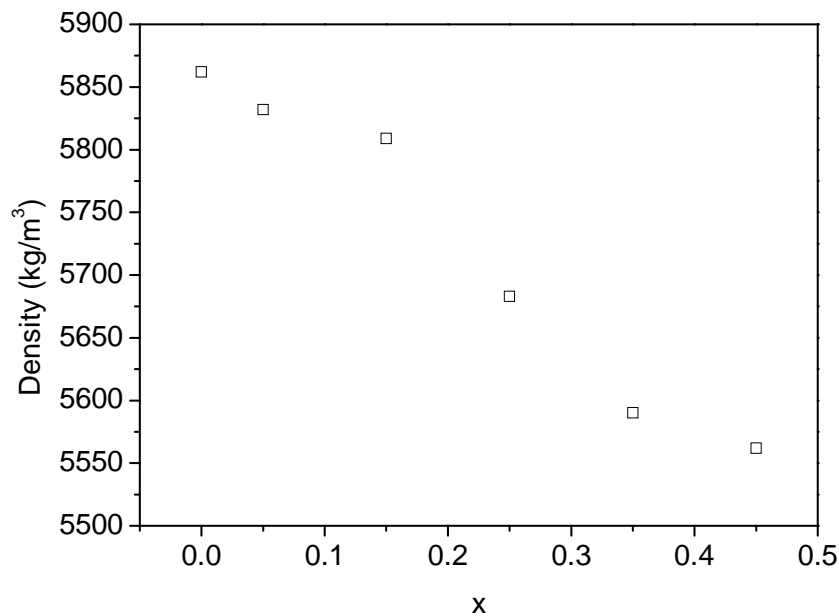


Figure 2.1 Density measurement of the $(\text{Ba}_{1-x}\text{Sr}_x)(\text{Zr}_{0.1}\text{Ti}_{0.9})\text{O}_3$ ($x = 0, 0.05, 0.15, 0.25, 0.35, 0.45$) ceramics.

2.3.2 X-ray diffraction and microstructural analysis

X-ray diffraction (XRD) is a non-destructive technique for analyzing a wide range of materials. XRD has now become an indispensable method for materials characterization and quality control. Areas of applications include qualitative and quantitative phase analysis, crystallography, structure, relaxation determination, texture and residual stress analysis.

If an incident X-ray beam encounters a crystal lattice, scattering occurs. Diffractions occur in a certain direction when the scattered rays from specific planes are in phase. Under this condition the reflections combine to form new enhanced wave fronts (constructive interference). The angle θ at which diffraction occurs can be described by the Bragg's law. (see Figure 2.2)

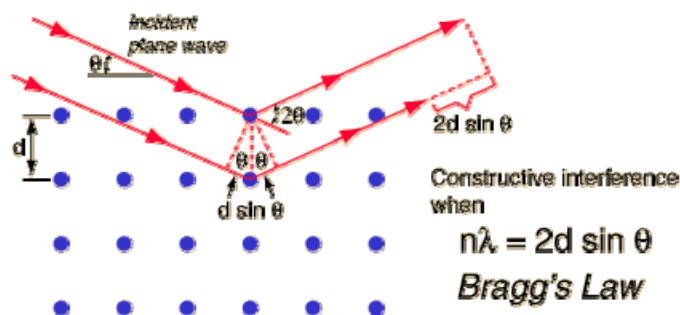


Figure 2.2 Schematic diagram of X-ray diffraction in crystal.

By varying the incidence angle, the Bragg conditions are satisfied by different d spacing in the polycrystals. Plotting the angular positions and intensities of the resultant diffracted peaks of radiation produces a pattern, which is the characteristic for the sample. For every material, it has its own diffractogram.



From the peaks obtained by the detector, computer can be used to find/match the unknown crystalline phase. A library called Powder Diffraction Files (PDF) can be used to find out the matched substance.

The X-ray analysis was conducted with a Philips analytical X-ray diffractometer. The sample was scanned from 10° to 90° in a step size of 0.05° with the X-ray wavelength $K_\alpha=1.54060\text{\AA}$.

Good piezoelectric properties of the BSZT materials arise from the perovskite structure. It is important to make sure that the sintered ceramic samples possess a single perovskite phase. The X-ray diffraction (XRD) patterns of the BSZT ceramics with various (Ba/Sr) ratios are shown in Figure 2.3(a). It is seen that the ceramic samples have perovskite crystal structure and no other phases are observed in the spectra. Without the addition of Sr, the (110) peaks is detected at $31.42^\circ(2\theta)$. With the increase in Sr content, the (110) peak shifts monotonically to a higher 2θ angle, to $31.92^\circ(2\theta)$. Figure 2.3(b) indicates that there is a reduction in lattice parameter with the increase in Sr content. As the ionic radius of Ba^{2+} (1.61\AA) is larger than that of Sr^{2+} (1.44\AA), more Sr^{2+} ions substituted for the Ba^{2+} ions as the Sr content increases, resulting in the decrease in lattice parameter. From Bragg's law, the a- and c- axis lattice constants of BSZT ceramics have been calculated and listed in Table 2.1. With $x = 0.35, 0.45$, the a- and c- axis lattice constant are very close to each other, i.e $c/a \approx 1$, this implies that the crystal structure is very close to cubic, different from the tetragonal structure when $x < 0.35$, indicating a phase transition from tetragonal phase to cubic phase. The volume (a^2c) of the unit cell decreases with the increase in Sr content.

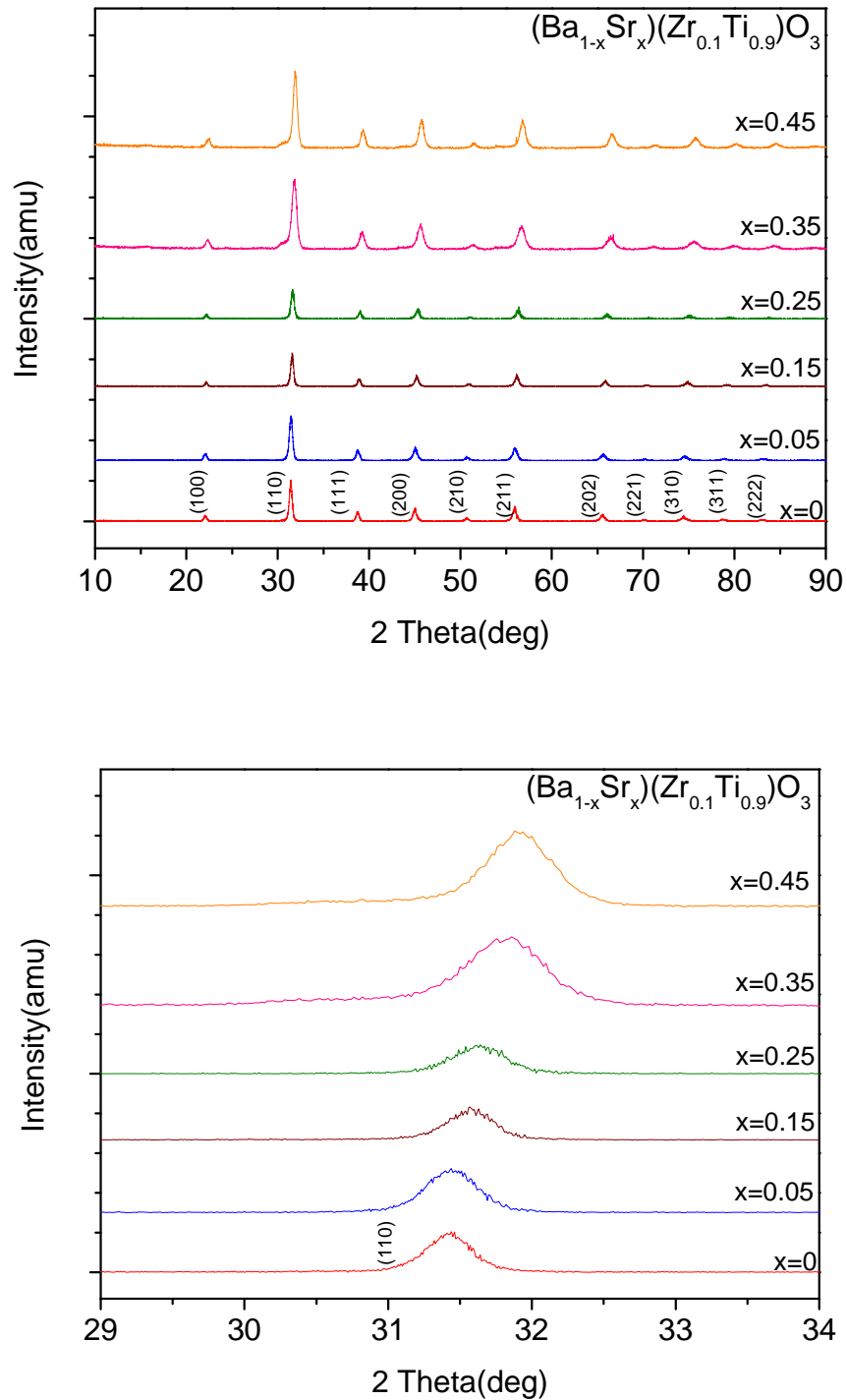


Figure 2.3 (a) X-Ray diffraction pattern of BSZT ceramics with different amounts of Sr content and (b) X-Ray diffraction pattern of BSZT ceramics (110) peak with different amounts of Sr content.



Table 2.1 Lattice constants of BSZT ceramics.

	x=0	x=0.05	x=0.15	x=0.25	x=0.35	x=0.45
a(Å)	4.019(6)	4.004(4)	4.003(2)	3.991(0)	3.969(6)	3.968(1)
c(Å)	4.040(6)	4.029(7)	4.002(8)	3.995(6)	3.968(8)	3.967(5)
Volume of the unit cell(Å ³)	65.283	64.618	64.147	63.641	62.539	62.460

Scanning electron microscopy (JSM 6700F) was used to observe the microstructure of the sintered samples. The top surface of the sample was observed after a thin layer of gold coating was deposited.

Microstructures of the BSZT ceramics are shown in Figure 2.4 (a) – (c). The SEM micrographs indicate that dense samples are obtained, and it is noted that the grain size decreases with increase in Sr content. The smaller grains merge with each other at low Sr content and grow into larger ones thereby increasing the fraction of the larger grains in the overall microstructure.

2.3.3 Dielectric properties

Dielectric properties of the ceramic samples include the relative permittivity ϵ_r and dielectric loss $\tan\delta$. The temperature dependent dielectric properties were characterized with a multi-frequency LCR meter (Model SR720 of Stanford Research System) equipped with a temperature controlled chamber (Oxford). A computer equipped with IEEE control cards was used to control the equipment in the dielectric measurement. The dielectric constant was calculated using the equation:

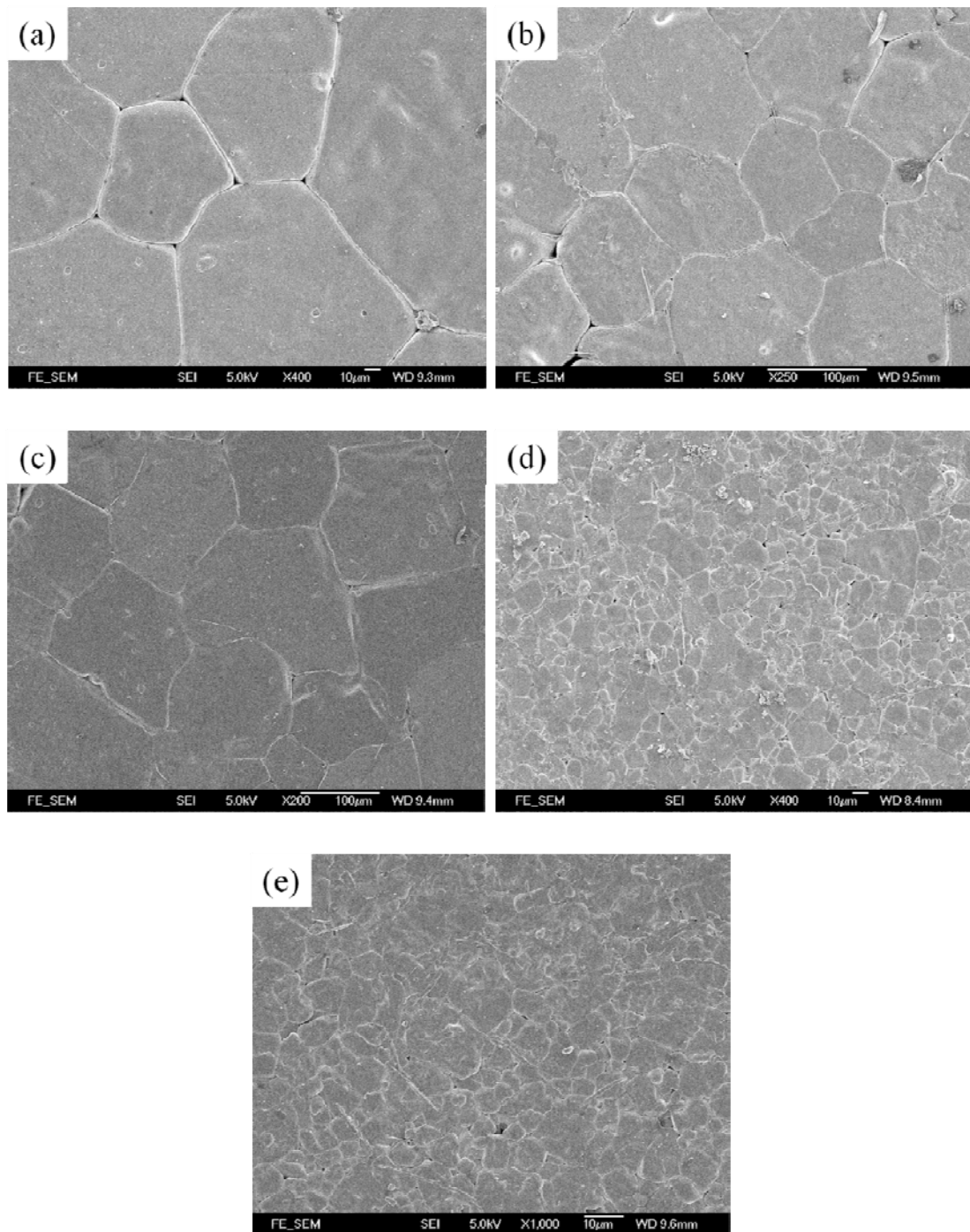


Figure 2.4 (a) – (e) SEM micrographs of BSZT ceramics with different concentrations of Sr. (a) $x = 0$, (b) $x = 0.15$, (c) $x = 0.25$, (d) $x = 0.35$, (e) $x = 0.45$.



$$\varepsilon = \frac{Cd}{A\varepsilon_0} \quad (2.2)$$

where C is the measured capacitance (F), d the thickness (m) of the ceramics, ε_0 the permittivity of the free space (8.85×10^{-12} F/m) and A is the area of the electrode.

Dielectric materials absorb electrical energy under an alternating electric field and thus have dielectric loss. The relative permittivity can be expressed in a complex form:

$$\varepsilon_r = \varepsilon' - \varepsilon'' \quad (2.3)$$

where ε' is the real part of permittivity and the ε'' is the imaginary part of the permittivity. The dielectric loss is given by the following equation

$$\tan\delta = \frac{\varepsilon''}{\varepsilon'} \quad (2.4)$$

Figure 2.5 shows the temperature dependence of the dielectric constant in the BSZT ceramics measured at 1kHz. The Curie transition peaks are found in the range between -6°C to 97°C . Dielectric constant of the sample has a maximum at the Curie temperature. With the increase in Sr content, the Curie temperature decreases linearly. (inset of Figure 2.5(a)). A peak corresponding to this transition can also be observed in the dielectric loss against temperature diagram as shown in Figure 2.5(b). From the figure, a linear relation between the Curie temperature and the stoichiometric Sr content can be expressed using

$$T_c = 97 - 230x \quad (2.5)$$

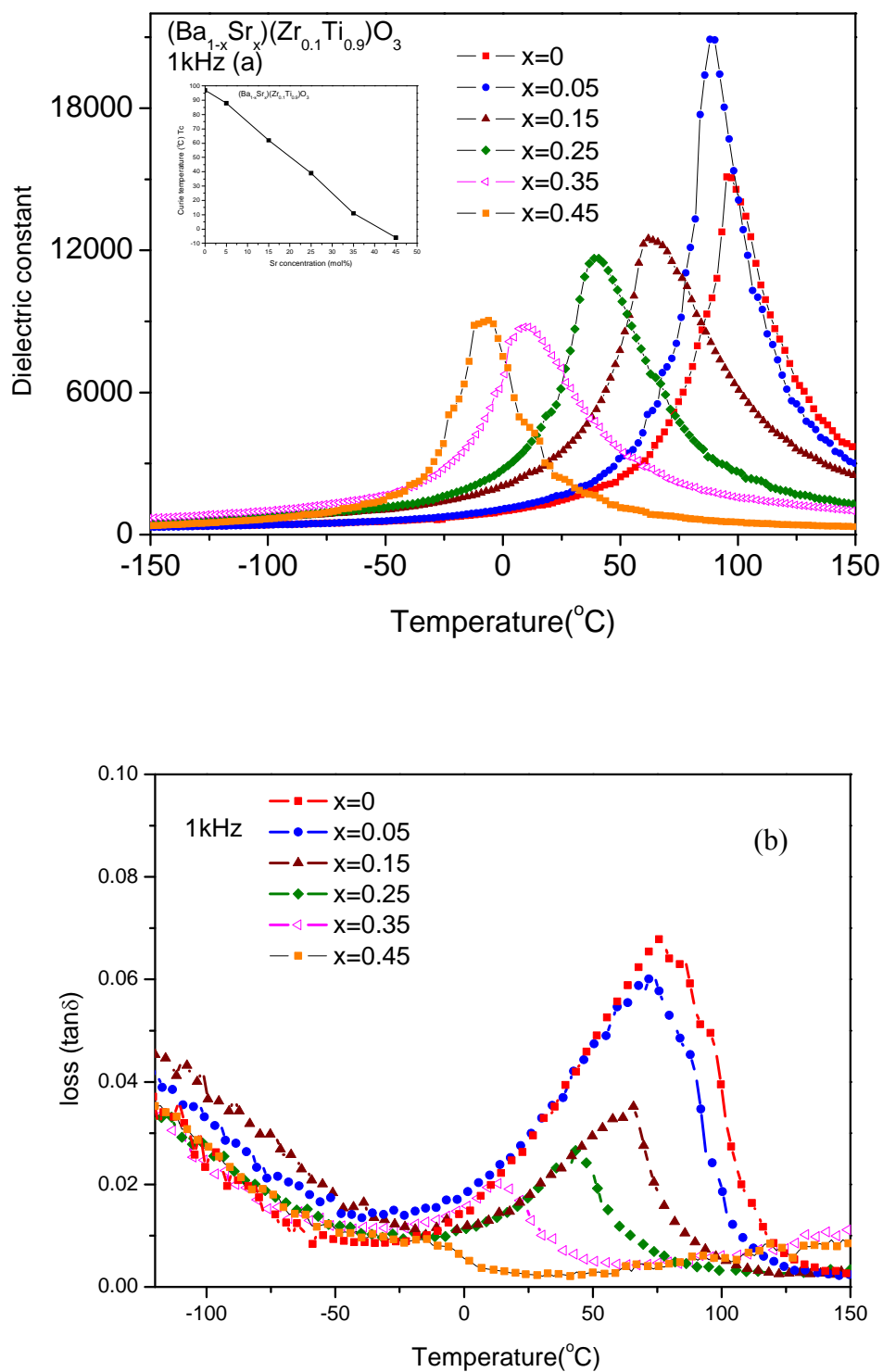


Figure 2.5 Temperature dependence of (a) relative permittivity and (b) dielectric loss measured at 1kHz.

The dielectric properties of this system at 1kHz is shown in Figure 2.6. The dielectric constant ranges from (1458 to 7032). The dielectric loss reaches the lowest values when the Sr content is 45mol%.

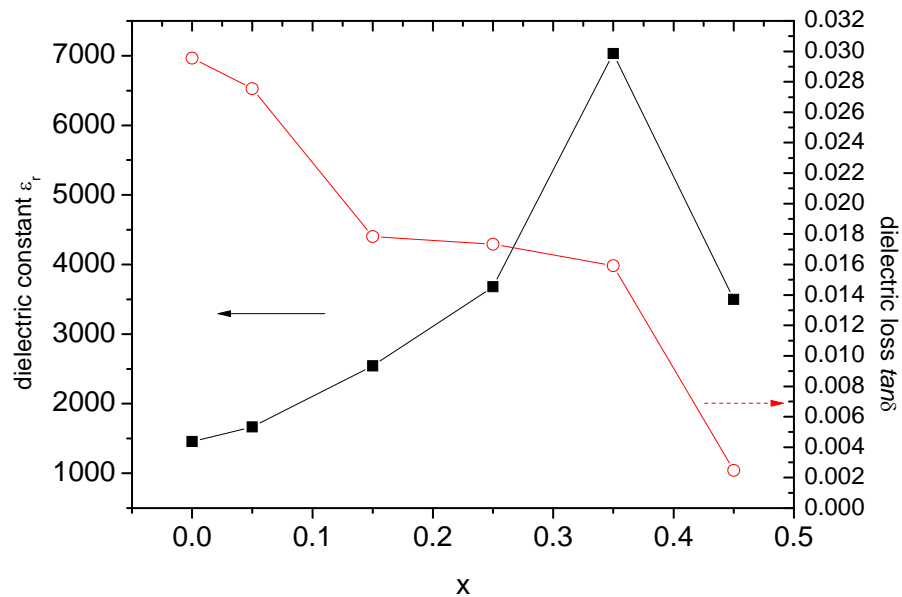


Figure 2.6 Dielectric constant and dielectric loss $\tan\delta$ of the BSZT ceramics measured at 1kHz.

2.3.4 Ferroelectric hysteresis loop measurement

The polarization-electric field (PE) hysteresis loop shows the ferroelectric characteristics of the ferroelectric materials. From the PE loop, the remnant polarization (P_r) and the coercive field (E_c) can be obtained. The loop not only exhibits the ferroelectric properties of the material, but also can provide some references for determining the required DC poling field.

The ferroelectric hysteresis loops are measured using a Sawyer-Tower circuit

(Sawyer and Tower 1930). A typical Sawyer – Tower bridge circuit contains two capacitors C_f and C_{ref} , which are the ferroelectric capacitor (the sample) and a reference capacitor, respectively. In the PE loop measurements, the value of C_{ref} should be much larger than that of C_f (typically around 1000times). The resultant hysteresis loop cannot be formed if this requirement is not satisfied. The schematic experimental setup of the hysteresis loop measurement is shown in Figure 2.7.

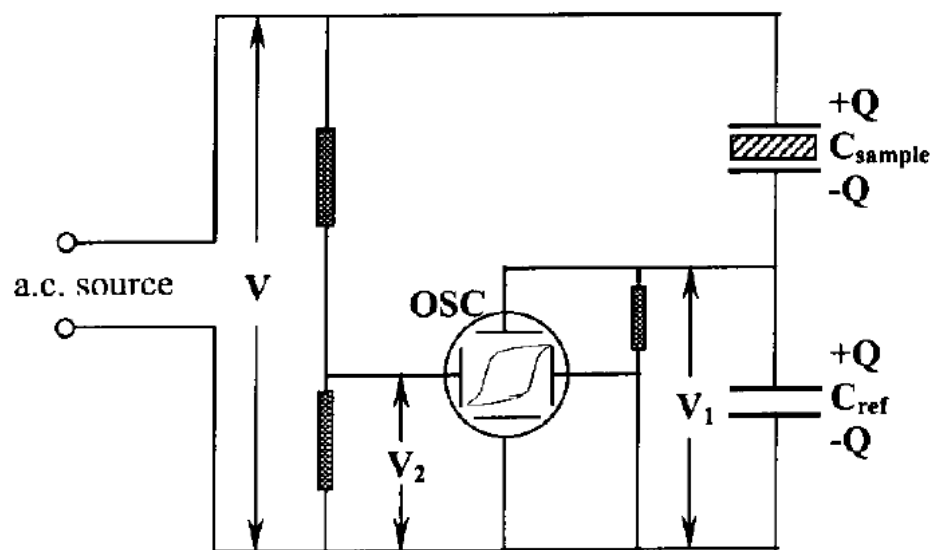


Figure 2.7 A schematic diagram of the Sawyer-Tower bridge for the hysteresis loop measurement (Sawyer and Tower 1930).

The setup is controlled by a computer. During the measurement, the sample was placed in a silicone oil bath. An AC signal with designated amplitude was generated by the function generator (HP 8116A). The signal was amplified by a voltage amplifier (Trek 609D-6) before applied to the sample. The input and output signals from the Sawyer Tower circuit were recorded by a digital oscilloscope (HP 5465A). The recorded data were stored in the computer for further analysis.

The polarization-electric field hysteresis loops of the $(\text{Ba}_{1-x}\text{Sr}_x)(\text{Zr}_{0.1}\text{Ti}_{0.9})\text{O}_3$ ceramics were measured at room temperature. The hysteresis loops are shown in Figure. 2.8 and it is seen that for $x \leq 0.25$, the sample is in ferroelectric phase, which is well consistent with the result from temperature dependence of the relativity permittivity and the XRD patterns. The Curie temperature, remnant polarization and coercive field with different compositions are listed in Table 2.2.

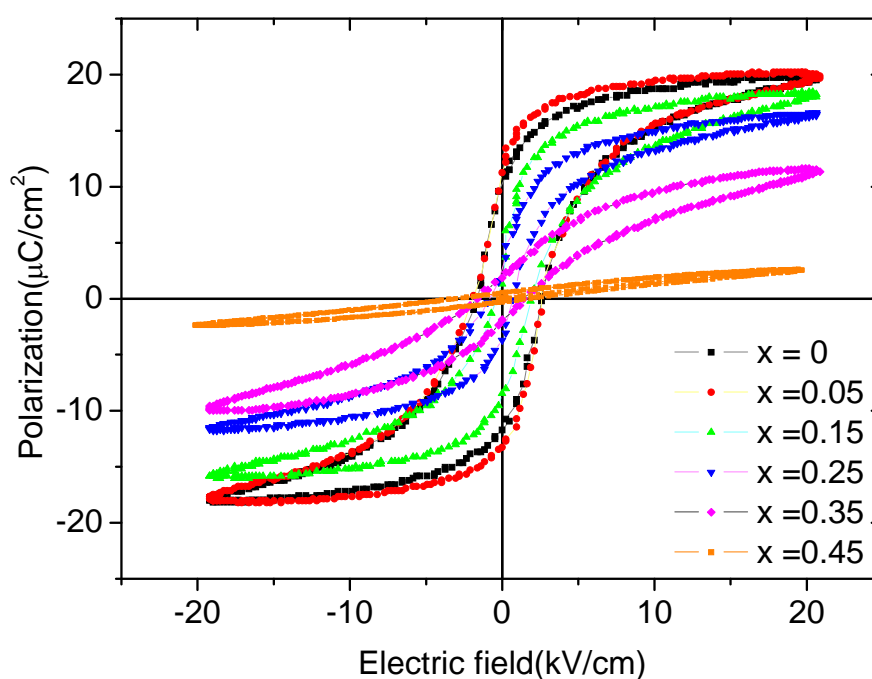


Figure 2.8 P-E hysteresis loops of the $(\text{Ba}_{1-x}\text{Sr}_x)(\text{Zr}_{0.1}\text{Ti}_{0.9})\text{O}_3$ ceramics at room temperature measured at 100Hz.

Clearly, the remnant polarization and coercive electric field decrease as the Sr content increases. The P-E loop becomes slimmer with increase in Sr content. The Curie temperature becomes lower than room temperature, and it transforms to paraelectric phase at room temperature when $x < 0.35$.



Table 2.2 List of Curie temperature, remnant polarization, and coercive field of BSZT ceramics.

Composition	T _c (°C)	Remnant Polarization(μC/cm ²)	Coercive field(kV/cm)
x=0	97	11.63	2.57
x=0.05	88	13.19	2.57
x=0.15	62	8.56	1.18
x=0.25	39	3.83	0.08
x=0.35	8	2.06	0.02
x=0.45	-6	Cannot be determined	Cannot be determined

2.3.5 Piezoelectric properties

The piezoelectric constants related to the mechanical strain produced by an applied electric field are the ‘‘d’’ coefficient. The unit of the ‘‘d’’ coefficient can be expressed in meter per volt or coulomb per newton. The unit comes from the definition of the ‘‘d’’ coefficient.

$$d = \frac{\text{strain}}{\text{applied electric field}} \left(\frac{\text{m}}{\text{V}} \right) = \frac{\text{short circuit charge density}}{\text{applied mechanical stress}} \left(\frac{\text{C}}{\text{N}} \right) \quad (2.6)$$

The piezoelectric d coefficient is closely related to the mechanical displacement. Three axes are used to identify the direction in piezoelectric sample. The axes are defined similar to the Cartesian coordinate in which 1,2 and 3 representing the x,y and z directions. The 3-axis is used to indicate the direction parallel to the polarization direction of the sample. The first subscript of d_{ij} represents the direction of the polarization and the second subscript represents the direction of the mechanical stress.

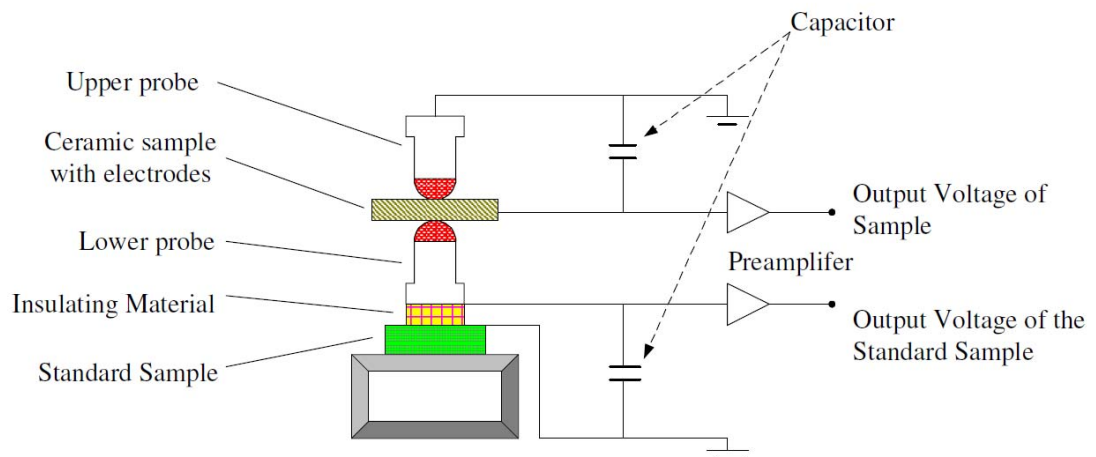


Figure 2.9 Schematic diagram of a d_{33} meter.

Among the d coefficients, only the d_{33} coefficient was measured in the present work. A ZJ-3D d_{33} meter from Beijing Institute of Acoustics is used to measure the d_{33} values. The ceramic sample is placed in between the two probes in the meter and the magnitude of d_{33} can be obtained from the meter directly.

It is important to know the impedance of a piezoelectric material in order to match the impedance between the driving circuit and the transducer. Most properties of the piezoelectric samples can be evaluated by using the impedance and phase versus frequency spectra, which are measured by an impedance/ gain phase analyzer (Agilent 4294A).

When a poled piezoelectric sample disc is subjected to an a.c signal, vibrational modes are excited. Two vibrational modes, the radial (f_{rr}) and thickness (f_{tt}) modes and their harmonics of a piezoelectric ceramics disc are observed from the impedance spectrum. The behaviour of the piezoelectric material can be characterized in terms of an equivalent circuit with corresponding resonant and anti-resonant frequency.



$$\text{Radial mode } f_{rr} = \frac{1}{2r} \sqrt{\frac{1}{\rho s_{11}^E}} \quad (2.7)$$

$$\text{Thickness mode } f_{rt} = \frac{1}{2t} \sqrt{\frac{1}{\rho s_{33}^E}} \quad (2.8)$$

where $2r$ and t are the diameter and the thickness of the ceramics disc, ρ the density of ceramics and s_{11}^E and s_{33}^E are the elastic compliance of the ceramics material measured under a short circuit condition.

By using the information obtained from the impedance/phase frequency spectra, including the resonance frequency, anti-resonance frequency, impedance at resonance frequency, etc at the corresponding resonance mode, the electromechanical coupling coefficient can be calculated by using the IEEE standard on Piezoelectricity (IEEE 1996). The planar electromechanical coupling coefficient k_p can be calculated.

The piezoelectric properties of the samples have been measured after DC poling. The poling field of the sample depends on its coercive field measured in PE loop. The poling field of the BSZT ceramics is 3kV/cm at room temperature for 30min.

The piezoelectric constant d_{33} increases with increasing $x = 0.15$ to 215pC/N and then decreases rapidly, for ceramics with composition $x = 0.35$ and when $x = 0.45$, no piezoelectric properties were observed, as the ceramics are in paraelectric phase at room temperature. The planar electromechanical coupling factor k_p changes as a function of x with a trend similar to the piezoelectric constant d_{33} , with maximum value of 28.9% at $x = 0.15$.

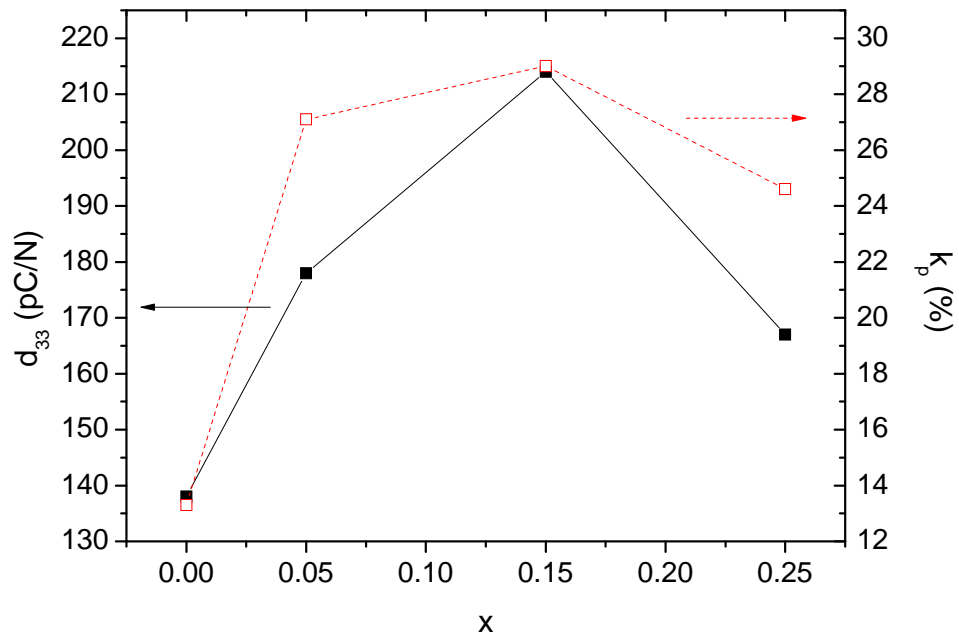


Figure 2.10 Piezoelectric constant d_{33} and planar electromechanical coupling factor k_p of the BSZT ceramics.

2.3.6 Tunability measurements

For microwave (MW) an important property in the ferroelectric circuit elements is the dependence of their dielectric permittivity (ϵ) on the applied biased electric field (E). This characteristic is commonly known as tunability (K) defined as below:

$$K(\%) = \left\{ 100 \times \left(\frac{\epsilon(0) - \epsilon(V)}{\epsilon(0)} \right) \right\} \% \quad (2.9)$$

where $\epsilon(0)$ and $\epsilon(V)$ represent the relative permittivity at zero and non-zero electric field. The dielectric loss in ferroelectrics is not as negligibly small as that of many common microwave dielectric ceramics. Dielectric loss tangent ($\tan\delta$) must be taken into account while designing a MW circuit using ferroelectric materials. The temperature dependence of the dielectric permittivity at the operation temperature



THE HONG KONG POLYTECHNIC UNIVERSITY

interval is another important issue. Usually there is a trade-off between tunability and loss tangent and the MW engineer has to judiciously choose the material with the optimal trade-off between these two parameters for a better device performance. This optimal trade off may be found by a parameter called the figure of merit (FOM) given by:

$$\text{FOM} = (\text{tunability}/\text{loss tangent}) \quad (2.10)$$

To obtain a high FOM, ferroelectric materials used in MW devices are in their paraelectric state close to the Curie temperature to ensure high dielectric permittivity, tunability and low loss tangent. One must realize, however, the figures of merit are of limited use when comparing materials because the figure of merit calculation may change dramatically depending on the application of interest.

The capacitance was also measured under various DC bias by using the blocking circuit, shown in the Figure 2.11, to protect the equipment, including a multi-frequency LCR meter (Model SR720 Stanford Research System) and a DC power source (Keithley 6517A). All the measurements were performed at room temperature and with a small AC amplitude of 0.5V, while the electric field was swept from (20kV/cm) to (-20kV/cm).

To further study the possible applications of BSZT ceramics in tunable capacitor, the dielectric constant as a function of biased electric field is studied. The curves in Figure 2.12 are measured at 100 kHz with a cycling of DC biased electric field range between 0 to ± 20 kV/cm. With the application of electric field, the dielectric constant decreases gradually.

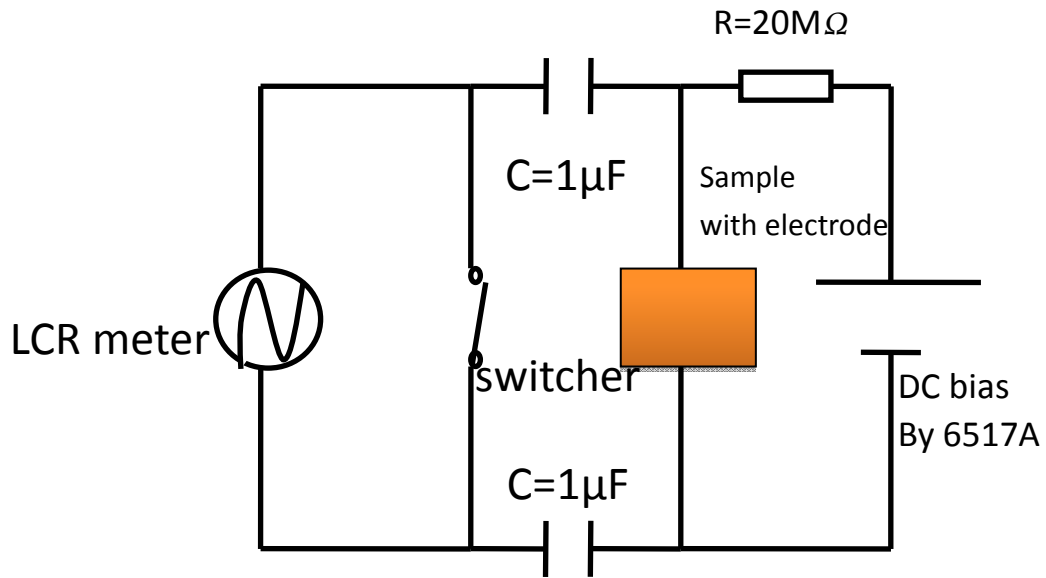


Figure 2.11 Schematic diagram of tunability measurements.

The tunability and figure of merit (FOM) of the ceramics as defined in Equation (2.8) and (2.9) have been summarized in Table 2.3.

Table 2.3 List of the tunability of BSZT ceramics under 20kV/cm.

	x=0	x=0.05	x=0.15	x=0.25	x=0.35	x=0.45
Tunability	58%	56%	68%	79%	51%	55%
$\tan\delta$ @Room temperature	0.02957	0.02755	0.01784	0.01733	0.01592	0.00247
FOM	19.6	20.3	38.1	45.6	32.0	222.7
ϵ at room temperature	1458	1666	2544	3678	7032	3500

The highest tunability of 79% was obtained from $x = 0.25$, however, due to the high dielectric loss of the ceramics, the FOM is low compared with $x = 0.45$. The result suggests that BSZT ceramics with $x = 0.45$ is a promising candidate for tunable

microwave tunable device applications.

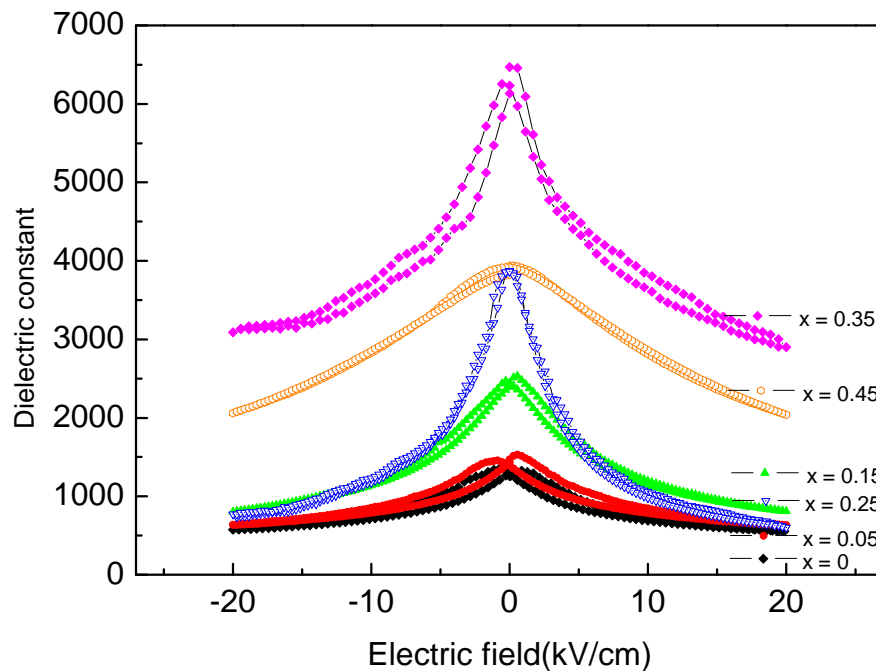


Figure 2.12 Dielectric constant as a function of DC biased electric field of

$(\text{Ba}_{1-x},\text{Sr}_x)(\text{Zr}_{0.1},\text{Ti}_{0.9})\text{O}_3$ ceramics at room temperature measured at 100kHz.

The mechanism of the relationship between relative permittivity and external DC biased field is not clear yet. To obtain a better insight into the problem, it is necessary to use the Johnson's formula (Johnson 1962) to fit the ϵ -E curves. Since the ϵ -E dependence to the ferroelectric materials (when in the paraelectric state) is generally found to follow this equation.

The explicit functional dependence of the relative permittivity on the applied electric field can be derived based on the phenomenological theory of Devonshire. In this treatment, for unstressed crystals, the free energy density is expanded in even powers of the polarization (P) developed by the electric field, i.e.



THE HONG KONG POLYTECHNIC UNIVERSITY

$$g(T, P) = g(T, 0) + \frac{(T-T_0)}{2\varepsilon_0 C} P^2 + \frac{1}{12} B(T) P^4 + \dots \quad (2.11)$$

where $g(T, 0)$ is the zero field free energy density. T is the absolute temperature, C and T_0 are the Curie-Weiss constant and temperature, $B(T)$ is a phenomenological constant, and ε_0 is the permittivity of the vacuum. The electric field is given by

$$E = \left(\frac{\partial f}{\partial P}\right)_T = \frac{(T-T_0)}{\varepsilon_0 C} P + \frac{1}{3} B(T) P^3 + \dots \quad (2.12)$$

The incremental dielectric permittivity $\varepsilon_r(T, E)$ is approximately given by

$$\frac{1}{\varepsilon_r(T, E)} \cong \varepsilon_0 \left(\frac{\partial E}{\partial P}\right)_T = \frac{1}{\varepsilon_r(T, 0)} + \varepsilon_0 B(T) P^2 + \dots \quad (2.13)$$

where $\varepsilon_r(T, 0) = \frac{C}{(T-T_0)}$ is the dielectric permittivity in the absence of a DC electric field. In the equation, it is assumed that $\varepsilon_r(T, E) \gg 1$, which is the case for most ferroelectric materials. For a second order phase transition, the decrease in dielectric permittivity as the electric field is increased is consistent with a positive value of the phenomenological coefficient B . Using the above equation, Johnson proposed an expression for the dielectric permittivity in terms of the electric field. First, considering the case of low field, then the terms in P^4 or higher can be neglected. Assuming that $P = \varepsilon_r \varepsilon_0 E$, then the equation can be written as

$$\frac{1}{\varepsilon_r(T, E)} = \frac{1}{\varepsilon_r(T, 0)} + \varepsilon_0^3 \varepsilon_r^2 B(T) E^2 + \dots \quad (2.14)$$

The equation can be further written as

$$\left[\left(\frac{\varepsilon_r(0)}{\varepsilon_r(E)}\right)^3 - \left(\frac{\varepsilon_r(0)}{\varepsilon_r(E)}\right)^2 + 1 \right] = [1 + \varepsilon_0^3 \varepsilon_r^2 B(T) E^2] \quad (2.15)$$

$$\frac{\varepsilon_r(T, E)}{\varepsilon_r(T, 0)} = \frac{\left(1 - \frac{\varepsilon_r}{\varepsilon_0} + \frac{\varepsilon_r^3}{\varepsilon_0^3}\right)^{\frac{1}{3}}}{[1 + (\varepsilon_0 \varepsilon_r(T, 0))^3 B(T) E^2]^{\frac{1}{3}}} \quad (2.16)$$

We can further assume the numerator to be unity as $1 - \frac{\varepsilon_r}{\varepsilon_0}$ can be neglected compared to $\frac{\varepsilon_r^3}{\varepsilon_0^3}$, therefore, the equation becomes,



$$\varepsilon_r(T, E) = \frac{\varepsilon_r(T, 0)}{\{1 + [\varepsilon_0 \varepsilon_r(T, 0)]^3 B(T) E^2\}^{\frac{1}{3}}} \quad (2.17)$$

2.4 Summary

The $(\text{Ba}_{1-x}\text{Sr}_x)(\text{Zr}_{0.1}\text{Ti}_{0.9})\text{O}_3$ ceramics with $x=0, 0.05, 0.15, 0.25, 0.35$ and 0.45 were successfully prepared by a solid state reaction process, the average grain size of this ceramics ranged from $100\mu\text{m}$ to submicron size. The microstructure, ferroelectric and piezoelectric properties of the ceramics were investigated and the result were summarized in Table 2.4.

The results show that all the BSZT ceramics have perovskite crystal structure. The lattice parameter decreases with increase in Sr content. With the increase in Sr content, the density decreases. The temperature dependent dielectric constant shows that the Curie temperature decreases with increase in Sr content and located between -6°C to 97°C . The relationship of the Curie temperature can be fitted according to the equation $T_c = 97 - 230x$, where x is concentration of the Sr content.

The piezoelectric properties of the BSZT ceramics were systematically characterized. The piezoelectric coefficient d_{33} ($\sim 215\text{pC/N}$) and planar electromechanical coupling coefficient k_p (~ 0.271) was measured for $(\text{Ba}_{0.85}\text{Sr}_{0.15})(\text{Zr}_{0.1}\text{Ti}_{0.9})\text{O}_3$ ceramics.

High tunability of the ceramics was obtained at 20kV/cm , which implies that BSZT ceramics is a promising candidate for microwave applications.



Table 2.4 Lattice parameter, Curie transition temperature, remnant polarization, coercive field, tunability, dielectric loss, figure of merit, d_{33} and planar electromechanical coefficient k_p .

Composition	x=0	x=0.05	x=0.15	x=0.25	x=0.35	x=0.45
Density(kg/cm ³)	5862	5832	5809	5683	5590	5562
a(Å)	4.019(6)	4.004(4)	4.003(2)	3.991(0)	3.969(6)	3.968(1)
c(Å)	4.040(6)	4.029(7)	4.002(8)	3.995(6)	3.968(8)	3.967(5)
Volume of the lattice(Å ³)	65.283	64.618	64.147	63.641	62.539	62.460
T _c (°C)	97	88	62	39	8	-6
Remnant Polarization (μC/cm ²)	11.63	13.19	8.56	3.83	2.06	Cannot be determined
Coercive field (kV/cm)	2.57	2.57	1.18	0.08	0.02	Cannot be determined
ε	1458	1666	2544	3678	7032	3500
Tunability(at E=20kV/cm)	58%	56%	68%	79%	51%	55%
Dielectric loss	0.02957	0.02755	0.01784	0.01733	0.01592	0.00247
FOM	19.6	20.3	38.1	45.6	32.0	222.7
d ₃₃	138	178	214	167	Cannot be determined	Cannot be determined
k _p (%)	13.3	27.1	29	24.6	Cannot be determined	Cannot be determined



CHAPTER 3

TECHNIQUES FOR DEPOSITION AND STRUCTURAL CHARACTERIZATION OF BSZT THIN FILMS

3.1 Introduction

BST and BZT thin films have been successfully grown on various substrates via different deposition techniques, including pulsed laser deposition (PLD) (Ying et al. 2007; Zhu et al. 2007; Qin et al. 2008), RF magnetron sputtering (Xiao et al. 2009; Xu et al. 2009; Yang et al. 2010) and sol gel deposition. (Cheng et al. 2006; Gao et al. 2008) Among them, PLD is the most extensively used technique for growing epitaxial BST and BZT thin films.

PLD has some unique advantages over other deposition techniques. For example, PLD can be utilized to fabricate high quality epitaxial oxide films at a relatively low deposition temperature (500-600°C). Thin films of high T_c superconducting oxides (Cheung et al. 1993), nitride (Vispute et al. 1995), ferroelectric (Ramesh et al. 1991), metallic multilayers and various superlattices (Seong et al. 2006) have been realized by these methods.

In the present work, $(\text{Ba}_{1-x}\text{Sr}_x)(\text{Zr}_{0.1}\text{Ti}_{0.9})\text{O}_3$ (BSZT) thin film were deposited by pulsed laser deposition. By the X-ray diffraction technique, the structure and the crystalline quality were studied. In order to study the effect of lattice mismatch and thermal expansion mismatch, $(\text{Ba}_{0.55}\text{Sr}_{0.45})(\text{Zr}_{0.1}\text{Ti}_{0.9})\text{O}_3$ thin film were also deposited on various substrates including $(\text{LaAlO}_3)_{0.3}(\text{Sr}_2\text{AlTaO}_6)_{0.35}$ (001) [abbreviated as



THE HONG KONG POLYTECHNIC UNIVERSITY

LSAT(001)], LaAlO_3 [abbreviated as LAO (001)] and MgO.

An increase in the surface roughness cause poor electrode –film interface and give rise to high dielectric loss in thin film for microwave application. Therefore, the variation of the surface morphology, grain size and roughness of the $(\text{Ba}_{1-x}, \text{Sr}_x)(\text{Zr}_{0.1}, \text{Ti}_{0.9})\text{O}_3$ thin film were studied using atomic force microscopy.

3.2 Deposition of BSZT thin films

3.2.1 PLD system and setup

The use of a pulsed laser as a directed energy source for evaporative film growth has been explored since the discovery of laser (Ramsey 1969; Smith and Turner 1969). Initial activities were limited in scope and involved both continuous wave (cw) and pulsed lasers. The first experiments in pulsed laser deposition were carried out in the 1960s; limited efforts continued into the 1970s and 1980s. Then, in the late 1980s, pulsed laser deposition was popularized as a fast and reproducible oxide film growth technique through its success in growing in situ epitaxial high temperature superconducting films(England et al. 1988).

Pulsed laser deposition is a physical vapour deposition process, carried out in a vacuum system and a pulsed laser is focused onto a target of the material to be deposited. For sufficiently high laser energy density, each laser pulse vaporizes or ablates a small amount of the material creating a plasma plume. The ablated material is ejected from the target in a highly forward directed plume. The ablation plume provides the material flux for film growth. PLD has proven remarkably effective at



THE HONG KONG POLYTECHNIC UNIVERSITY

yielding epitaxial films. In this case, ablation conditions are chosen such that the ablation plume consists primarily of atomic, diatomic, and other low mass species. This is typically achieved by selecting an ultraviolet (UV) laser wavelength and nanosecond pulse width that is strongly absorbed by a small volume of the target material. Laser absorption by the ejected material creates plasma.

Compared with conventional film deposition techniques, e.g. thermal evaporation, molecular beam epitaxy (MBE), sputtering, metalorganic chemical vapour deposition (MOCVD), etc, laser ablation has the following characteristics (Glocker et al. 1995).

- (i) Materials with high melting points can also be deposited if the materials absorb the laser light
- (ii) It is possible to prepare films in an oxidation environment with relatively high pressure because of the absence of a heater or filament in the deposition chamber.
- (iii) The target composition is transferred to the film, leading to stoichiometric deposition.
- (iv) A large number of droplets of submicron size are often seen on the surface of the deposited film

Atoms and clusters are ejected from the target due to focused laser irradiation and deposited onto substrates. Features of film deposition are governed by the laser employed for the ablation.

During deposition, the target is often rotated to eliminate changes in composition. In order to guide the laser light into the deposition chamber, an incident window



THE HONG KONG POLYTECHNIC UNIVERSITY

should always be transparent to the incoming laser light. If an KrF excimer laser is used for ablation, synthesized quartz is the preferred window material. Occasionally the window material is turned opaque or luminous by the UV laser irradiation. To avoid a reduction of laser fluence onto the target, special care is required.

Introducing oxygen or an inert gas from the window is preferred for eliminating unintentional deposition on the window. In the preparation of the film by laser ablation it is important to control the plume in order to obtain high quality films. The optimum laser fluence for film preparation depends on the substrate target spacing and the ambient gas pressure. The substrate-target spacing is, typically, around 2 -5 cm, depending on the laboratory set up. The crucial point for laser ablation is how the plume interacts with the substrate.

At present, compared with conventional film preparation technique, the homogeneity of the film thickness is not good enough to allow the use of a large area substrate. Small area substrates are preferred for laser ablation. The substrate temperatures are often calibrated by a thermocouple attached to the substrate by silver paste.

Target preparation is also important for the film growth. The target morphology affects the surface morphology of the films. A fresh target surface is preferred because after prolonged irradiation of the target its composition at the ablated surface often deviates from the original stoichiometric one, especially in ablation with a low fluence. A high density target is also required for high quality film without a large amount of droplets.

A schematic diagram of the PLD system used in our laboratory is shown in Figure 3.1. The laser used is a KrF excimer laser with a wavelength of 248nm and pulse duration of 25ns (Lambda Physik COMPex 205). The laser pulse repetition rate is fixed at 10Hz. The laser energy is around 250mJ (energy density of 2-3 J/cm² on the target surface) per pulse. During deposition, the target is rotated so that successive pulses do not hit the same point on the target surface.

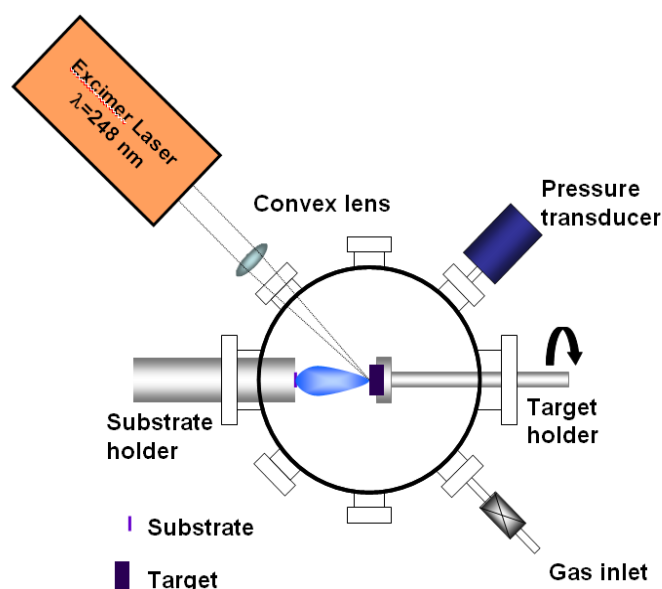


Figure 3.1 Schematic diagram of the pulsed laser deposition system.

Before the deposition, the quartz window was cleaned using abrasive powders. It is a critical step to ensure the entire laser beam enters the chamber with less reflection. After mounting the substrates on the sample holder, the chamber is pumped down to a pressure of 10^{-5} to 10^{-6} Torr using rotary pump and turbo molecular pump. Oxygen (processing gas) pressure is controlled by the pumping valve. The laser beam enters the chamber through the quartz window, by adjusting the position of the convex lens, the pulsed laser beam interacts with the solid target, producing a plume. The plume contains energetic neutral atoms, ions and molecules, which are subsequently

THE HONG KONG POLYTECHNIC UNIVERSITY

transported towards the substrate. Since sufficient ionic mobility is needed for the growth of epitaxial oxide thin films, the substrate is kept at a high temperature (700°C) during the deposition.

3.2.2 Thin film growth modes

A lattice mismatch and surface energy between substrate and film materials is a key parameter to determine the growth mode. Generally in heteroepitaxy, growth mode can be classified into three categories, as shown in Figure 3.2.

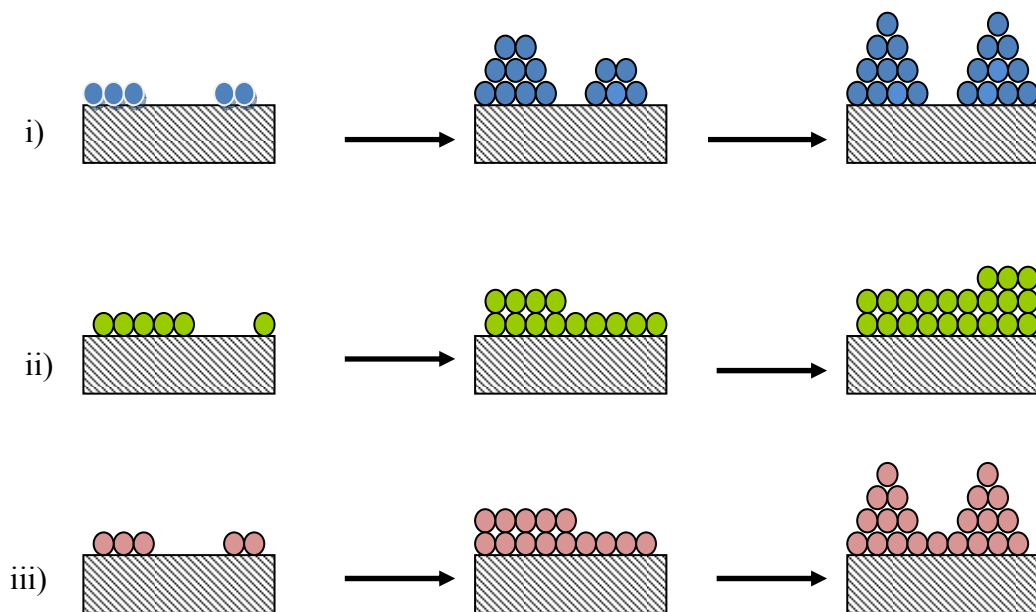


Figure 3.2 Thin film growth mode: (i) Volmer-Weber growth, (ii) Frank-van der Merme mode and (iii) Stranski-Krastinov growth mode (Waser 2005).

Different growth modes of the thin films were shown in Figure 3.2. (i) Volmer-Weber growth or 3D island growth mode involves the film materials being formed as isolated islands on the substrates. (ii) Frank-van der Merme or



layer-by-layer growth mode involves the interatomic interactions between substrate and the film materials are stronger than those between the different atomic species of the film. Monolayer growth is preferred and excellent epitaxy can be obtained; (iii) Stranski-Krastinov growth mode involve a combination of layer by layer mode and 3D island growth modes as described in (i) and (ii). This growth mode is dominated in the early stage.

3.2.3 Deposition of BSZT thin films

In Chapter 2, the dielectric, ferroelectric and structural properties of the BSZT ceramics were studied. The BSZT ceramics were used as target materials for depositing thin films. Different PLD target with diameter 2cm were fabricated by the parameters introduced in Chapter 2. In this work, $(\text{Ba}_{1-x}\text{Sr}_x)(\text{Zr}_{0.1}\text{Ti}_{0.9})\text{O}_3$ thin film with composition ($0 \leq x \leq 0.45$) were deposited on LSAT substrates by PLD. For $(\text{Ba}_{0.55}\text{Sr}_{0.45})(\text{Zr}_{0.1}\text{Ti}_{0.9})\text{O}_3$ ceramics, this ceramics has a cubic structure and is in paraelectric phase at room temperature. The figure of merit for this ceramics is high compared with other compositions, which implies this composition is a potential material for microwave devices application. The $(\text{Ba}_{0.55}\text{Sr}_{0.45})(\text{Zr}_{0.1}\text{Ti}_{0.9})\text{O}_3$ thin films were deposited on various substrates (LSAT, MgO and LAO). The polished single crystal substrates were supplied by Heifei Kejing Materials Technology Co. Ltd. Before deposition, the surface of the substrate was cleaned properly using acetone and ethanol in an ultrasonic bath. The deposition conditions were optimized and the details of the deposition parameters are summarized in Table 3.1.



Table 3.1 Deposition conditions of $(\text{Ba}_{1-x}, \text{Sr}_x)(\text{Zr}_{0.1}, \text{Ti}_{0.9})\text{O}_3$ thin films by pulsed laser deposition.

Target to substrate distance	50mm
Laser Energy	250mJ
Repetition rate of the laser	10Hz
Deposition temperature	700°C
Oxygen partial pressure	200mTorr
Target Materials	Substrate
$\text{Ba}(\text{Zr}_{0.1}, \text{Ti}_{0.9})\text{O}_3$	LSAT(001)
$(\text{Ba}_{0.95}, \text{Sr}_{0.05})(\text{Zr}_{0.1}, \text{Ti}_{0.9})\text{O}_3$	LSAT(001)
$(\text{Ba}_{0.85}, \text{Sr}_{0.15})(\text{Zr}_{0.1}, \text{Ti}_{0.9})\text{O}_3$	LSAT(001)
$(\text{Ba}_{0.75}, \text{Sr}_{0.25})(\text{Zr}_{0.1}, \text{Ti}_{0.9})\text{O}_3$	LSAT(001)
$(\text{Ba}_{0.65}, \text{Sr}_{0.35})(\text{Zr}_{0.1}, \text{Ti}_{0.9})\text{O}_3$	LSAT(001)
$(\text{Ba}_{0.55}, \text{Sr}_{0.45})(\text{Zr}_{0.1}, \text{Ti}_{0.9})\text{O}_3$	LSAT(001)
	MgO(001)
	LAO(001)

3.3 Structural characterization of BSZT thin films by X-Ray diffraction

3.3.1 X-Ray diffraction

X-ray diffraction (XRD) is a common non-destructive method for obtaining the crystalline structure of single crystals, ceramics and thin film. As discussed in Chapter 2, the structural properties of BSZT ceramics can be studied using XRD.

If an incident X-ray beam encounters a crystal lattice, scattering occurs. Diffractions occur in a certain direction when the scattered rays are in phases from specific planes. Under this condition the reflections combine to form new enhanced wave fronts (constructive interference). By varying the incidence angle, the Bragg's law conditions are satisfied by different d spacing's in the polycrystals.

By Bragg's law

$$2d\sin\theta = n\lambda \quad (3.1)$$

where d is the distance between the lattice planes and λ is the wavelength of the X-Ray beam. The integer number n is the order of diffraction.

Rewriting Bragg's law we get:

$$2d_{hkl}\sin\theta = \lambda \quad (3.2)$$

where d_{hkl} is the interplanar spacing of the planes (hkl) and h,k,l are the Miller indices.

Constructive interference exists only for the planes perpendicular to the surface.

The illuminated area and the penetration depth depend on the angle of incidence.

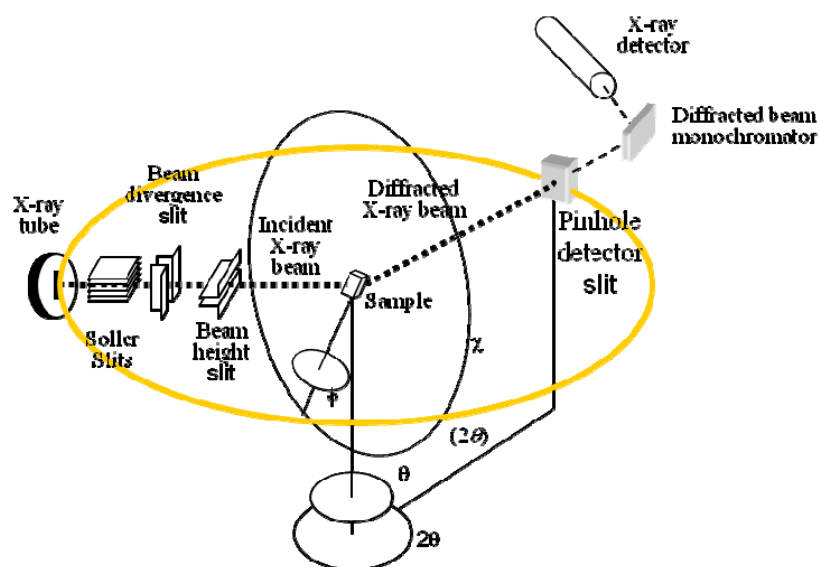


Figure 3.3 Layout of the X-ray diffractometer.

For a tetragonal crystal structure, d_{hkl} is related to lattice parameters a and c , it can be determined by the following equation:

$$\frac{1}{d_{hkl}^2} = \frac{h^2+k^2}{a^2} + \frac{l^2}{c^2} \quad (3.3)$$

The X-ray diffraction measurements on all thin films mentioned in Table 3.1 were carried out in Bruker AXD D8 Discover X-ray diffractometer operating at 40kV and 40mA, and equipped with Cu $K\alpha$ radiation at a wavelength $\lambda=1.540562 \text{ \AA}$. Figure 3.3 shows the schematic diagram of the X-ray diffraction measurement.

The most common mode is called θ - 2θ scan, as shown in Figure 3.4, the sample is rotated by θ and the detector rotated by 2θ .

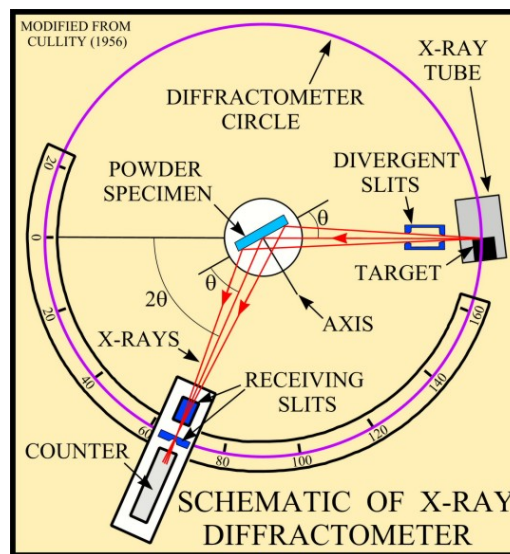


Figure 3.4 Schematic of Bragg- Brentano diffractometer (Cullity 1956).

For example, the θ - 2θ scan for $(\text{Ba}_{0.55}, \text{Sr}_{0.45})(\text{Zr}_{0.1}, \text{Ti}_{0.9})\text{O}_3$ thin film deposited on LSAT is shown in Figure 3.5.

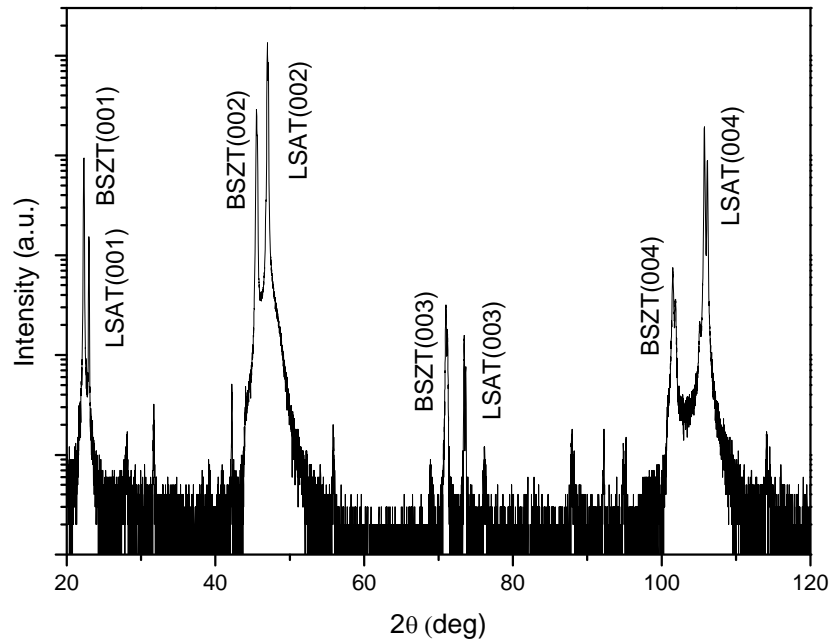


Figure 3.5 XRD θ - 2θ scan pattern of $(\text{Ba}_{0.55},\text{Sr}_{0.45})(\text{Zr}_{0.1},\text{Ti}_{0.9})\text{O}_3$ thin film grown on LSAT(001) at 700°C under an oxygen partial pressure of 200mTorr.

Apart from the reflection of the substrate, only (001) peaks of the thin film appear in the XRD pattern. Therefore, the c -axes of the crystallites in the film are highly oriented along the film normal.

Using the θ - 2θ scan pattern and the Nelson-Riley extrapolation function (Cullity 1956), the out of plane lattice parameter can be determined with high accuracy. The Nelson-Riley function is given by:

$$c = c_0 - c_0 k \left(\frac{\cos^2 \theta}{\sin \theta} + \frac{\cos^2 \theta}{\theta} \right) \quad (3.4)$$

where c is the lattice parameter calculated from the position of the Bragg peak, c_0 the 'true' fitted lattice parameter and k is a fitting parameter. The equation yields $c=c_0$ at $\theta=90^\circ$, thus in practice c is plotted versus $\left(\frac{\cos^2 \theta}{\sin \theta} + \frac{\cos^2 \theta}{\theta} \right)$ and linearly extrapolated

THE HONG KONG POLYTECHNIC UNIVERSITY

to $\theta = 90^\circ$ to obtain $c=c_0$. The major errors in the determination of lattice parameter arise from the misalignment of the instrument, surface shape of the sample, absorption of the sample, displacement of the sample from the diffractometer axis (usually the largest single source of error) and vertical divergence of the incident beam. The use of the Nelson-Riley function can effectively reduce the above systematic errors.

The out of plane lattice parameters c was calculated from the position of the (001) peaks ($l=1-4$) using

$$c = l \cdot d_{00l} \quad (3.5)$$

The out of plane lattice parameters c is plotted against the function $(\frac{\cos^2\theta}{\sin\theta} + \frac{\cos^2\theta}{\theta})$ as shown in Figure 3.6. The data points are least squares fitted to a straight line and the true out of plane lattice parameter c_0 of the thin film can be fitted, obtained from the y intercept, is 3.979 Å.

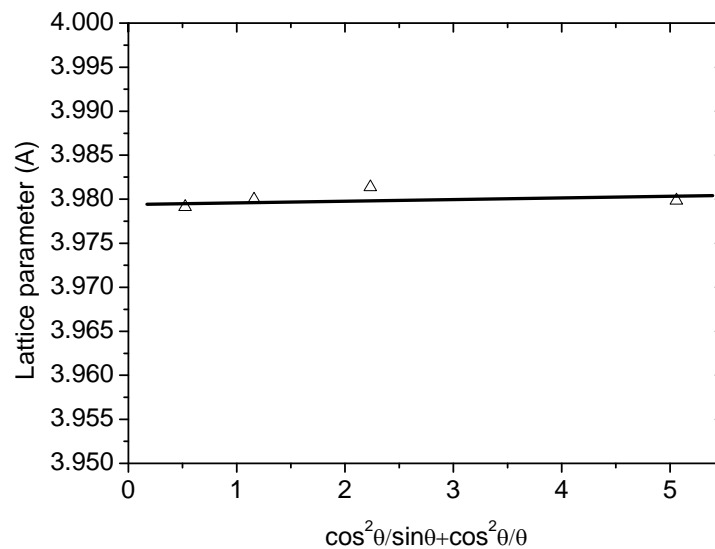


Figure 3.6 The out-of-plane lattice parameter of $(\text{Ba}_{0.55}, \text{Sr}_{0.45})(\text{Zr}_{0.1}, \text{Ti}_{0.9})\text{O}_3$ thin film grown on LSAT(001) substrate fitted to the Nelson-Riley function.



A θ - 2θ scan at $\chi=0$ is only useful for investigating planes parallel to the film surface. To study other lattice planes, it is necessary to incline the sample at an angle χ , these planes are often called oblique planes and we have to estimate the value of χ and then adjust the diffractometer accordingly. By investigating different oblique planes, the in plane lattice parameter can be calculated. e.g. from the θ - 2θ scan pattern of the oblique (202) plane for the thin film grown on LSAT(001) substrate by tilting the sample at an angle of $\chi=45^\circ$. Since the thin films usually having tetragonal structure with symmetry axis along the film normal, the in plane lattice parameter a can be calculated using

$$a = \frac{2}{\sqrt{d_{(202)}^{-2} - \left(\frac{c}{2}\right)^{-2}}} = \frac{2}{\sqrt{d_{(202)}^{-2} - d_{(002)}^{-2}}} \quad (3.6)$$

In ω scan, the sample is fixed at angle θ and the sample is rocked about the ω axis which is in the same direction as the incident X-ray beam. As the angle ω rocks, strong diffraction only occurs when Bragg's law is matched. The full width at half maximum (FWHM) of the diffraction curve can thus be used to determine the quality of the film orientation. The rocking curve can give the degree of random orientation of the crystal grains with each other in the film. Films having better aligned grains give narrow diffraction peaks.

In φ scan, the sample is fixed at angle θ and rotates 45° about the ω axis. The sample is turned about the φ axis through 360° . Since strong signal is detected only when Bragg's law is matched, this scanning mode can reveal the spatial distribution of the atom inside the material.



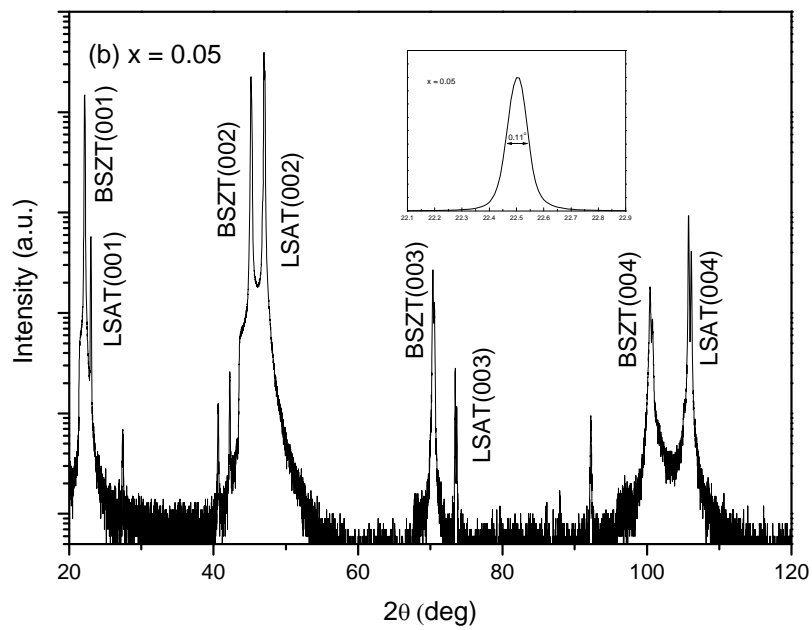
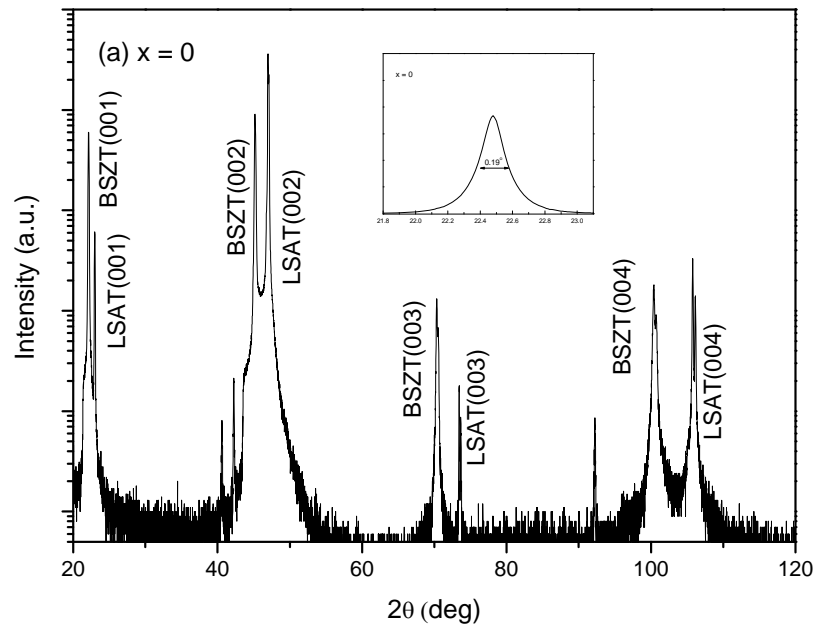
The full width at half maximum (FWHM) of the ω scan peaks for the (002) reflections were determined. These indicate the films are strongly aligned out of plane.

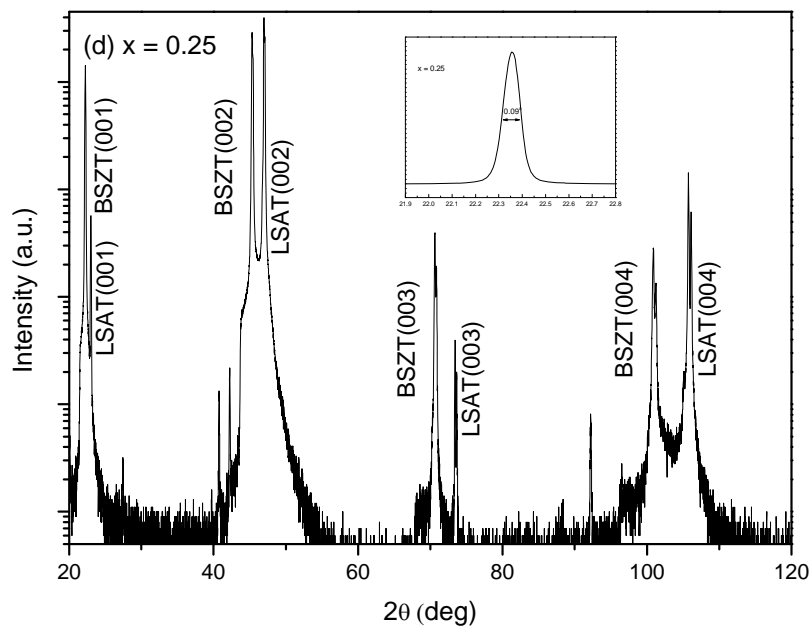
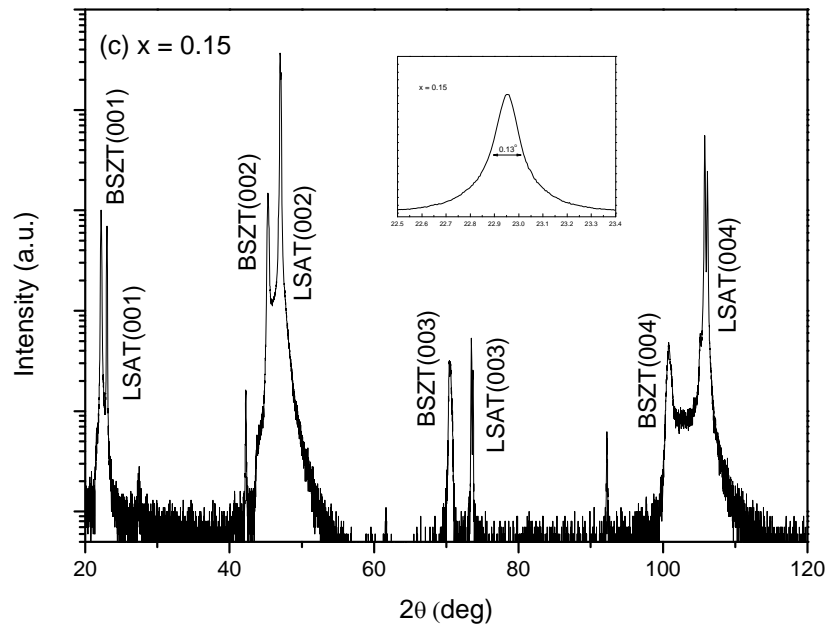
The off axis ϕ scans of (202) diffraction of the thin films were performed to understand the quality of the epitaxy and to determine the in plane relationship between the film and the substrate. The four fold symmetric (202) diffraction of the films are very sharp and coincide well with those LSAT (001) substrate. Suggesting all the films have a high degree of in plane orientation and exhibit an epitaxial growth on the LSAT substrate.

3.3.2 Compositional dependence

$(\text{Ba}_{1-x}, \text{Sr}_x)(\text{Zr}_{0.1}, \text{Ti}_{0.9})\text{O}_3$ thin films with ($0 \leq x \leq 0.45$) were deposited according to the condition in Table 3.1. Using XRD, the structural properties of the thin films were characterized. Figure 3.7(a)-(f) shows the XRD θ - 2θ scan patterns for the BSZT thin films on LSAT substrate. As revealed from the Figure, only (001) peaks are observed, which implies the BSZT films on LSAT substrates have a perovskite phase and highly c-axis oriented.

From the inset of each figure, the full width at half maximum (FWHM) of the ω -scan peaks of BSZT (002) reflection is shown. The grain orientation is a key factor to determine the quality of the thin films. The FWHM values of the BSZT thin films are below 0.25° , which indicates that all thin films are having high degrees of grain orientation.





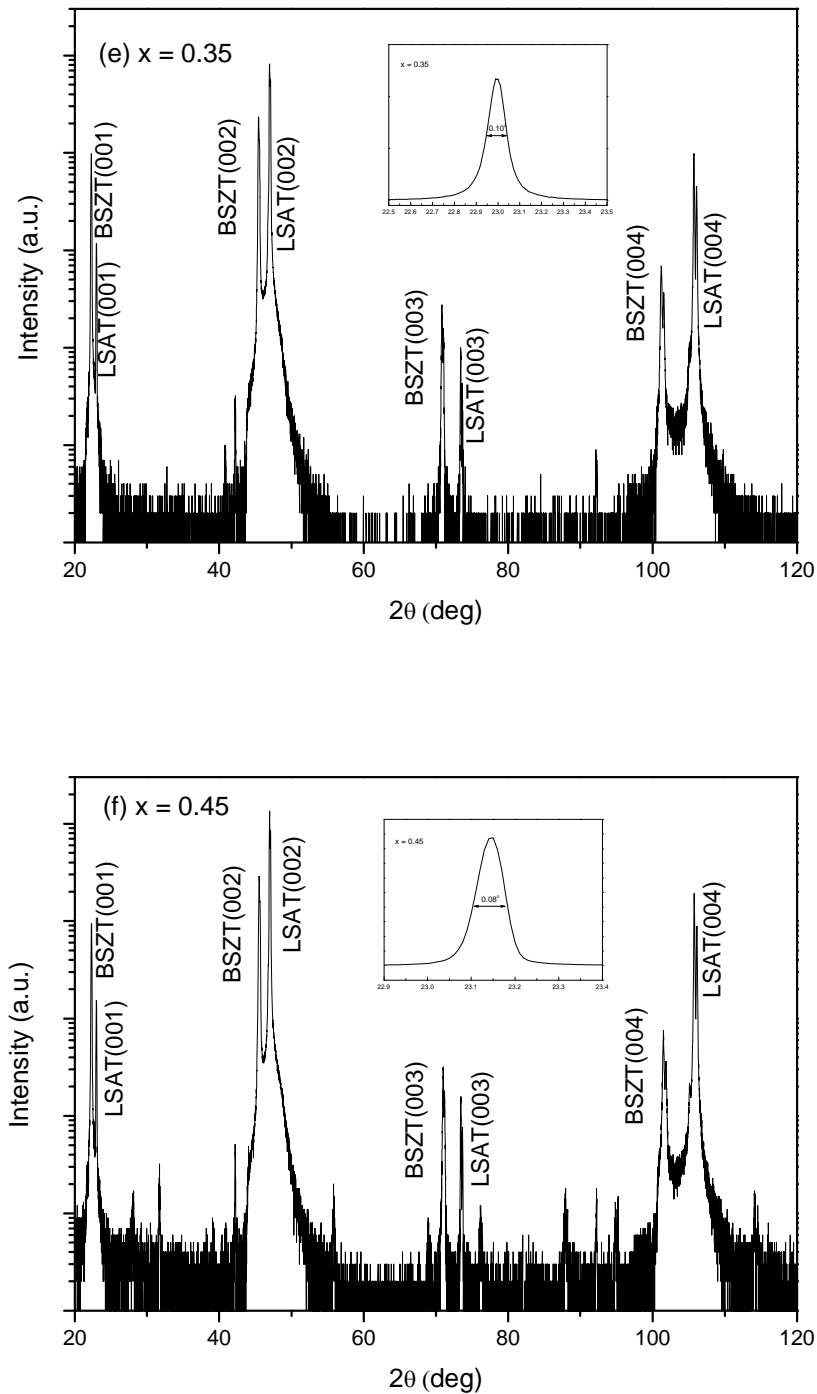


Figure 3.7 XRD θ - 2θ scan pattern of $(\text{Ba}_{1-x}\text{Sr}_x)(\text{Zr}_{0.1}\text{Ti}_{0.9})\text{O}_3$ thin film grown on LSAT(001) under the conditions listed in Table 4.1. (a) $x = 0$, (b) $x = 0.05$, (c) $x = 0.15$, (d) $x = 0.25$, (e) $x = 0.35$, (f) $x = 0.45$ (inset: ω - scan of the thin films).

From Figure 3.8, the XRD patterns for all BSZT thin films deposited on LSAT are shown in the range of 44° to 48° . Within this range, the peaks for BSZT(002) and LSAT(002) can be observed clearly. It is noted that, with the increase in Sr content, the diffraction peaks of BSZT (002) shifts to higher angles. It indicates that the lattice parameter along the c – axis decreases. The lattice parameter c can be calculated using the Nelson-Riley extrapolation function.

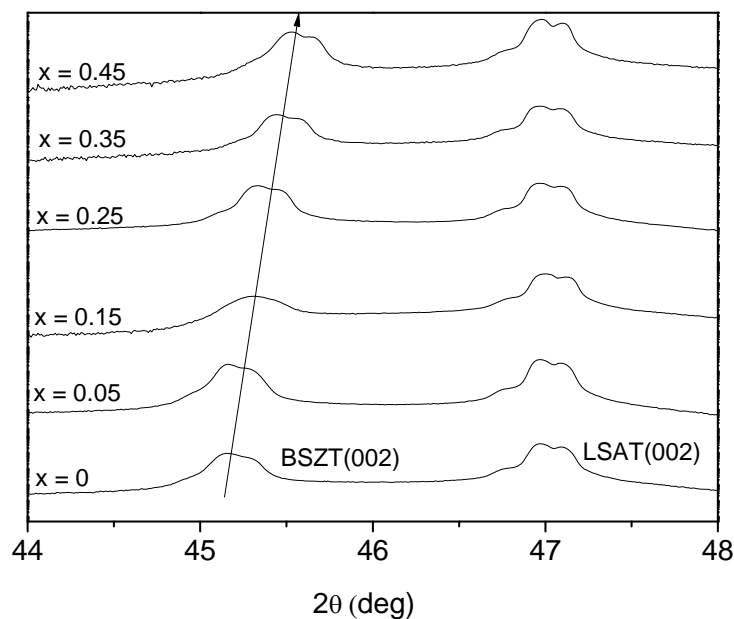


Figure 3.8 XRD θ - 2θ scan patterns of $(\text{Ba}_{1-x},\text{Sr}_x)(\text{Zr}_{0.1},\text{Ti}_{0.9})\text{O}_3$ thin film grown on LSAT(001) substrates.

To determine all the lattice parameters of the thin film, it is necessary to determine the θ - 2θ scan patterns for $\chi=45^\circ$. From Figure 3.9, the BSZT (202) diffraction peaks shifts to the higher angle, having the same trend as mentioned for BSZT (002) peaks. Indicates that the lattice parameters a and b decreases with the increase in Sr content.

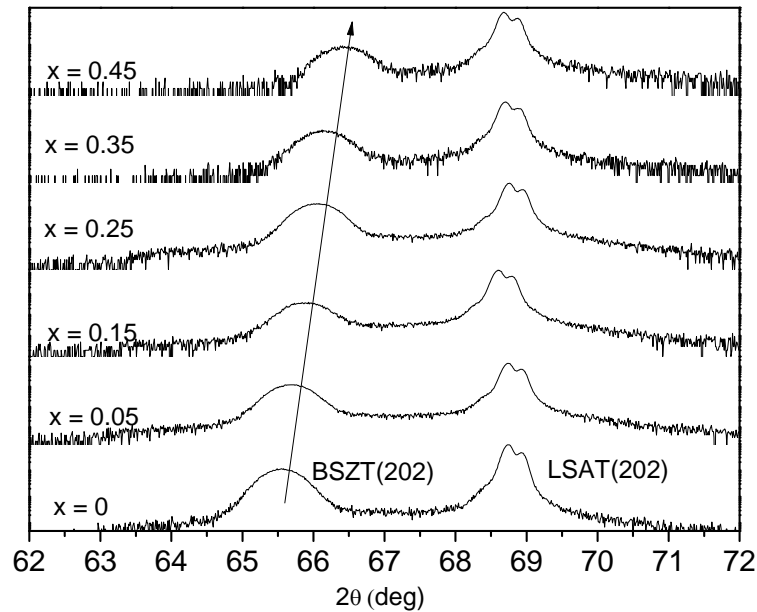


Figure 3.9 XRD θ - 2θ scan pattern of $(\text{Ba}_{1-x}\text{Sr}_x)(\text{Zr}_{0.1}\text{Ti}_{0.9})\text{O}_3$ thin film grown on LSAT(001) substrates with $\chi=45^\circ$.

The lattice parameters of the thin films were determined from the XRD results θ - 2θ scan patterns and θ - 2θ scan with $\chi=45^\circ$, the results of the lattice parameter are summarized in Table 3.2

All the thin films show tetragonally distorted lattice structure, which is different from the lattice parameters calculated for the constituent ceramics, indicating that structure of the films have been modified by the substrates. The out-of-plane and in plane lattice parameter decreases with the increase in Sr content, which is in agreement with the trend we found in Chapter 2, since the ionic radius of Ba^{2+} (1.61\AA) is larger than that of Sr^{2+} (1.44\AA), more Sr^{2+} ions substituted for the Ba^{2+} ions as the Sr content increases, resulting in the decrease in lattice parameter.



Table 3.2 Lattice parameters of the $(\text{Ba}_{1-x}\text{Sr}_x)(\text{Zr}_{0.1}\text{Ti}_{0.9})\text{O}_3$ thin film grown on LSAT(001) substrates (with $\chi = 45^\circ$).

Composition	Lattice parameter(Å)	
	Out-of-plane c	In-plane-a
x = 0	4.0118	4.0366
x = 0.05	4.0113	4.0248
x = 0.15	4.0021	4.0115
x = 0.25	3.9980	3.9952
x = 0.35	3.9881	3.9861
x = 0.45	3.9799	3.9770

Figure 3.10 shows the tetragonality a/c and unit cell volume a^2c of BSZT thin film deposited on LSAT(001) substrates as a function of Sr content x . The a/c ratio indicates the tetragonal distortion of the films, it decreases monotonically with the increase in Sr content. Oriented $\text{Ba}_{1-x}\text{Sr}_x\text{TiO}_3$ thin films deposited by PLD on (001) single crystal substrates with cubic structure show deviations from the expected cubic structure (Canedy et al. 2000; Chen et al. 2002; Navi et al. 2003). These deviations are caused by the strain generated as a result of the difference between the lattice parameters and difference between the thermal expansion coefficients of the film and the substrate, and the presence of oxygen vacancies.

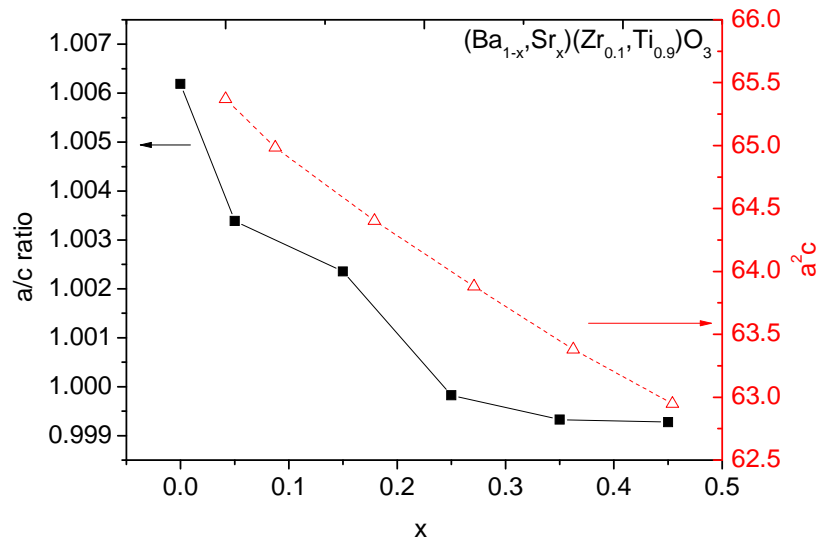


Figure 3.10 Tetragonality a/c and unit cell volume a^2c of BSZT thin films deposited on LSAT(001) substrates as a function of Sr content x .

The off axis phi scan of the (202) diffraction of BSZT thin film, as shown in Figure 3.11, has been performed to determine the in-plane crystallographic relationship between the film and the substrate. The specimen is first tilted 45° along the axis relative to the normal plane, and angles are set to the particular angles for specific planes. Then a 360° scan is performed to investigate the peaks appeared and identifies its four-fold symmetric feature, peaks of all the BSZT thin film coincide well with those of LSAT substrates. The peaks are separated by 90° , which shows the four-fold symmetric features. The in-plane orientation relationship has been determined to be $\langle 100 \rangle_{\text{BSZT}} // \langle 100 \rangle_{\text{LSAT}}$.

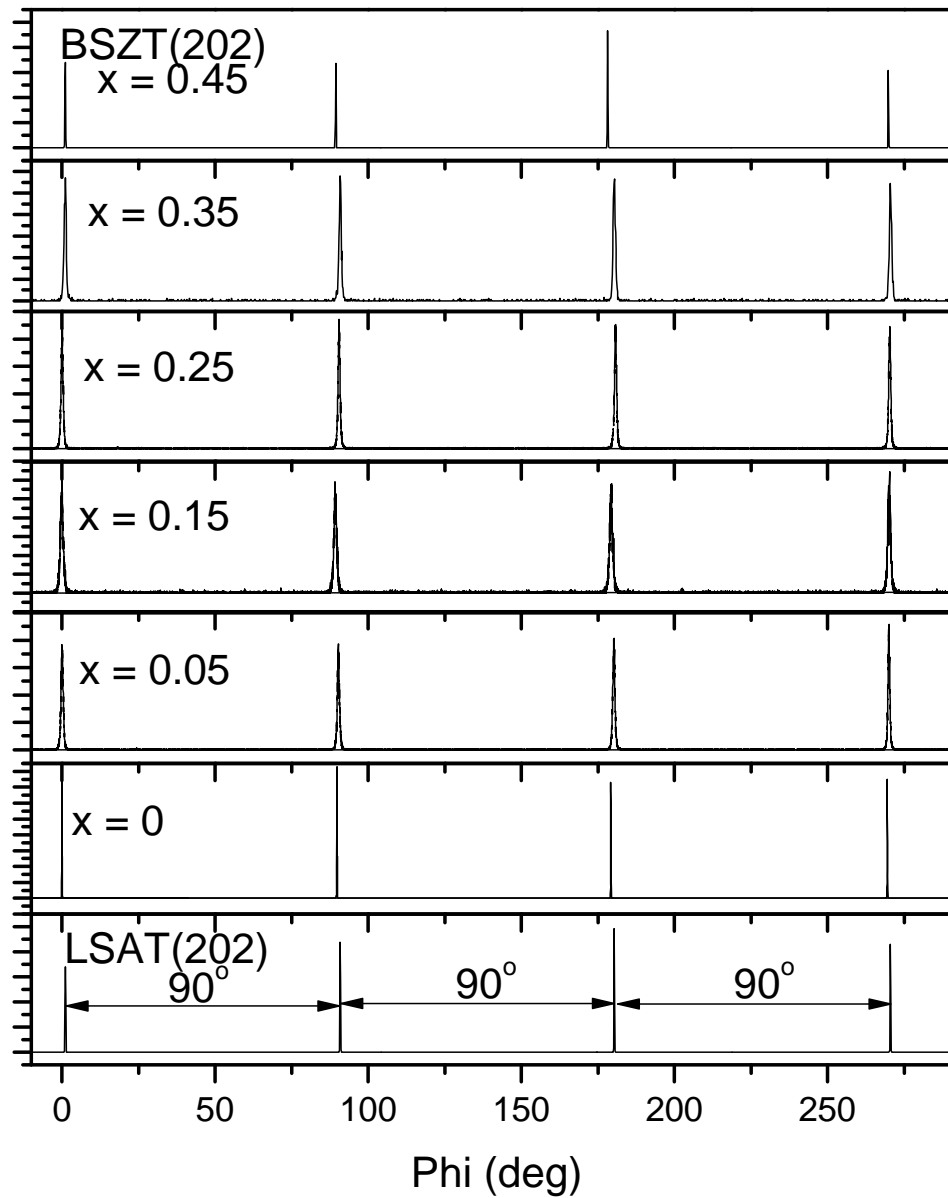


Figure 3.11 Off axis ϕ scan of the (202) diffraction of BSZT thin films deposited LSAT(001) substrates.



3.3.3 Effect of different substrates

Ferroelectric thin films have been deposited on different substrates such as MgO (Chen et al. 2001; Moon et al. 2005), LAO (Majumder et al. 2001), STO (Vendik et al. 1999) and LSAT (Zhou et al. 2007) for microwave applications. The dielectric, electrical and microwave properties were influenced strongly by the substrates. The deviations area caused by the strain generated as a result of the difference between the lattice parameters. In this Section, the crystal structure of $(\text{Ba}_{0.55}\text{Sr}_{0.45})(\text{Zr}_{0.1}\text{Ti}_{0.9})\text{O}_3$ thin film were deposited on MgO (001), LAO (001) and LSAT (001) substrates under the conditions as shown in Table 3.1. (Figure 3.12 to 3.17)

All the films were found to have a pure perovskite phase with (001) orientation as shown in Figure 3.12, 3.14 and 3.16. The in plane alignment of the (100) crystal axis of the single crystal substrate was also confirmed by the XRD off-axis φ scans of the (202) diffraction of the $(\text{Ba}_{0.55}\text{Sr}_{0.45})(\text{Zr}_{0.1}\text{Ti}_{0.9})\text{O}_3$ (BSZT45) film and the substrate as shown in Figure 3.13, 3.15 and 3.17, indicating epitaxial growth of $(\text{Ba}_{0.55}\text{Sr}_{0.45})(\text{Zr}_{0.1}\text{Ti}_{0.9})\text{O}_3$ thin films.

The lattice parameters of $(\text{Ba}_{0.55}\text{Sr}_{0.45})(\text{Zr}_{0.1}\text{Ti}_{0.9})\text{O}_3$ films were determined from the XRD θ - 2θ scan pattern and are listed in Table 3.3. The out-of-plane lattice parameters of the films are slightly larger than those of the bulk ceramics, which indicates that the films have more oxygen vacancies than the bulk ceramics.

If we assume that the tetragonal structure of the films arises from the distortion from the cubic structure of the bulk ceramic, then the in-plane strain ϵ'' is:



THE HONG KONG POLYTECHNIC UNIVERSITY

$$x'' = \frac{a_f - a_0}{a_0} \quad (3.7)$$

where a'' is the in-plane lattice parameter of $(\text{Ba}_{0.55}, \text{Sr}_{0.45})(\text{Zr}_{0.1}, \text{Ti}_{0.9})\text{O}_3$ film and a_0 is the lattice parameter of bulk ceramics. On the other hand, the ideal in-plane strain induced by lattice mismatch is given by:

$$x^0 = \frac{a_s - a_0}{a_0} \quad (3.8)$$

where a_s is the lattice parameter of the substrate (also see Table 3.3)

Table 3.3 shows that the ideal in-plane strain x^0 of film grown on LAO, LSAT and substrates have negative values, indicating that the films are under in-plane compression. While for thin films on MgO substrate, the in-plane strain x^0 of film have positive value, indicating that the films having in plane elongation. From the XRD patterns, the lattice parameters of the $(\text{Ba}_{0.55}, \text{Sr}_{0.45})(\text{Zr}_{0.1}, \text{Ti}_{0.9})\text{O}_3$ film on different substrates can be calculated, i.e. x'' can also be calculated. From Table 3.3, the x'' have positive values, indicates that the films are under in-plane elongation.

As the film thickness has greatly exceeded the critical value, the internal stress may be relaxed towards a zero-strain state by the formation of misfit dislocations. The large lattice mismatch energy induced by the lattice mismatch at the interface can be released by creating a number of edge dislocations at the interface between the film and the substrate. It is noted that the strain induced by thermal expansion difference is one order of magnitude smaller than that induced by lattice mismatch, implying that the thermal expansion mismatch could not be the dominant factor in this case.

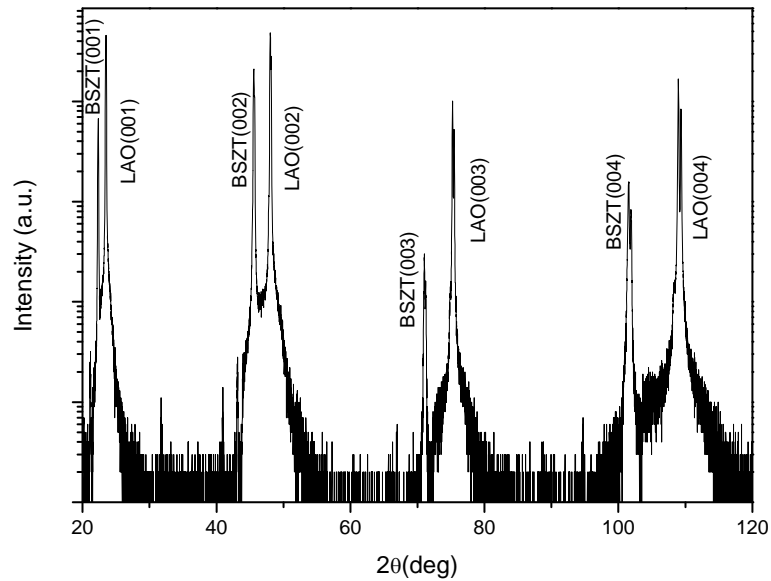


Figure 3.12 XRD θ - 2θ scan pattern of $(\text{Ba}_{0.55},\text{Sr}_{0.45})(\text{Zr}_{0.1},\text{Ti}_{0.9})\text{O}_3$ grown on LAO(001) substrate.

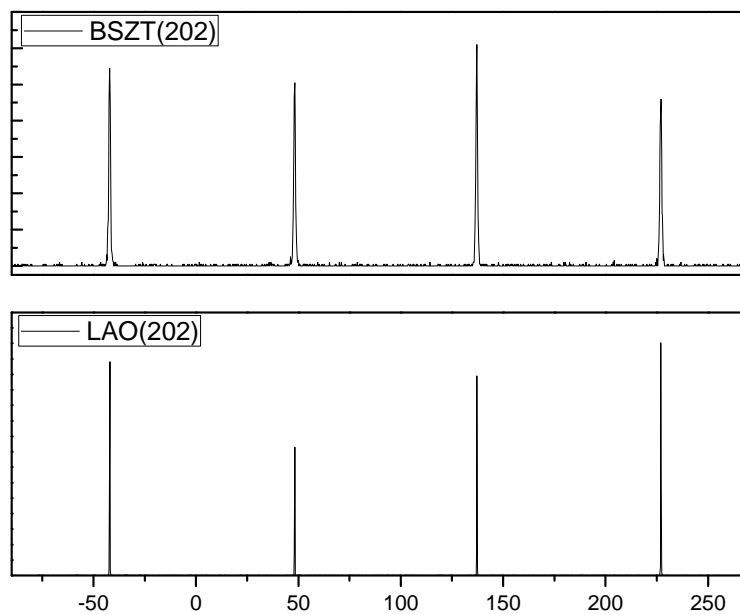


Figure 3.13 Off axis ϕ scan of the (202) diffraction of $(\text{Ba}_{0.55},\text{Sr}_{0.45})(\text{Zr}_{0.1},\text{Ti}_{0.9})\text{O}_3$ thin films deposited on LAO(001) substrate.

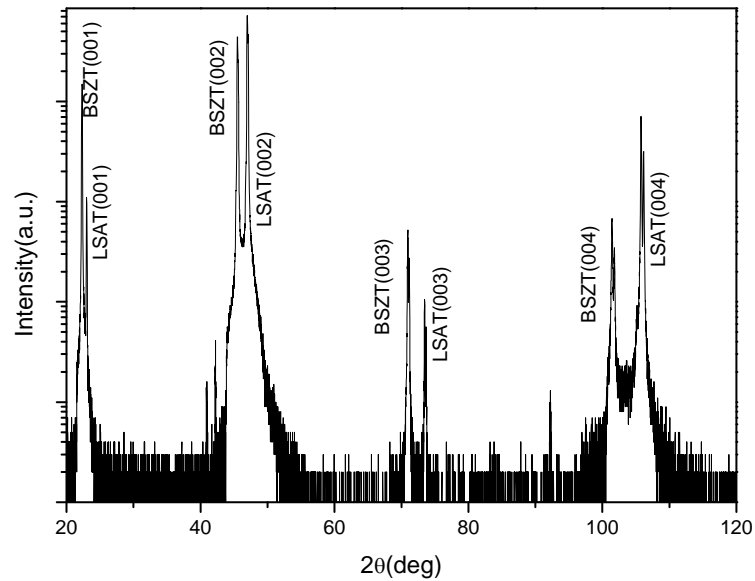


Figure 3.14 XRD θ - 2θ scan pattern of $(\text{Ba}_{0.55},\text{Sr}_{0.45})(\text{Zr}_{0.1},\text{Ti}_{0.9})\text{O}_3$ grown on LSAT(001) substrate.

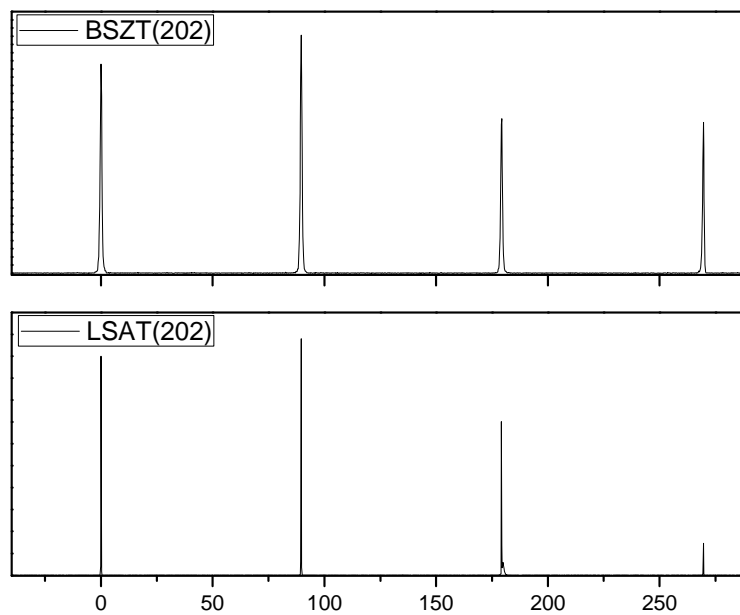


Figure 3.15 Off axis ϕ scan of the (202) diffraction of $(\text{Ba}_{0.55},\text{Sr}_{0.45})(\text{Zr}_{0.1},\text{Ti}_{0.9})\text{O}_3$ thin films deposited on LSAT(001) substrate.

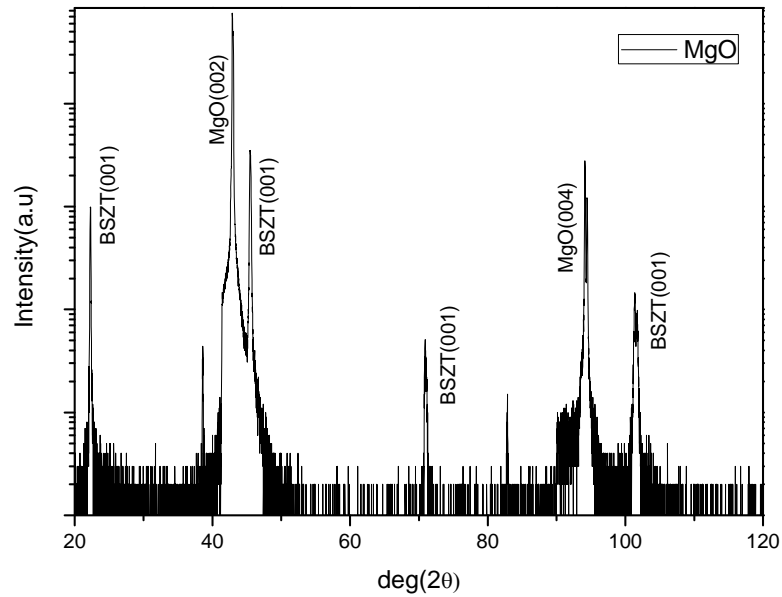


Figure 3.16 XRD θ - 2θ scan pattern of $(\text{Ba}_{0.55},\text{Sr}_{0.45})(\text{Zr}_{0.1},\text{Ti}_{0.9})\text{O}_3$ grown on MgO(001) substrate.

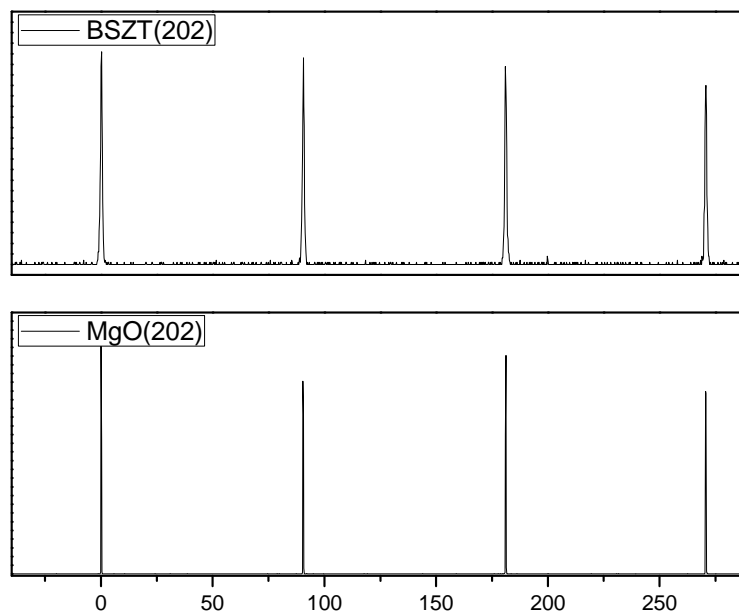


Figure 3.17 Off axis ϕ scan of the (202) diffraction of $(\text{Ba}_{0.55},\text{Sr}_{0.45})(\text{Zr}_{0.1},\text{Ti}_{0.9})\text{O}_3$ thin films deposited on MgO(001) substrate.

Table 3.3 Lattice parameters of thin films, un-relaxed lattice misfit and actual in-plane lattice misfit strain on various substrates at room temperature.

Substrate	Crystal structure	Lattice parameter(Å)			FWHM of rocking curve of BSZT(001) peak(deg)	x^0 (%)	$x^{2\theta}$ (%)
		Substrate	Out-of-plane c	In-plane a			
MgO(001)	Cubic	4.215	3.9753	3.9826	0.67	5.8363	0.15873
LAO(001)	Rhombohedral	3.790	3.9789	3.9801	0.09	-5	0.27967
LSAT(001)	Cubic	3.868	3.9729	3.9819	0.07	-2.6112	0.00982
BSZT45 bulk ceramics	Cubic		3.969		N.A.	N.A.	N.A.

3.4 Investigation of surface morphology by atomic force microscopy

3.4.1 Atomic force microscopy

Scanning Probe Microscopy (SPM):

The SPM is one kind of microscopy that forms images of surfaces using a physical probe that scan over the specimen. The images of the surface were obtained from the interaction between the probe and the surface. The probe is moving mechanically in a raster scan across the specimen, line by line. The interaction of probe and surfaces is recorded as a function of position.

Atomic Force Microscopy (AFM):

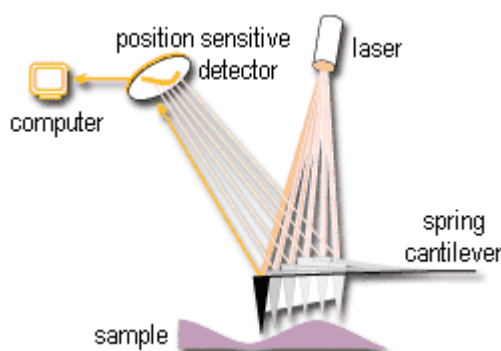


Figure 3.18 Experimental setup of AFM (wikipedia).

The AFM (Morris et al. 1999) works by scanning a fine ceramic or semiconductor tip over a surface much the same way as a phonograph needle scanning a record. The tip is positioned at the end of a cantilever beam shaped much like a diving board. As the tip is repelled by or attracted to the surface, the cantilever beam deflects. The magnitude of the deflection is captured by a laser that reflects at an oblique angle from the very end of the cantilever. A plot of the laser deflection versus tip position on the sample surface provides the resolution of the hills and valleys that constitute the topography of the



THE HONG KONG POLYTECHNIC UNIVERSITY

surface. The AFM can work with the tip touching the sample (contact mode), or the tip can tap across the surface (tapping mode), or non-contact mode.

The following shows the differences of contact mode, non-contact mode and tapping mode.

Contact mode: Probe scanning across a sample surface, monitor the change in cantilever deflection with the split photodiode detector. A feedback loop maintains a constant cantilever deflection (constant force) by vertically moving the scanner to maintain a constant photodetector signal. This feedback loop maintains a constant force during imaging, ranging between 0.1-100mN. The distance the scanner moves vertically at each x or y direction. The data point is stored by the computer to form the topographic image of the sample surface.

Non-contact mode: The tip on the sample surface with 5-20nm distance without contact with the sample. It can eliminate tip contamination problem due to the contact of tip with sample surface. The force between sample and tip is weak long distance for van der Waals attraction force. A small oscillation is applied on the tip, so that AC measurement can be used to determine the weak interaction. But the resolution is poor. This movement forms the photographic image.

Tapping mode: Larger oscillation in the cantilever occurs at its resonant frequency (~100kHz) and lightly trapping on the surface during scanning (discontinuous contact with sample surface). The deflection of laser is used to detect root mean square amplitude of cantilever oscillation. A feedback loop maintains constant oscillation amplitude by moving the scanner vertically at every point.



In this Section, the surface morphology, surface roughness and grain size of the BSZT thin film were studied using a Digital Instruments Nanoscope II atomic force microscope (AFM) operating in the tapping mode. All images were fitted using the flattening and plane fit functions provided with the AFM software. The root mean square (rms) roughness of the film surface and the grain size were determined also by using the software included in the instrument.

3.4.2 Compositional dependence

In the BSZT thin films, the surface morphology of the films may be influenced by the compositional dependence of the strontium content x . In Chapter 2, we have found that the addition of Sr into the ceramics influence the grain size strongly. The surface morphology of the thin film was studied by AFM. Figure 3.19 shows the surface morphology of the thin films. Through the analysis of these AFM images, we found that the surface morphological features of the thin film were sensitive to the amount of Sr contents. The grain size of the thin films decreases with the increase in Sr content. On the other hand, a smooth surface with no microcracks and pinholes, and a dense morphology were observed in all the investigated BSZT thin film compositions.

Table 3.4 lists average grain size of the BSZT thin films evaluated from the AFM results.

Table 3.4 Average grain size of the $(\text{Ba}_{1-x}, \text{Sr}_x)(\text{Zr}_{0.1}, \text{Ti}_{0.9})\text{O}_3$ thin film grown on LSAT substrates.

Composition	$x = 0$	$x = 0.25$	$x = 0.45$
Average grain size(nm)	110-130	60-80	20-40

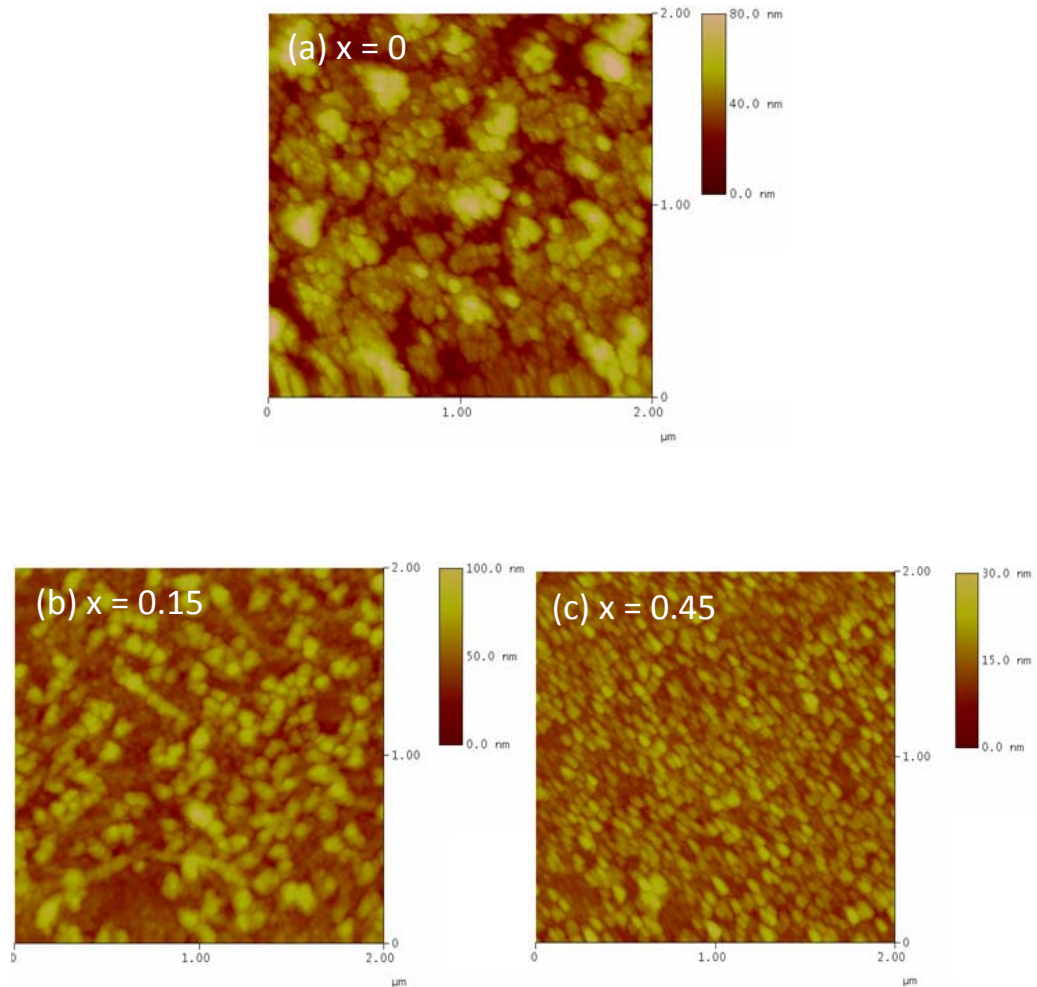


Figure 3.19 Surface morphology of BSZT thin film deposited on LSAT (001) single crystal substrate. (a) $x = 0$, (b) $x = 0.15$, (c) $x = 0.45$.

3.4.3 Effect of different substrates

From the AFM study performed on the different samples, we can see that the surface morphology is similar for all the films with the existence of a granular like surface with rounded grains. The similarity in the growth morphology on different substrates, showing an island like growth mode, is surprising. This means that during the ablation process, the BSZT accommodates the strains, leading to strong distortion of

the perovskite cell.

As a result, the films of oxide will grow in the same way since its cell is highly distorted. However, some differences exist in the mean grains diameter, the mean surface roughness (rms), and the maximum peak to valley roughness values depending on the choice of substrate. On LSAT and LAO, the rms values are about the same (40\AA), but lower than those obtained from MgO (rms: 100\AA). Concerning the mean grains diameter values, we found that they are in the same order. Indeed, the mean grains diameter of films grown on MgO is larger than in others. This is probably due to the large lattice mismatch between the BSZT films and the MgO substrates. The strain energy will generate a strain induced roughening on the surface by the dynamically stable growth mode.

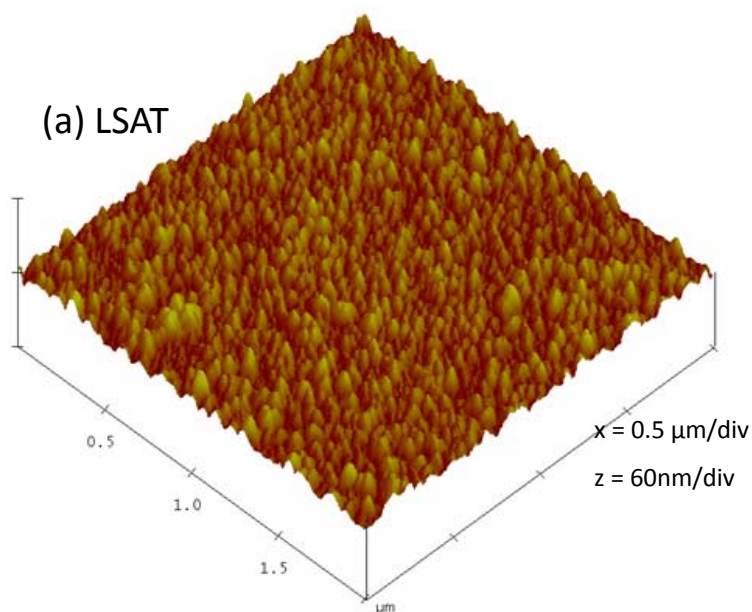


Figure 3.20 Surface morphology of $(\text{Ba}_{0.55},\text{Sr}_{0.45})(\text{Zr}_{0.1},\text{Ti}_{0.9})\text{O}_3$ thin film deposited on LSAT substrate.

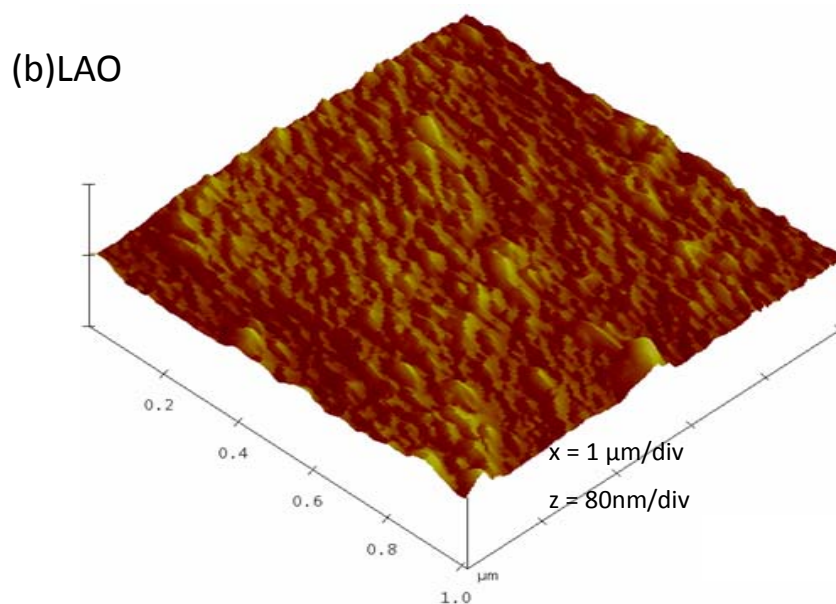


Figure 3.21 Surface morphology of $(\text{Ba}_{0.55},\text{Sr}_{0.45})(\text{Zr}_{0.1},\text{Ti}_{0.9})\text{O}_3$ thin film deposited on LAO substrate.

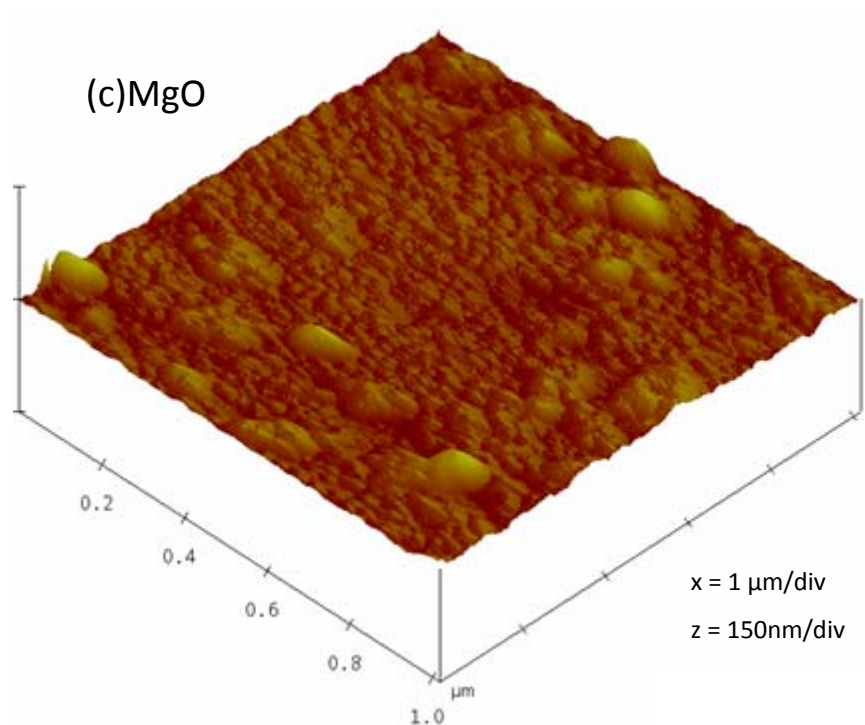


Figure 3.22 Surface morphology of $(\text{Ba}_{0.55},\text{Sr}_{0.45})(\text{Zr}_{0.1},\text{Ti}_{0.9})\text{O}_3$ thin film deposited on MgO substrate.



Table 3.5 Average grain size and roughness of the $(\text{Ba}_{0.55}\text{Sr}_{0.45})(\text{Zr}_{0.1}\text{Ti}_{0.9})\text{O}_3$ thin film grown on different substrates.

Substrate	LSAT	LAO	MgO
Average grain size(nm)	20-40	20-40	20-40
Roughness	3.2	3.3	9.4

3.5 Summary

Epitaxial BSZT thin films were produced by using pulsed laser deposition. The microstructure of the thin film were analyzed by the X – ray diffraction. It is found that, the lattice parameter decreases with the increase in Sr content. The surface morphology of the films was observed using an atomic force microscope. The grain size of the thin film decreases with the increase in Sr content. $(\text{Ba}_{0.55}\text{Sr}_{0.45})(\text{Zr}_{0.1}\text{Ti}_{0.9})\text{O}_3$ films were also deposited on LSAT, LAO and MgO substrates. By considering the crystalline quality, epitaxy of the films and the surface roughness and grain size, the optimum conditions for depositing BSZT thin films were found.



CHAPTER 4

BARIUM STRONTIUM ZIRCONATE TITANATE

THIN FILM CHARACTERIZATION

4.1 Introduction

In Chapter 2, we found that for BSZT ceramics the dielectric, ferroelectric and structural properties are greatly depended on the Sr contents. At the Curie temperature, the system transform from ferroelectric state to paraelectric state, at which the structural changes from tetragonal to cubic. For tunable microwave application, it is preferable to use system in the paraelectric state as there is absent of hysteresis, and the tunability of the sample could be larger than 50% for typically applications. To determine the potential applications of the BSZT in thin films form, we have conducted relative permittivity measurement as a function of temperature, voltage and hysteresis measurements.

Generally, in thin films, the dielectric and ferroelectric behaviours are much more complicated in comparison with bulk ceramics because of the size effect. Many reasons for the size effect have been proposed, including local polar regions near the charged defects like oxygen vacancies, a dead layer near the interface and residual stress from the lattice mismatch or the different thermal expansion coefficients between the substrate and the film.

Interdigital capacitor (IDC) is a useful component in integrated microwave circuit because of its simplicity of fabrication, low capacitance values and ease of integration



THE HONG KONG POLYTECHNIC UNIVERSITY

into microwave devices. In this Chapter, properties of the thin film are characterized by IDC with Gevorgian model.

4.2 Electrode patterning of the BSZT thin films

4.2.1 Electrode deposition, photolithography, IDC geometry and extraction of relative permittivity of the film

Before deposition of gold as electrode, the thicknesses of the thin films are measured using a Metricon Model 2010 prism coupler. The thickness of the $(\text{Ba}_{1-x}\text{Sr}_x)(\text{Zr}_{0.1}\text{Ti}_{0.9})\text{O}_3$ ($x = 0, 0.05, 0.15, 0.25, 0.35, 0.45$) thin films are measured to be around 400 nm.

4.2.1.1 Electrode deposition

The material used in magnetron sputtering has almost no restriction. The target can be either conducting or non – conducting. However, to sputter different materials, the source has to be chosen carefully. The DC sputtering works very well if the target shows some electrical conductivity. For insulating targets, a high frequency plasma discharge must be applied in order to avoid the accumulation of electric charges. Figure 4.1 shows the schematics of the magnetron sputtering setup.

The DC magnetron sputtering system was used to deposit the Au film on the samples. Before deposition, the samples were cleaned by the use of acetone, IPA and deionised water in the ultrasonic bath.

Table 4.1 shows the parameters used for Au sputtering.

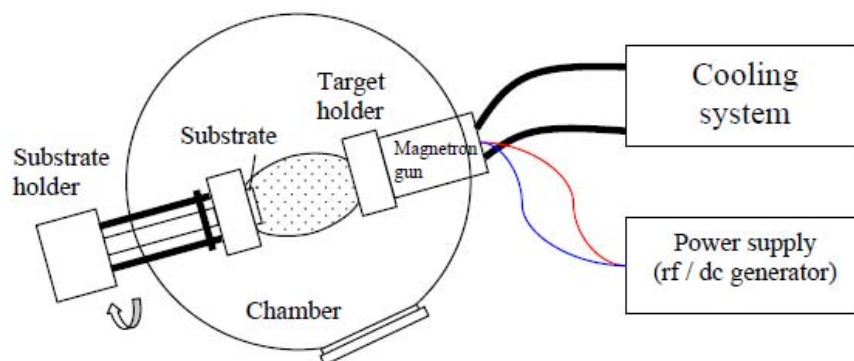


Figure 4.1 Schematic diagram of magnetron sputtering setup. In this system, the power supply can be either RF or DC. The cooling system is to prevent the target from overheating.

Table 4.1 Deposition conditions for Au sputtering.

Target material	Gold (Au)
Sputtering power:	70W
Ar gas pressure:	1.5Pa
Gas flow rate of Ar:	80sccm
Deposition time:	10min
Thickness of Au (measured by surface profiler)	500nm
Substrate temperature	Room temperature

4.2.1.2 Photolithography

After the deposition of Au electrode, the next step is photolithography. Photolithography is the basic technique used to define the shape of micro machined structure. The techniques are essentially the same as that used in the microelectronics industry. For a photolithographic process, many steps are involved. The following



THE HONG KONG POLYTECHNIC UNIVERSITY

section discusses the step involved in fabricating the micropatterns. Figure 4.2 shows the flow for the photolithographic technique.

(i) Photomasks

A photomask with chromium pattern on glass was fabricated by Microelectronic Fabrication Facility in HKUST. The smallest size of the mask pattern was $2\mu\text{m}$. For even higher resolution, the single crystal Quartz can be used as a mask.

(ii) Positive and negative photoresists

Photoresist is a kind of polymer which is sensitive to ultraviolet light. The photoresist can be classified into two groups, termed positive resists and negative resists. Once the ultraviolet light strikes on a positive photoresist, the bonds between the polymers get weakened and become soluble to the photoresist developer. Conversely, if the ultraviolet light strikes on a negative photoresist, the bonds between the polymers get strengthened and become insoluble to the photoresist developer. The photoresist was spin coated on the thin films

(iii) Baking of the photoresist

After the spin coating, the photoresist-coated thin film is then "soft-baked" to drive off excess solvent. The baking makes the photoresist sensitive to UV light. Because of the solvent is mostly removed, the thickness of the photoresist usually decreases almost 25%.

(iv) Exposure of UV light by the use of optical aligner

An optical aligner was used to align the mask and the sample. It also provides the UV light source for exposure. There are many types of exposure methods, for example, for the mask aligner (OAI MDL 800 Series, the one inside PolyU class 1000 cleanroom), there are two types of exposure method, namely, hard contact mode and proximity mode.

**Hard contact mode:**

The photoresist on the substrates is brought in contact with the photomask. For this mode of exposure, very high resolution of the pattern can be made. However, for hard contact mode, it may be easy to damage the mask and causes defect in the pattern.

Proximity mode:

For proximity mode, there is a small gap between the photomask and the substrates, which is typically around 10 to 25 microns. Because there is a little gap in between the sample and the mask, the UV light diffract accordingly, the resolution of the produced pattern is not as high compared with the hard contact mode.

To fabricate IDC with 2 μ m resolution, hard contact mode was used in our experiment to make sure the contact between the thin film surface and the photomask is good enough.

(v) Development and etching

Positive photoresist, the most common type, becomes soluble in the basic developer when exposed, negative photoresist becomes insoluble in the (organic) developer. This chemical change allows some of the photoresist to be removed by a special solution, called "developer" by analogy with photographic developer. In our experiment, positive photoresist AZ5214 and AZ400K developer with deionized water ratio 1:4 were used.

After the development process, the pattern is formed; the solution for etching the gold is a combination of the chemicals of KI, I₂ and H₂O. The samples were put into the etchant for gold etching.

(vi) Cleaning of the residual photoresist by O₂ plasma.

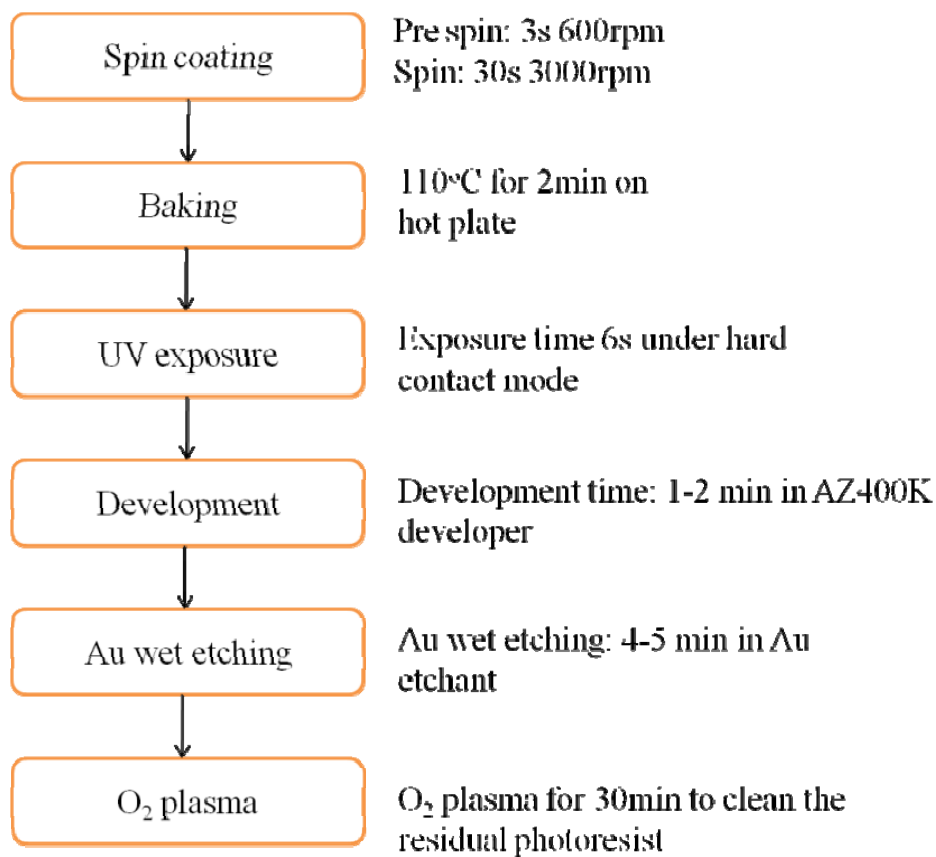


Figure 4.2 Process flow of the photolithographic technique.

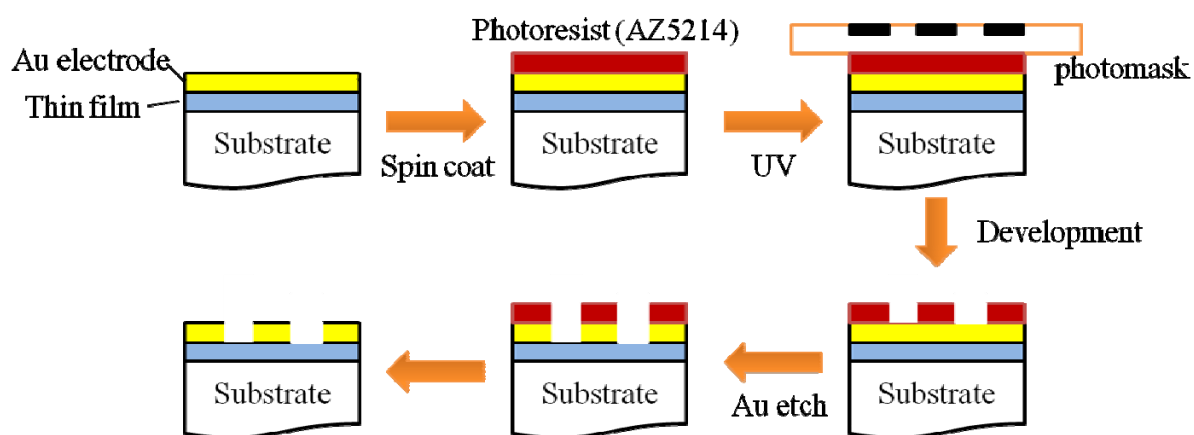


Figure 4.3 Steps for fabricating pattern by photolithography.

4.2.1.3 IDC geometry

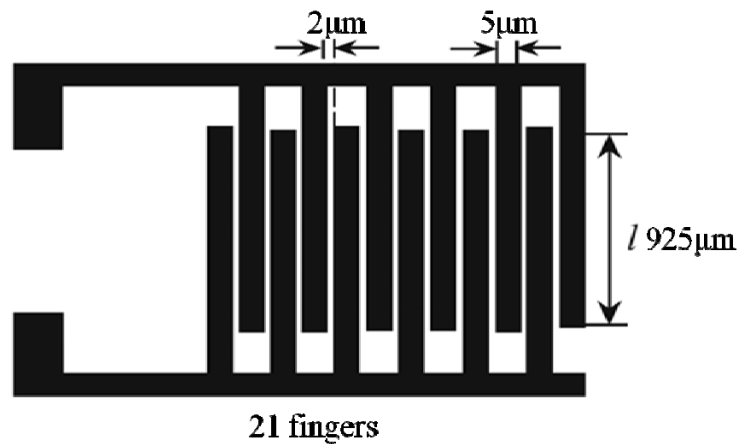


Figure 4.4 Schematic diagram showing the interdigital capacitor (IDC) used for dielectric and hysteresis measurement.

As shown in Figure 4.4. The electrode pattern used for dielectric and ferroelectric characterization consists of interdigital electrodes (IDC). The IDE had a total of 21 fingers with finger length of $925\mu\text{m}$, and finger width of $5\mu\text{m}$. The finger gap spacing with is $2\mu\text{m}$. The fingers of the IDC are arranged to lie along the in-plane $\langle 010 \rangle$ or $\langle 100 \rangle$ crystallographic directions. The IDC was wire bonded to a piece of PCB for easy handling and better electrical contact during subsequent measurement process.

4.2.1.4 Capacitor configurations: parallel plate vs coplanar

Typically there are two choices for capacitor configurations used for microwave devices as shown in Figure 4.5, a parallel plate capacitor, where the dielectric is sandwiched between two metal electrodes, and a coplanar capacitor, where the electrode lies on the surface of the dielectric.

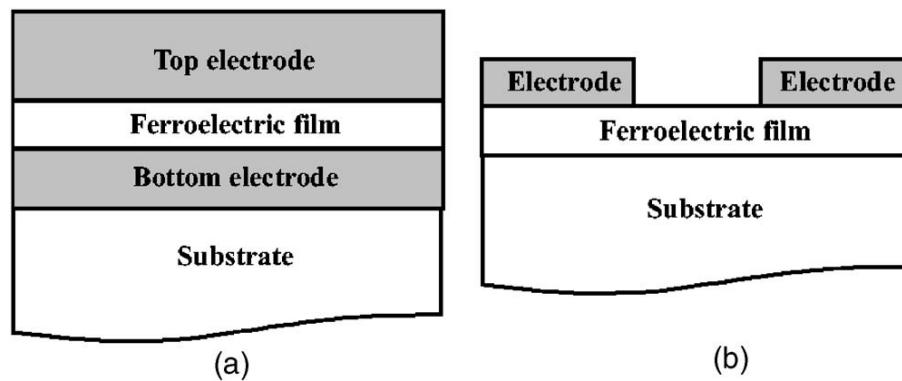


Figure 4.5 (a) Parallel plate capacitor, and (b) coplanar capacitor.

Both configurations have been used for microwave devices. Coplanar capacitors are preferred for obtaining sub-picofarad capacitance values, as only a portion of the electric field probes the dielectric and substrate. The capacitance values of the parallel capacitor are much higher than the coplanar one. For coplanar configuration, the tunability is much lower compared to parallel capacitors since the capacitance from the air and substrates are not tunable.

In terms of fabrication, coplanar capacitors typically require a single photolithography step. As for the disadvantage, in addition to low tunability, coplanar capacitors require higher handling voltages. Parallel configuration capacitors typically exhibit higher tunability at lower applied voltages. Extraction of the electrical characterization result using IDC is much more complicated. The interdigital varactor lends itself to single layer processing and high Q values.

The calculation of the relative permittivity from the IDC data was conducted using a MATHEMATICA program we developed based on Gevorgian's model, which gives the relationship among the capacitance, the electrode sizes and the material properties (Gevorgian et al. 1996),(Wang et al. 2003) The reported dielectric constant was



THE HONG KONG POLYTECHNIC UNIVERSITY

extracted from the capacitance using conformal mapping technique originally developed by Gevorgian. By considering the capacitance between the fingers and the capacitance due to the finger ends, the relative permittivity of the thin film can be calculated by a set of mathematical formulas.

4.3 Measurement of relative permittivity of BSZT thin films

4.3.1 Permittivity as a function of temperature

The relative permittivity ε of the film was measured using an HP4194A impedance analyzer connected to a temperature controller (Oxford) (-190°C to 150°C). The impedance analyzer can be used in the frequency range of 1kHz – 1MHz with special fixture connected.

4.3.1.1 Effect of compositions

The phase transition temperature in the $(\text{Ba}_{1-x}\text{Sr}_x)(\text{Zr}_{0.1}\text{Ti}_{0.9})\text{O}_3$ ($x = 0, 0.05, 0.15, 0.25, 0.35, 0.45$) thin films have been investigated. Figure 4.6 shows the temperature dependence of the relative permittivity of the BSZT thin films measured using IDC in the frequency range of 1kHz to 100kHz. As shown in Figure 4.6, the Curie temperature decreases with the increase in the Sr content. While, compared with the Curie temperature measured in bulk form, the Curie temperature is higher than the bulk ceramics. It is noted that, the Curie temperature of the $\text{Ba}(\text{Zr}_{0.1}\text{Ti}_{0.9})\text{O}_3$ and $(\text{Ba}_{0.95}\text{Sr}_{0.05})(\text{Zr}_{0.1}\text{Ti}_{0.9})\text{O}_3$ thin films is higher than 150°C. However, the transition peaks cannot be measured due to the device limitations. Frequency dispersion mechanism have been observed in the measurements, as the frequency increases, the

phase transition peak is depressed continuously, the relative permittivity decreases, and T_c shifts to higher temperature. It is noted that the shape of the peaks are much broader than the BSZT bulk ceramics. As reported in the literature, the broadening of the transition peaks in the films is attributed to the small grain size. The broadening of the transition peak have also been observed in other ferroelectric thin films such as BaTiO_3 (Udayakumar et al. 1995) and $\text{Pb}(\text{Zr},\text{Ti})\text{O}_3$ (TrolierMcKinstry et al. 1996), which have grain size in the nanometer range.

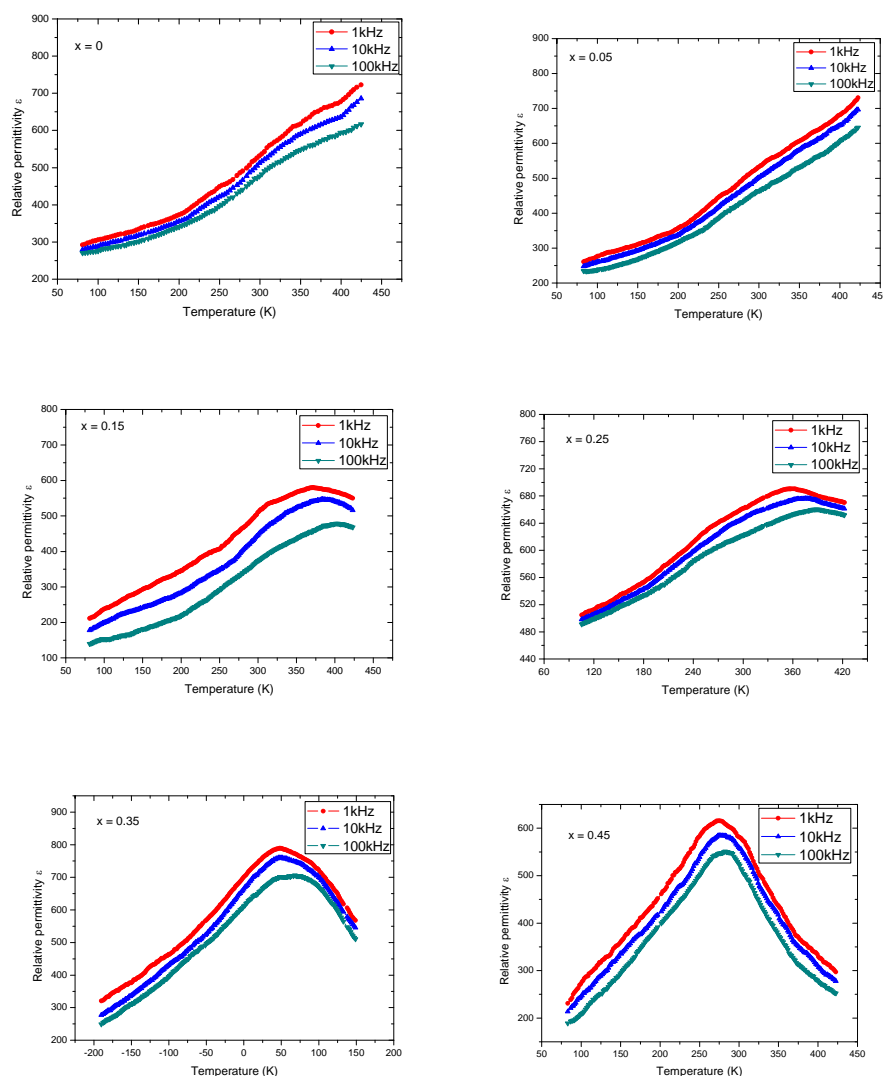


Figure 4.6 Temperature dependence of the relative permittivity of BSZT thin films on LSAT measured using IDC.

For better analysis, Figure 4.7 show the plots of the relative permittivity against temperature for all compositions measured at 1kHz. The Curie temperature of the thin film is much higher than the corresponding bulk ceramics, the upward shift of the Curie temperature is believed to arise from the in-plane tensile strain induced by the lattice misfit on LSAT.

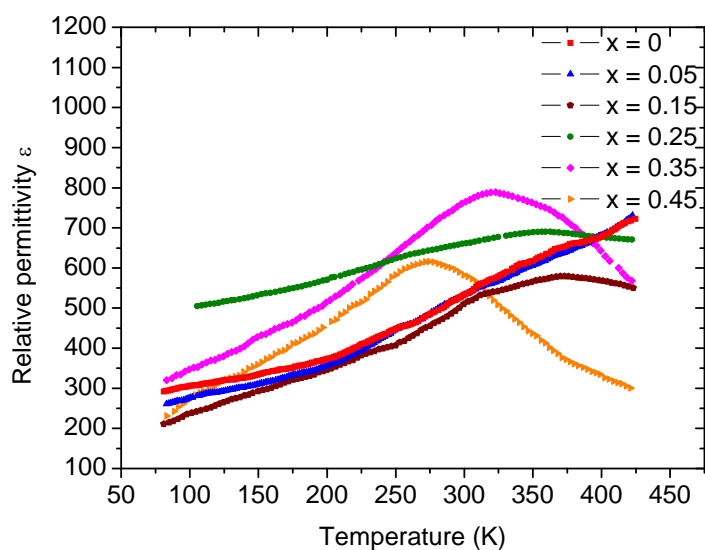


Figure 4.7 Temperature dependence of the relative permittivity of BSZT thin film on LSAT.

Table 4.2 Transition temperature of $(\text{Ba}_{1-x}\text{Sr}_x)(\text{Zr}_{0.1}\text{Ti}_{0.9})\text{O}_3$ ($x = 0, 0.05, 0.15, 0.25, 0.35, 0.45$) thin films and bulk ceramics measured at 1kHz.

	$x=0$	$x=0.05$	$x=0.15$	$x=0.25$	$x=0.35$	$x=0.45$
Bulk ($^{\circ}\text{C}$)	97	88	62	39	8	-6
Thin film($^{\circ}\text{C}$)	---	---	97	80	23	10

The upward shift of T_c of the BSZT thin film is believed to be due to the contribution of in-plane lattice elongation as confirmed by XRD measurements, which is analogous to that reported in the literature (Lin et al. 2005; Wang et al. 2005). In



THE HONG KONG POLYTECHNIC UNIVERSITY

general, if there is a tensile stress along the in-plane direction, then the Curie temperature of the thin films is likely to shift toward the high temperature direction. Conversely, a compressive stress may lower the Curie temperature of the films. It has been reported that a biaxial tensile strain of order of 1% in ferroelectric thin films is enough to push the Curie temperature T_c to a value much higher than its inherent value. (Choi et al. 2004; Haeni et al. 2004)

For example, the $\epsilon - T$ curve for $(\text{Ba}_{0.55}, \text{Sr}_{0.45})(\text{Zr}_{0.1}, \text{Ti}_{0.9})\text{O}_3$ thin films exhibits a maximum at 10°C . The upshift of T_c in our tensile stressed BSZT thin film is not so significant as expected because the film thickness has greatly exceeded its critical values, resulting in a relaxation towards a zero-strain state by introduction of dislocations. The large lattice misfit energy at the interface can only be released by creating lots of edge dislocations at the interface between the BSZT film and the substrate. (Canedy et al. 2000; Chen et al. 2002)

In thin film form the relative permittivity of the BSZT is low as compared to its bulk. Decrease in the dielectric constant can be attributed to reduction of crystallite size due to incorporation of Sr in the BZT lattice. The lower permittivity value results from lack of long range ordering in the material, which is effectively caused by the smaller crystallite size.

4.3.1.2 Effect of substrates

The BSZT thin films exhibit different dielectric behaviour when grown on different substrates. The physical properties of the thin film can be altered by the



THE HONG KONG POLYTECHNIC UNIVERSITY

substrates. Strain can be induced by the lattice mismatch or difference in thermal expansion coefficient between the film and the substrate. As a result, the properties of the thin films can be markedly different to the intrinsic properties of the corresponding unstrained bulk materials.

Although such strain sometimes leads to degraded film properties, if judicious use is made of substrates and growth parameters, strain offers the opportunity to enhance particular properties of a chosen material in thin film form and, this is called ‘ lattice or strain engineering’.

Strain engineering is a very hot topic in state of the art thin film studies, since strain is an effective way to adjust the Curie temperature of ferroelectric thin film. In this Section, the temperature dependence of relative permittivity of $(\text{Ba}_{0.55}, \text{Sr}_{0.45})(\text{Zr}_{0.1}, \text{Ti}_{0.9})\text{O}_3$ BSZT45 thin films deposited LAO(001), LSAT(001) and MgO(001) substrates are presented.

Figure 4.8 shows the temperature dependence of the relative permittivity of BSZT45 thin film deposited on different substrates under the optimum conditions. The film grown on LAO ($T_c \sim 26^\circ\text{C}$), LSAT ($T_c \sim 10^\circ\text{C}$) and MgO ($T_c \sim 20^\circ\text{C}$) shows increased phase transition temperature compared with the bulk BSZT45 ceramics ($T_c \sim -6^\circ\text{C}$). The shift of the T_c is believed to be due to the elongation of the in-plane lattice parameters. The shift of T_c for BSZT45 thin film in LAO and MgO are more significant compared with LSAT. Which is probably due to the in-plane strain for BSZT45 thin film on MgO and LAO are much higher than that on LSAT.

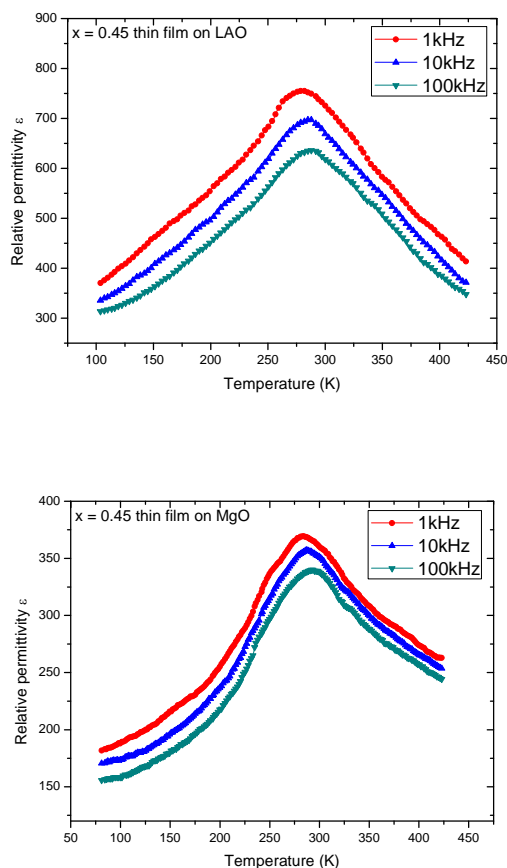


Figure 4.8 Relative permittivity as a function of temperature of

$(\text{Ba}_{0.55}, \text{Sr}_{0.45})(\text{Zr}_{0.1}, \text{Ti}_{0.9})\text{O}_3$ thin films deposited at 700°C on LAO and MgO substrates.

4.3.2 Permittivity as a function of frequency

The room-temperature relative permittivity of the BSZT thin films as a function of frequency was measured using an HP4294A impedance analyzer (measured frequency: 1kHz – 1MHz) and an HP4291B RF impedance analyzer (measured frequency: 1MHz – 100MHz). The HP4291B RF impedance analyzer was calibrated before the measurement in order to remove the parasitic of the testing probe and the connecting wire.

4.3.2.1 Effect of compositions

Figure 4.9 shows the relative permittivity ϵ and dissipation factor of BSZT films as a function of frequency. The relative permittivity of the films shows slight dispersion.

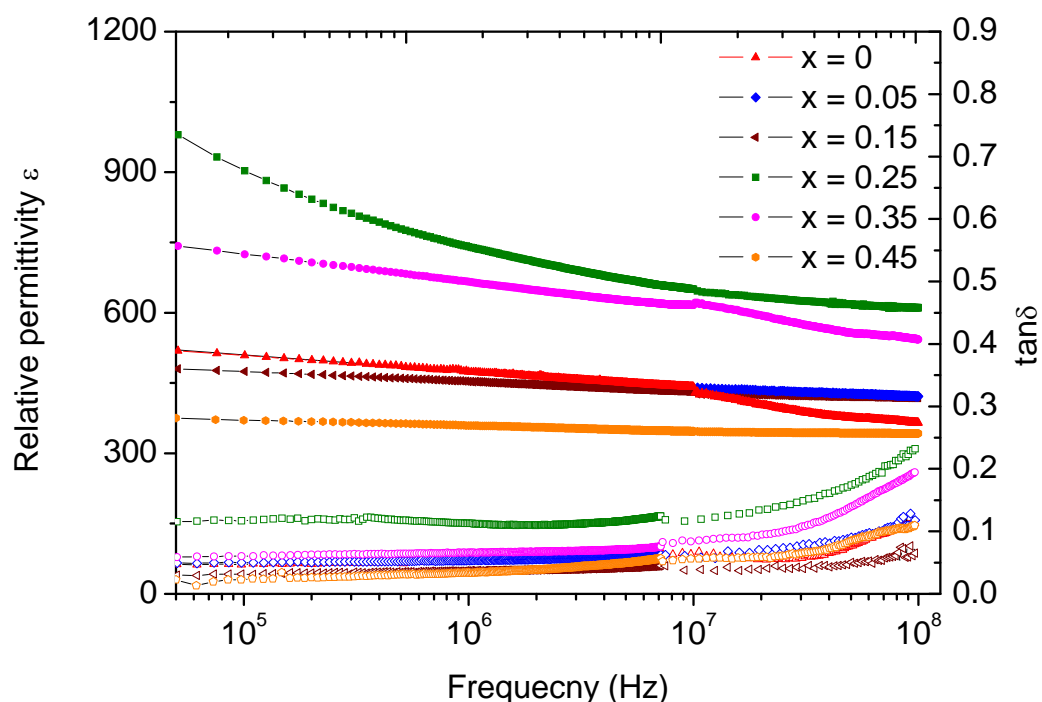


Figure 4.9 Frequency dependence of the relative permittivity ϵ and loss tangent of $(\text{Ba}_{1-x}\text{Sr}_x)(\text{Zr}_{0.1}\text{Ti}_{0.9})\text{O}_3$ ($x = 0, 0.05, 0.15, 0.25, 0.35, 0.45$) thin films.

The slow decrease of the permittivity and the less than linear increase of the loss tangent could indicate a broad distribution of relaxation frequencies instead of a constant series resistance of the electrode.

Ferroelectric theory predicts decreasing loss tangent as measurement are made closer to T_c approaching from the low temperature ferroelectric side of the phase



THE HONG KONG POLYTECHNIC UNIVERSITY

transition. For $(\text{Ba}_{0.75}\text{Sr}_{0.25})(\text{Zr}_{0.1}\text{Ti}_{0.9})\text{O}_3$ thin film, the Curie transition temperature is close to room temperature. The $(\text{Ba}_{0.75}\text{Sr}_{0.25})(\text{Zr}_{0.1}\text{Ti}_{0.9})\text{O}_3$ thin film shows highest relative permittivity and highest loss tangent, which is consistent with the prediction.

However, at higher frequency, the loss tangent rises rapidly. This dispersion is probably due to parasitic capacitance not accounted for the circuit model for in determining the loss of DUT.

The dispersion can be strongly linked to the microstructure of the film. The low frequency dielectric dispersion in ferroelectric films can arise due to domain wall fluctuations, hopping conduction or space charge dispersion. But, as the frequency increases, parameter like wires, ferroelectric domains, and electrodes influenced the dielectric dispersion.

Therefore, for better understanding, we consider an equivalent circuit model of the measurement system. (Nath et al. 2004)

The equivalent circuit model of the measurement system with wire inductance L_s , wire/electrode contact resistance R_s and dielectric resistance of the sample R_p , capacitance C_p . The capacitance C_m and loss tangent $\tan\delta_m$ can be measured. From the measured result, C_m and $\tan\delta_m$ have contribution from the wire inductance L_s , wire/electrode contact resistance R_s between the measuring tools and the samples. From the equivalent circuit, $\tan\delta_m$ and C_m can be written as equation (4.1) and (4.2)

$$\tan\delta_m = \frac{\omega C_p R_s + \tan\delta_d}{(1 - \omega^2 L_s C_p)} \quad (4.1)$$



$$C_m = \frac{C_p}{(1 + \tan^2 \delta_m)(1 - \omega^2 L_s C_p)} \quad (4.2)$$

As the frequency of the measurements increases, $\tan \delta_m$ increases with the wire inductance L_s and resistance R_s , while the measured capacitance decreases. From this mathematical model, the dielectric behaviour of the BSZT thin film can be understood.

4.3.2.2 Effect of substrates

From Figure 4.10, the frequency dependence of the relative permittivity and loss tangent of $(\text{Ba}_{0.55}, \text{Sr}_{0.45})(\text{Zr}_{0.1}, \text{Ti}_{0.9})\text{O}_3$ thin films on different substrates. It can be seen that, there is a very small dispersion in ϵ characteristics for BSZT45 thin film on different substrates. Variations in the relative permittivity have been reported different the crystallinity (Mohammed et al. 1996; Park et al. 2001), grain size (Detalle et al. 2008; Ohki and Miyata 2009) and stress (Hu et al. 2004). The variation of the relative permittivity can be attributed to different grain size and stress in the films.

4.3.3 Dielectric tunability of the BSZT thin films

The electric field dependence of the relative permittivity of the BSZT thin films were also characterized using HP4294A impedance analyzer (measured frequency : 1kHz-1MHz) and HP4291B RF impedance analyzer (measured frequency 1MHz-100MHz). The measurement was performed by applying a small AC signal of 0.5V amplitude. The DC bias voltage was swept from 0V to positive (+40V) to negative (-40V) and back again. The room temperature tunability K (%) and the figure of merit are defined as Eqs (4.3) and (4.4)

$$K = \frac{\varepsilon(0) - \varepsilon(E_{max})}{\varepsilon(0)} \times 100\% \quad (4.3)$$

$$FOM = \text{tunability}(\%) / \text{loss tangent} \quad (4.4)$$

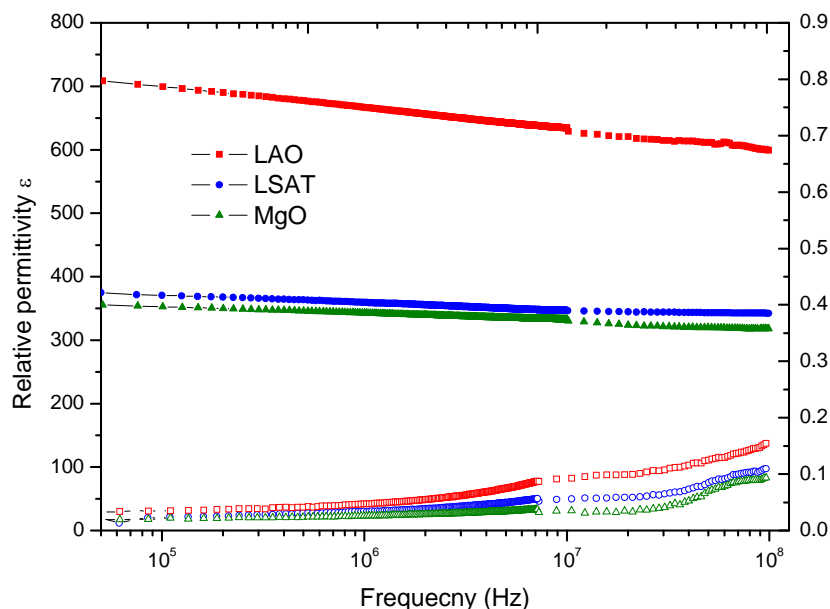


Figure 4.10 Frequency dependence of the in-plane relative permittivity and loss tangent of $(\text{Ba}_{0.55}, \text{Sr}_{0.45})(\text{Zr}_{0.1}, \text{Ti}_{0.9})\text{O}_3$ thin films on different substrates

4.3.3.1 Effect of compositions

Figure 4.11 shows the DC bias electric field dependence of the relative permittivity of the BSZT thin film measured at room temperature. The curves are measured at 10kHz, 100kHz, 1MHz and 100MHz, respectively. The relative permittivity – E-field characteristics of the BSZT thin films were determined over these selected frequencies. A strong dependence of the relative permittivity on the applied DC bias is found. The curves are in the shape of butterfly, which is consistent with the room temperature ferroelectric state observed in the relative permittivity – temperature measurements.



Furthermore, with the increasing in the bias electric field, the dielectric constant and dielectric loss decreases. Such decrease in dielectric loss with increasing electric field is related to the pinning effect of domain or movable charge defects. The characterization of dielectric constant depending on the bias DC voltage provides a useful foreground in tunable devices. A high tunability near the transition temperature is expected. The decrease in tunability with the increase in Sr content indicates the decreasing nonlinearity due to the lower proportion of ferroelectric range.

For a capacitor with a planar structure, the total capacitance is composed of three components: air, BSZT and substrate. In this configuration, tunability only comes from BSZT since the substrate show no observable tunability in such small electric field. Therefore, if we increase the contribution of the BSZT capacitor by depositing a thicker BSZT film, we should be able to increase the tunability value.

It is known that, due to the non-uniform distribution of electrical fields, coplanar designs generally require a higher driving voltage and offer lower apparent tunability in comparison to the parallel plate capacitor. The mechanism of the relationship between relative permittivity and external DC biased field is not clear yet. To obtain a better insight into the problem, it is necessary to use the Johnson's formula (Johnson 1962) to study the behaviour of the ϵ -E curves. Since the ϵ -E dependence to the ferroelectric materials (when in the paraelectric state) is generally found to follow this equation.

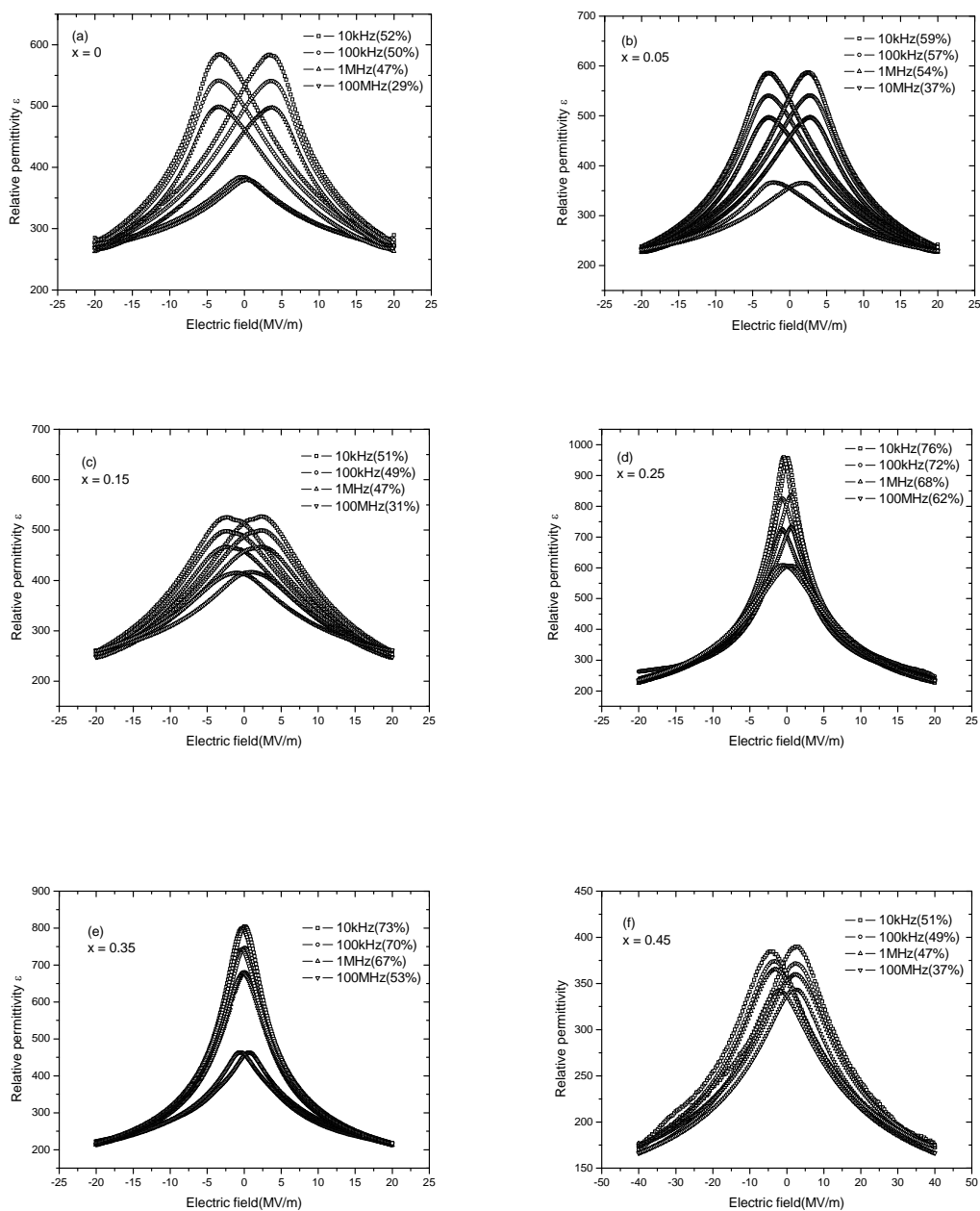


Figure 4.11 Relative permittivity as a function of electric field for

$(\text{Ba}_{1-x}\text{Sr}_x)(\text{Zr}_{0.1}\text{Ti}_{0.9})\text{O}_3$ ($x = 0, 0.05, 0.15, 0.25, 0.35, 0.45$) grown on LSAT.



THE HONG KONG POLYTECHNIC UNIVERSITY

According to the Johnson's formula,

$$\varepsilon_r(T, E) = \frac{\varepsilon_r(T, 0)}{\{1 + [\varepsilon_0 \varepsilon_r(T, 0)]^3 B(T) E^2\}^{\frac{1}{3}}} \quad (4.3)$$

where $\varepsilon_r(T, 0)$ and the ε_0 are the relative permittivity and vacuum permittivity respectively, and $B(T)$ is a phenomenological constant, which provides information on the degree of anharmonic contributions of the polarization to the Helmholtz free energy. However, Eq(4.3) is only suitable for the case in paraelectric state.

For thin film in ferroelectric state, it was found that a polar cluster contribution (Langevin-type polar cluster contribution) term should be taken into account. Thus, the DC bias dependence of relative permittivity should be described with a modified Devonshire relation including a term of local polar clusters or regions (Yang et al. 2007), the so called multipolarization mechanism model proposed by Chen et al. (Ang et al. 2000),

$$\varepsilon_r(T, E) = \frac{\varepsilon_r(T, 0)}{\{1 + [\varepsilon_0 \varepsilon_r(T, 0)]^3 B(T) E^2\}^{\frac{1}{3}}} + \left(\frac{P_r \chi}{\varepsilon_0}\right) [\cosh(E\chi)]^{-2} \quad (4.4)$$

Where $\chi = \frac{P_r L^3}{2k_B T}$ with the cluster polarization P_r and size L .

Figure 4.12 shows the frequency dependence of the dielectric tunability K of $(\text{Ba}_{1-x}\text{Sr}_x)(\text{Zr}_{0.1}\text{Ti}_{0.9})\text{O}_3$ ($x = 0, 0.05, 0.15, 0.25, 0.35, 0.45$) thin films under 20MV/m biased field. The largest tunability is obtained for $x = 0.25$ and $x = 0.35$. The relative permittivity of $x = 0.25$ and $x = 0.35$ is the largest compared with other thin films, from the calculation in Chapter 1, it concludes that the tunability increases with the relative permittivity.

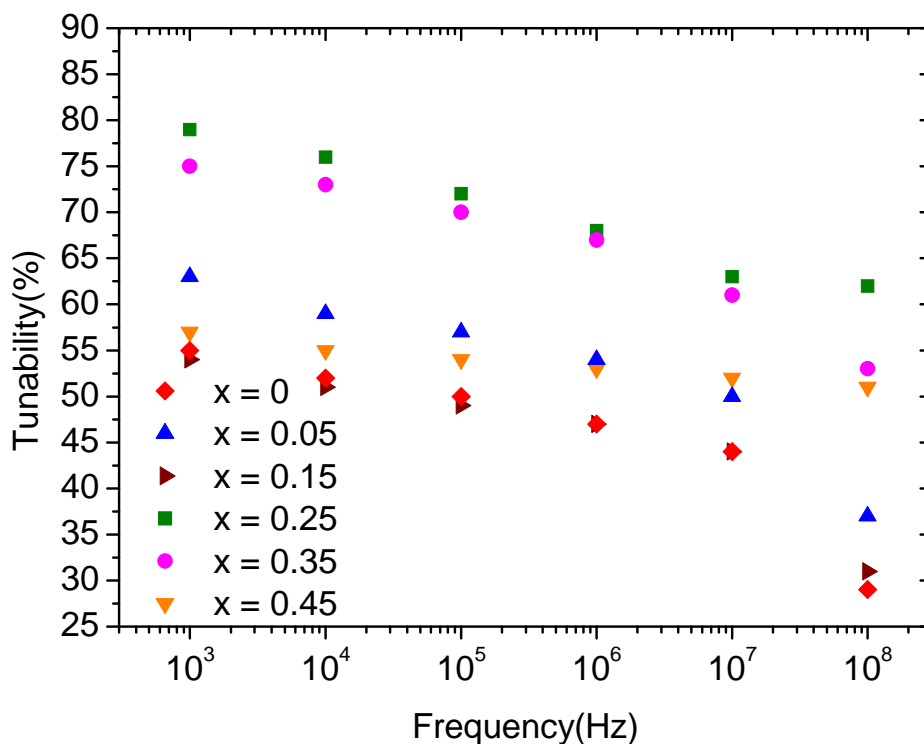


Figure 4.12 The frequency dependence of dielectric tunability $K(\%)$ of the BSZT thin films under 20MV/m.

Table 4.3 Tunability, loss tangent and figure of merit for $(\text{Ba}_{1-x}\text{Sr}_x)(\text{Zr}_{0.1}\text{Ti}_{0.9})\text{O}_3$ ($x = 0, 0.05, 0.15, 0.25, 0.35, 0.45$) grown on LSAT.

	$x = 0$	$x = 0.05$	$x = 0.15$	$x = 0.25$	$x = 0.35$	$x = 0.45$
K at 1MHz(%)	47	57	47	68	67	47
Loss at 1MHz	0.0533	0.0531	0.0445	0.1043	0.0690	0.0338
FOM	881.8	1073.4	1056.1	651.96	971.01	1390.53

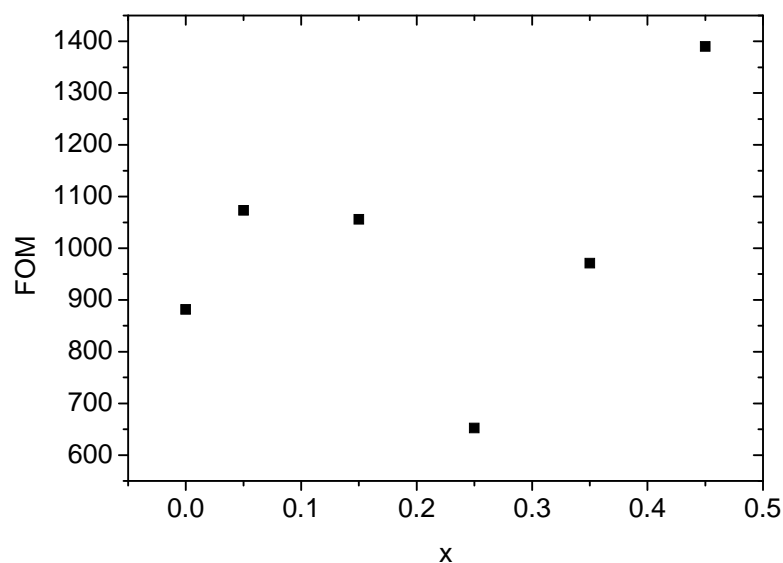


Figure 4.13 Figure of merit (FOM) as a function of compositions in

$(\text{Ba}_{1-x}\text{Sr}_x)(\text{Zr}_{0.1}\text{Ti}_{0.9})\text{O}_3$ ($x = 0, 0.05, 0.15, 0.25, 0.35, 0.45$) thin films.

In $(\text{Ba}_{0.55}\text{Sr}_{0.45})(\text{Zr}_{0.1}\text{Ti}_{0.9})\text{O}_3$ thin film, the high figure of merit is due to the lowest loss tangent. The loss tangent decreases, and hence the figure of merit (K) increases. From the AFM result, the reduction in grain size could lead to the decrease in dielectric loss and an increase in the figure of merit (FOM).

4.3.3.2 Effect of substrates

The tunability of the $(\text{Ba}_{0.55}\text{Sr}_{0.45})(\text{Zr}_{0.1}\text{Ti}_{0.9})\text{O}_3$ thin films grown on LAO and MgO have also been characterized. The tunability of the thin films on LAO and MgO are calculated to be 52% and 43% at 100MHz under electric field of the $20(\text{V}/\mu\text{m})$. The tunability is a very important indicator for microwave device applications.

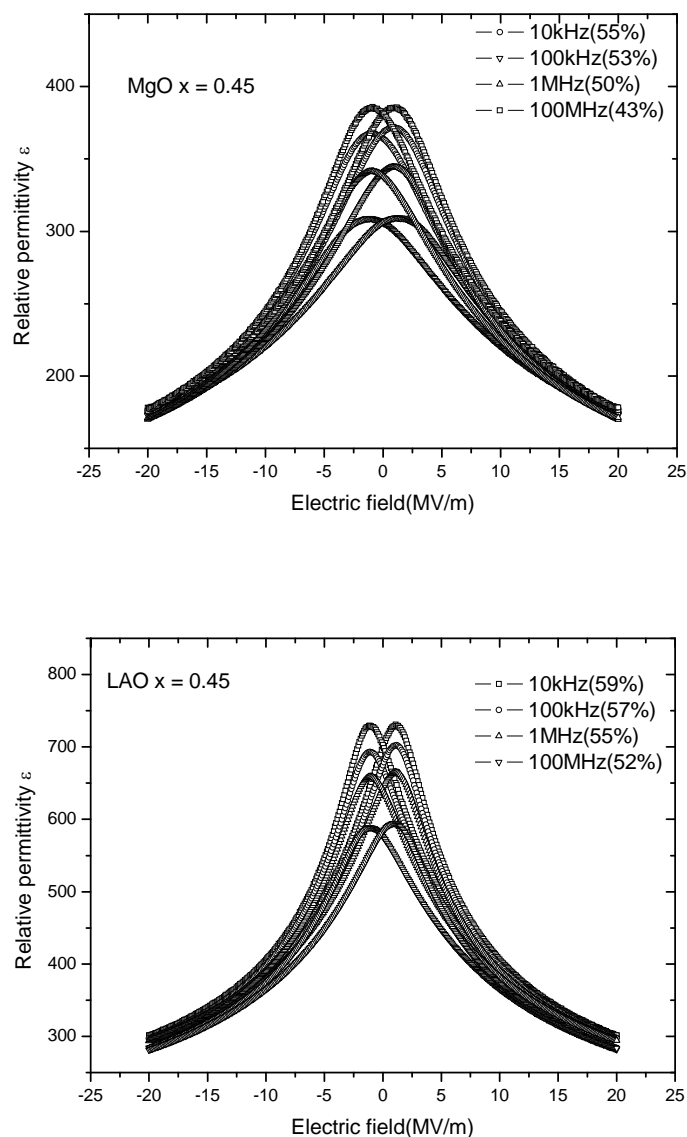


Figure 4.14 Dielectric tunability as a function of electric field for

$(\text{Ba}_{0.55}\text{Sr}_{0.45})(\text{Zr}_{0.1}\text{Ti}_{0.9})\text{O}_3$ thin films grown on LAO and MgO.

4.3.4 Hysteresis measurements

The ferroelectric hysteresis loops was measured using a TF analyzer 2000 equipped with a FE-Module (HV) (aixACCT) at room temperature.

4.3.4.1 Effect of compositions

The variation of electric polarization with applied field is shown in Figure 4.15. It is observed that the saturation polarization decreases with increasing Sr content in the films. The decrease in P_r can be attributed to two reasons, smaller grain size in Sr modified BZT thin film inhibited the formation of large ferroelectric domains, which reduced the effective contribution to total polarization. With increasing amount in Sr content, the Curie transition temperature decreases, which made the thin film exhibit paraelectric behaviour at room temperature. Thus, the polarization becomes weaker.

A linear PE curve arises due to paraelectric nature of the material. Here, with increasing Sr content in $(\text{Ba}_{0.55}\text{Sr}_{0.45})(\text{Zr}_{0.1}\text{Ti}_{0.9})\text{O}_3$, the Curie point moves to below room temperature, and hence paraelectric behaviour dominates. Table 4.4 shows the summary of the remnant polarization and the coercive field of the thin films.

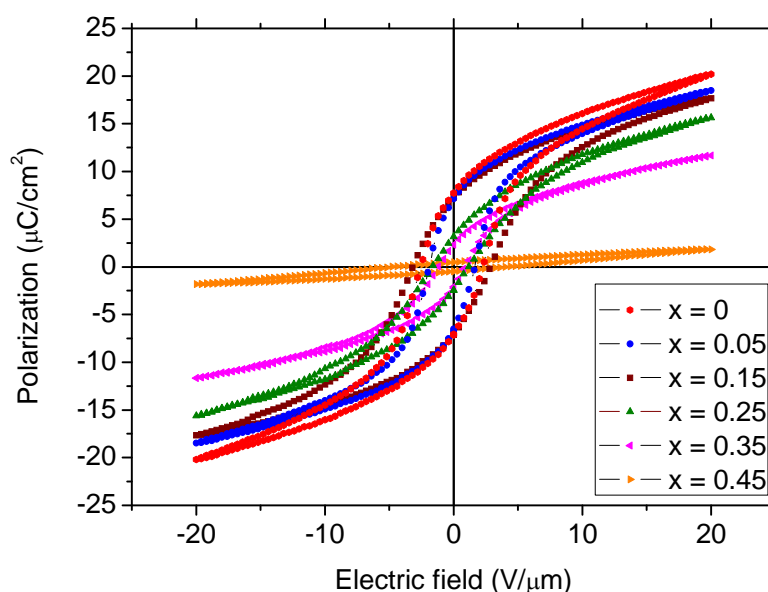


Figure 4.15 Hysteresis loops of $(\text{Ba}_{1-x}\text{Sr}_x)(\text{Zr}_{0.1}\text{Ti}_{0.9})\text{O}_3$ ($x = 0, 0.05, 0.15, 0.25, 0.35, 0.45$) thin films.



Table 4.4 The remnant polarization P_r and coercive field E_c of $(\text{Ba}_{1-x}\text{Sr}_x)(\text{Zr}_{0.1}\text{Ti}_{0.9})\text{O}_3$ with ($x = 0, 0.05, 0.15, 0.25, 0.35, 0.45$) thin films.

	x=0	x=0.05	x=0.15	x=0.25	x=0.35	x=0.45
P_r ($\mu\text{C}/\text{cm}^2$)	7.73	7.10	7.10	3.16	2.32	---
E_c (V/ μm)	2.59	1.79	2.79	1.59	1.19	---

4.3.4.2 Effect of substrates

A bulk $(\text{Ba}_{0.55}\text{Sr}_{0.45})(\text{Zr}_{0.1}\text{Ti}_{0.9})\text{O}_3$ ceramics have a cubic structure and do not show obvious hysteresis loop. Normally, the substrates will affect the measurement results in the coplanar configuration since the electric field may penetrate into the substrate. The low dielectric constant of MgO, LSAT and LAO substrate can reduce the field penetration in the substrate and the applied field can be more effective in exciting in-plane ferroelectricity of the BSZT thin films.

The hysteresis loops for $(\text{Ba}_{0.55}\text{Sr}_{0.45})(\text{Zr}_{0.1}\text{Ti}_{0.9})\text{O}_3$ thin films have been grown on different substrates under the same condition as described previously. Figure 4.16 shows the hysteresis loop. Well defined hysteresis loops were observed in thin films grown on LAO and MgO substrates and remnant polarization P_r are $4.22 \mu\text{C}/\text{cm}^2$ and $3.30 \mu\text{C}/\text{cm}^2$, respectively. In comparison with the $(\text{Ba}_{0.55}\text{Sr}_{0.45})(\text{Zr}_{0.1}\text{Ti}_{0.9})\text{O}_3$ ceramics, P_r of the films grown on LAO and MgO are significantly enhanced, which can be attributed to the increase of tetragonality. A very slim hysteresis loop was obtained for the film grown on LSAT substrate. The P_r of the film along the in-plane direction has been noticeable enhanced. As seen from the relative permittivity against temperature curve, therefore, the ferroelectric – paraelectric phase transition has already started,

and the film has lost most of its ferroelectric activity.

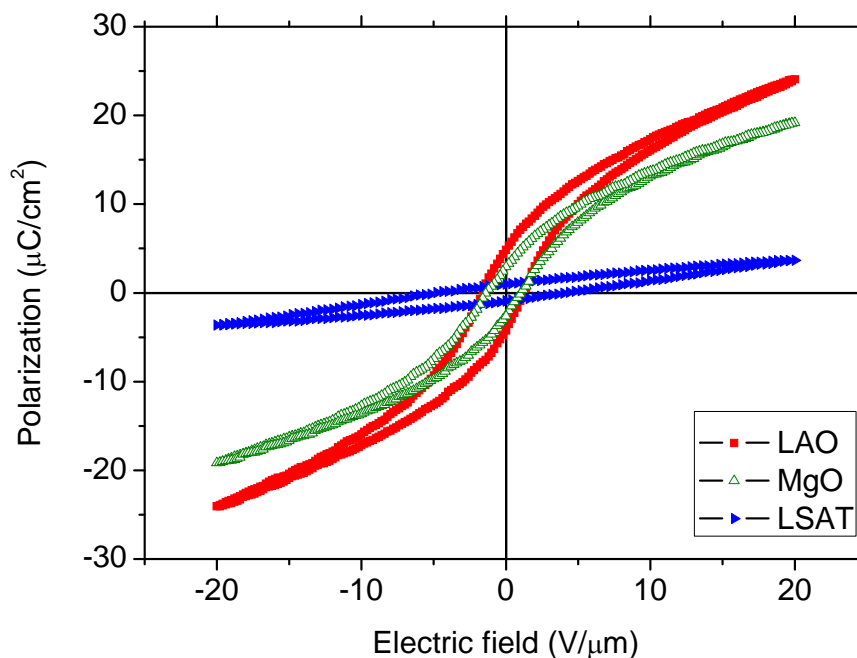


Figure 4.16 Hysteresis loop of $(\text{Ba}_{0.55}\text{Sr}_{0.45})(\text{Zr}_{0.1}\text{Ti}_{0.9})\text{O}_3$ thin films on LSAT, MgO and LAO substrates.

Table 4.5 Remnant polarization P_r and coercive field E_c of the $(\text{Ba}_{0.55}\text{Sr}_{0.45})(\text{Zr}_{0.1}\text{Ti}_{0.9})\text{O}_3$ on different substrates.

	LSAT	LAO	MgO
P_r ($\mu\text{C}/\text{cm}^2$)	---	4.22	3.30
E_c ($\text{V}/\mu\text{m}$)	---	1.58	1.39

4.3.5 Summary

The dielectric and hysteresis properties of the $(\text{Ba}_{1-x}\text{Sr}_x)(\text{Zr}_{0.1}\text{Ti}_{0.9})\text{O}_3$ ($x = 0, 0.05, 0.15, 0.25, 0.35, 0.45$) thin films were studied. The relative permittivity versus temperature and the PE loop measurement were performed in order to determine



THE HONG KONG POLYTECHNIC UNIVERSITY

whether the thin films were ferroelectric and paraelectric at room temperature. The dielectric tunabilities were also measured for these thin films. For $(\text{Ba}_{0.55}\text{Sr}_{0.45})(\text{Zr}_{0.1}\text{Ti}_{0.9})\text{O}_3$ thin film deposited on LSAT substrate, the Curie temperature is lower than room temperature ($T_c \sim 10^\circ\text{C}$) and it is in paraelectric state. The tunability of the $(\text{Ba}_{0.55}\text{Sr}_{0.45})(\text{Zr}_{0.1}\text{Ti}_{0.9})\text{O}_3$ thin film is measured to be 51% (10kHz) and 37% (100MHz), the dielectric loss (0.0338), giving a FOM of 1390, suggesting that it is a promising candidate for tunable microwave application.

$(\text{Ba}_{0.55}\text{Sr}_{0.45})(\text{Zr}_{0.1}\text{Ti}_{0.9})\text{O}_3$ thin films were also grown on different substrates under the optimum conditions, and it exhibits different ferroelectric behaviour at room temperature. The thin film grown in LAO and MgO shows significant ferroelectric activity at room temperature as the Curie temperature shifted higher ($T_c \sim 26^\circ\text{C}$ for LAO), ($T_c \sim 20^\circ\text{C}$ for MgO). Knowledge of the dielectric properties of $(\text{Ba}_{0.55}\text{Sr}_{0.45})(\text{Zr}_{0.1}\text{Ti}_{0.9})\text{O}_3$ thin film on different substrates may help us to understand its properties in the microwave regions.

**CHAPTER 5****BARIUM STRONTIUM ZIRCONATE TITANATE
THIN FILMS BASED MICROWAVE DEVICES****5.1 Introduction**

Tunable devices based on ferroelectric varactor provide the potential for MW device fabrication. In this Chapter, BSZT thin film based ring resonator and phase shifters have been fabricated and characterized. Typically, tunable phase shifters are devices where the potential of ferroelectric is demonstrated. Ideally, phase shifter provides a frequency independent differential phase shift in a specific frequency range. As discussed in Chapter 1, for some application, the loss, tuning speed, cost and the selectivity are very stringent. Dielectric properties of the ferroelectrics in MW range define the performance of the phase shifter. BSZT thin film based ring resonators have been studied also in order to characterize the dielectric properties in MW range.

Ring resonators have been fabricated to determine the dielectric properties of the $(\text{Ba}_{0.55}\text{Sr}_{0.45})(\text{Zr}_{0.1}\text{Ti}_{0.9})\text{O}_3$ thin films on different substrates at high frequency. Instead, ring resonators are versatile wavelength selective elements that can be used to synthesize a wide class of filter functions. The structure of the ring resonator is simple and has many other attractive features such as, small size, no cutoff frequency, no critical machining, good reproducibility and repeatability and low fabrication cost.

Compared with ferrite based phase shifters, ferroelectric based phase shifters have



THE HONG KONG POLYTECHNIC UNIVERSITY

low power requirement and also, the dielectric loss at microwave frequency is much lower as compared to semiconductor based phase shifters.

This Chapter deals with the characterization of the phase shifter based on the optimized $(\text{Ba}_{0.55}\text{Sr}_{0.45})(\text{Zr}_{0.1}\text{Ti}_{0.9})\text{O}_3$ thin film grown on different substrates at MW frequencies.

5.2 S-parameters

In microwave design, Scattering parameters (S-parameters) are important to characterize the high frequency network. It is a set of parameters describing the scattering and reflection of travelling waves when a network is inserted into the transmission line. S-parameters are conceptually simple, analytically convenient, and capable of providing a great insight into a measurement or design problem. Instead, S-parameters are powerful in describing an electrical network. S-parameters are normally measured as a function of frequency, so when looking at the formulae for S-parameter, it is important to note what frequency is implied and that the complex gain (i.e. gain and phase) is also assumed. For this reason, S-parameters are often called complex scattering parameters.

S-parameters can be described using a scattering matrix, the matrix is a mathematical expression that quantifies how RF energy propagates through a multi-port network. The scattering matrix can be defined as:

$$(S_{11}) \quad \text{one-port network}$$

$$\begin{pmatrix} S_{11} & S_{12} \\ S_{21} & S_{22} \end{pmatrix} \text{ two-port network}$$

$$\begin{pmatrix} S_{11} & S_{12} & S_{13} \\ S_{21} & S_{22} & S_{23} \\ S_{31} & S_{13} & S_{33} \end{pmatrix} \text{ three-port network}$$

When the incident wave travels through the network, the value is multiplied by the scattering parameter, giving the resulting output value. A port is a terminal of a pair of lines. The subscripts denote the port numbers. Power, voltage and current can be considered as the form of waves travelling in both directions. The signal of the output of port 2 to the incident wave on port 1 is designated as S_{21} . For reflected waves, the signal comes in and out of the same port, hence, the S parameters for the input reflection is designated as S_{11} . Figure 5.1 shows a two port networks:

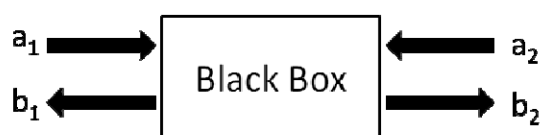


Figure 5.1 Two port electrical network.

For a two ports network,

S_{11} : reflection coefficient of the input (input match), $S_{11}=b_1/a_1$

S_{22} : reflection coefficient of the output (output match), $S_{22}=b_2/a_2$

S_{21} : forward transmission gain (gain or loss), $S_{21}=b_2/a_1$

S_{12} : reverse transmission gain (isolation), $S_{12}=b_1/a_2$

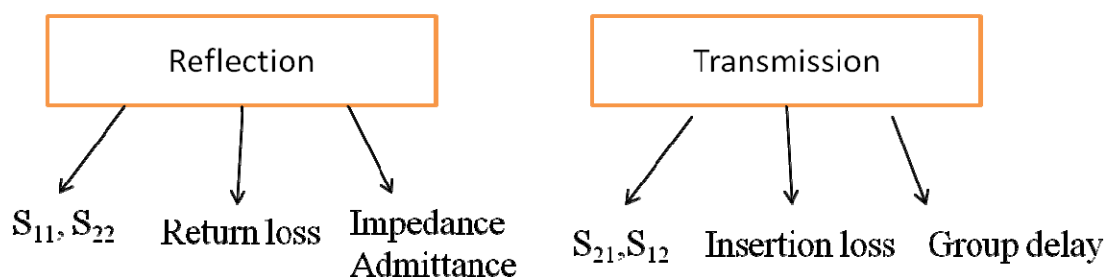


Figure 5.2 Information of S-parameters.



S-parameters are complex, they have magnitude and angles. The unit of the S parameter is dB or ratio. The unit of phases is degree or radian.

In Figure 5.1, the black box can contain anything, like resistor, transmission or an integrated circuit. S-parameter depends on the network and the characteristic impedances of the source and the load and the frequency measured at. The S parameter can be converted to impedance by taking the ratio of $(1+S_{11})$ to $(1-S_{11})$ and multiplying the result by the characteristic impedance (often 50 or 75 Ω)

5.3 Issues of microwave measurements

The characterization of device at microwave frequencies was performed by using a network analyzer 8720ES (Agilent, USA) equipped with a standard probe station Microtech RF-1 (Cascade, USA). The probe should be selected according to the device structure. In our laboratory, air coplanar Cascade ground-signal-ground (GSG) microprobes and air coplanar Cascade ground signal (GS) microprobe can be used. The tips of the microprobe is made of beryllium copper (BeCu), which are preferable to use with gold pad or copper pad as the contact substrate. Before the mounting of the probe to the probe station, the GS, GSG probes tip was cleaned using isopropyl alcohol (IPA) and air stream was blown from the probe body to the tip. After cleaning, the probe can be mounted to the probe station. Planarization of tips is to make sure all contacts are at the same height. A contact substrate (provided by the manufacturer) was used to adjust the height of the tips. The planarity positioned on the probe station was adjusted until all tops made even contact on the contact substrate. Figures 5.3 shows the photograph of the GSG probes.

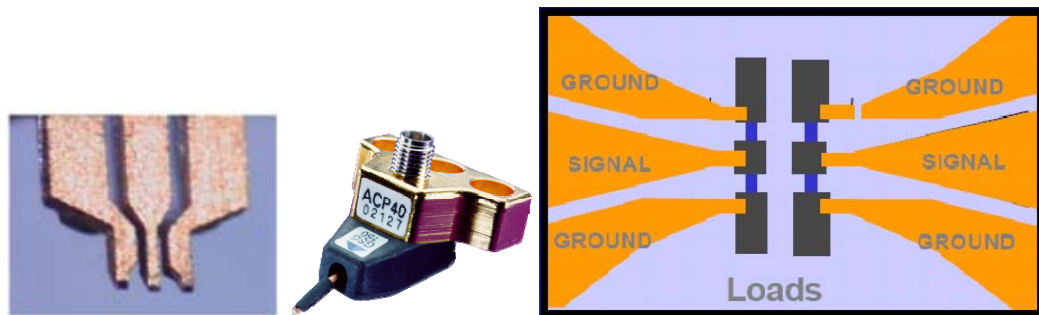


Figure 5.3 Photographs of (a) GSG probe tips, (b) GSG probes, (c) Schematic of GSG probes (C.Doan).

5.3.1 Calibration of the system

Before the measurement each time, a calibration is a must to remove the parasitic of the probes and the connection wires of the measurement system. The calibration can be divided into two parts, one port calibration or two ports calibrations. The impedance standard substrate (ISS) with “short”, “50 Ω load”, “open” and “thru”(used for two port calibration) calibration kit provided from the manufacturer was used for calibrations. In the calibrations, the automatic Cascade Mircotech calibration software “Wincal” was used. Figure 5.4 shows the calibration steps (open \rightarrow load \rightarrow short \rightarrow thru) individually.

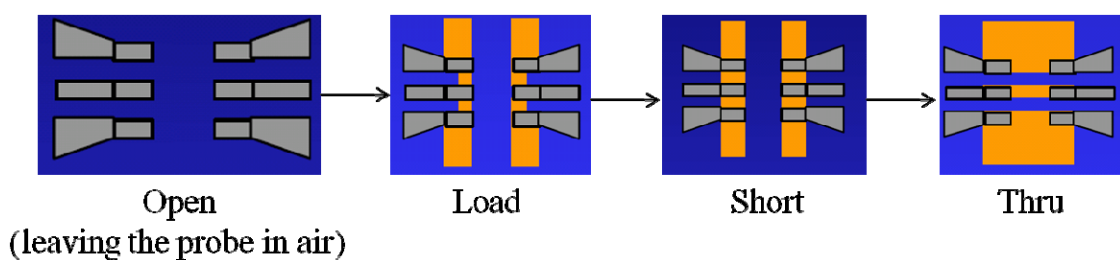


Figure 5.4 Different calibration steps: Microprobes placed on different ISS (C.Doan).



THE HONG KONG POLYTECHNIC UNIVERSITY

After the calibration, it is important to verify the performance by the following steps provided from the manufacturer.

There are two methods to verify the calibrations.

1) Verify the calibration on the open.

Using the open standard and leave it open in air. S_{11} or S_{22} should be within +/- 0.1dB or smaller.

2) Verify the calibration on 50 Ω load.

Place the probe on 50 ohm load, on the Smith chart, the impedance terminates at 50 Ω (centre of Smith chart)

5.4 Microwave characterization of the $(\text{Ba}_{0.55}\text{Sr}_{0.45})(\text{Zr}_{0.1}\text{Ti}_{0.9})\text{O}_3$ thin film on different substrates

The microwave properties of $(\text{Ba}_{0.55}\text{Sr}_{0.45})(\text{Zr}_{0.1}\text{Ti}_{0.9})\text{O}_3$ thin film on different substrates were characterized using IDC in one port network.

There is a host of sources that can contribute to insertion losses. These include the substrate, the dielectrics, and the metal electrodes. For high frequencies the insertion loss is mostly dominated by the contribution from the metal electrodes elements due to the finite resistance, and an effectively fixed and frequency independent dielectric loss tangent of the substrates. The quality factor for a device is given as the sum of the contributions from the substrate, dielectric layer, and are given by the inverse of the loss tangent, and have been experimentally shown to vary slightly with frequency(C.Doan). For the metal electrodes the quality factor is given by the inverse



THE HONG KONG POLYTECHNIC UNIVERSITY

of the product of frequency, capacitance and resistance of the electrode layer, that is, overall reduction in insertion loss can occur by reducing the overall device resistance.

$$\frac{1}{Q_{total}} = \frac{1}{Q_{subs}} + \frac{1}{Q_{BSZT}} + \frac{1}{Q_{metal}} \quad (5.1)$$

$$\frac{1}{Q_{total}} = \tan\delta_{subs} + \tan\delta_{BSZT} + \omega C_p R_s \quad (5.2)$$

Equation (5.2) shows the contribution of the quality factor from the substrate, dielectric layer and the metal electrode, where Q_t is the total device quality factor, Q_{BSZT} the dielectric quality factor, Q_m the quality factor contribution from the metallization, $\tan\delta_{subs}$ the substrate loss, $\tan\delta_{BSZT}$ the dielectric loss, ω the angular frequency, C_p the capacitance values and R_s is the series resistance.

For better understanding of the phenomenon, values of $C_p=1\text{pF}$, $\tan\delta_{subs} = 1.7 \times 10^{-4}$, $\tan\delta_{BSZT}=0.02$, $R_s=0.1\Omega$ are assumed. It can be assumed the Q_{BSZT} remains constant over the frequency range of interest as the quality factor is independent of the frequency. From Figure 5.5, it is clear that the metallization Q , i.e. Q_{total} dominates at high frequencies and has a greater effect on the overall device Q . To increase the total Q of the MW device, the resistance of the electrode should decrease by increasing the electrode thickness, however, from the microfabrication point of view, the etching of the Au electrode becomes a challenging task as thick Au layer will be detached easily. Instead of using Au as the electrodes, F.M.Vaulus (Keuls et al. 1999) uses superconducting YBCO thin film as the top electrode, in theory, the superconducting electrode give zero resistance below the transition temperature.

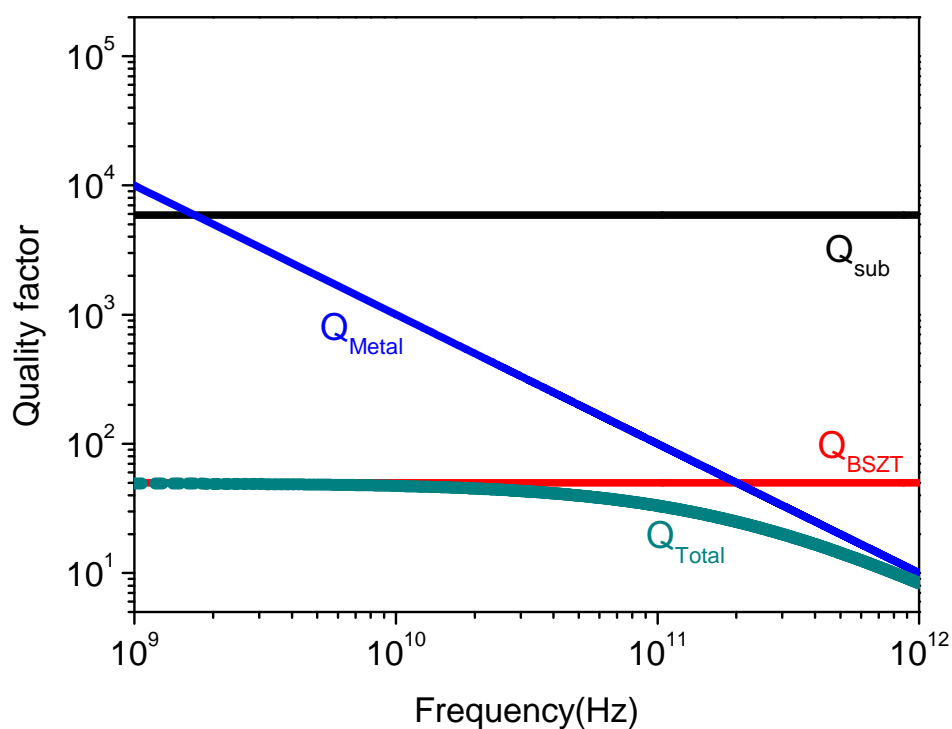


Figure 5.5 Quality factor contributions from substrate, metal and dielectrics as a function of frequency.

To further investigate this mechanisms, Figure 5.6 shows the quality factor of the $(\text{Ba}_{0.55}\text{Sr}_{0.45})(\text{Zr}_{0.1}\text{Ti}_{0.9})\text{O}_3$ thin film on LAO, LSAT and MgO substrates are studied based on the IDC configuration. All three curves give the same trends, the devices shows high Q values (30-50) at low frequency, the quality factor decreases with frequency, when the frequency reaches 10^8 Hz, the quality factor decreases to around 8. It is believed that, the decrease in the Q factor comes from the resistivity of the Au electrodes.

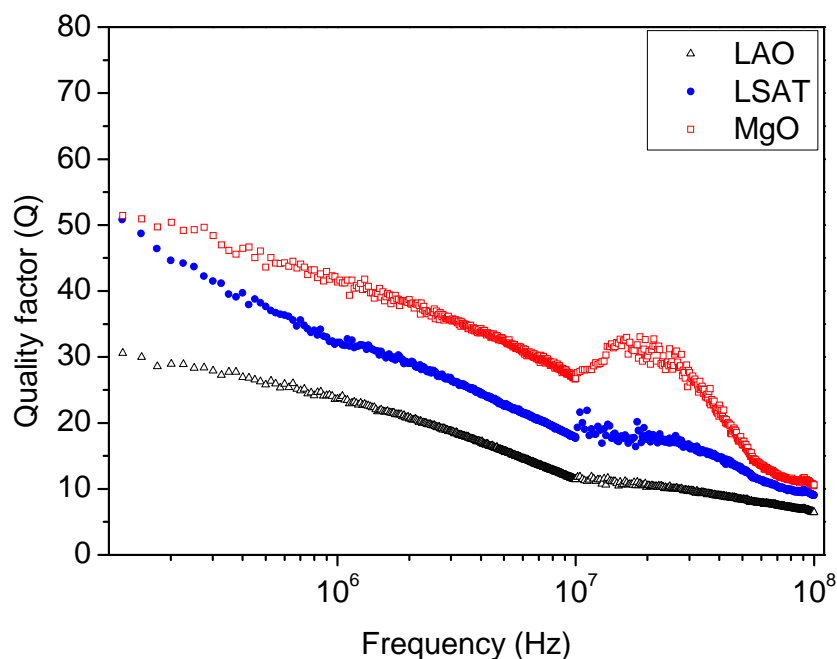


Figure 5.6 Quality factor of the $(\text{Ba}_{0.55}\text{Sr}_{0.45})(\text{Zr}_{0.1}\text{Ti}_{0.9})\text{O}_3$ thin film on different substrates.

5.5 $(\text{Ba}_{0.55}\text{Sr}_{0.45})(\text{Zr}_{0.1}\text{Ti}_{0.9})\text{O}_3$ thin film based ring resonators on different substrates

The frequency dependence of the effective dielectric constant can easily be accomplished by the use of a microstrip resonator in the form of a straight open or short ended microstrip line or a ring.

The microstrip ring resonance technique has been applied to determine the dielectric properties of $(\text{Ba}_{0.55}\text{Sr}_{0.45})(\text{Zr}_{0.1}\text{Ti}_{0.9})\text{O}_3$ thin films at high frequency in this study. The microstrip ring resonator is simple and has many other attractive features, such as small size, no critical machining, no cut off frequencies, good repeatability and



THE HONG KONG POLYTECHNIC UNIVERSITY

reproducibility and low fabrication cost.

5.5.1 Theory

The microstrip ring resonator was first proposed by P.Troughton in 1969 for measurements of the phase velocity and dispersive characteristics of a microstrip transmission line, which is composed of a strip conductor and a ground plane separated by a dielectric substrate.

Ring resonators also are useful for measurement of dispersion and wavelength in microstrip transmission lines. They do not include any discontinuity effect of either open or short circuit terminations. The ring resonator is merely a transmission line formed in a closed loop, and hence it does not suffer from open ended effects as existed in the microstrip linear resonator.

When an integral multiple of the wavelength λ_g of a guided wave equals to the mean circumference of the ring structure, resonance (maximum transmission signal) occurs. This may be expressed as:

$$2\pi r = n\lambda_g \quad \text{for } n = 1, 2, 3, \dots \quad (5.3)$$

Or

$$2\pi r = \frac{nv}{f_r} \quad (5.4)$$

where r is the mean radius of the ring, n the mode number, v the wave velocity and f_r the resonance frequency. Therefore, by the measurement of f_r , the dielectric properties of the thin films can be determined. Figure 5.7 shows the configuration of the ring resonators, it composes of grounded plane, feed line and the resonators.

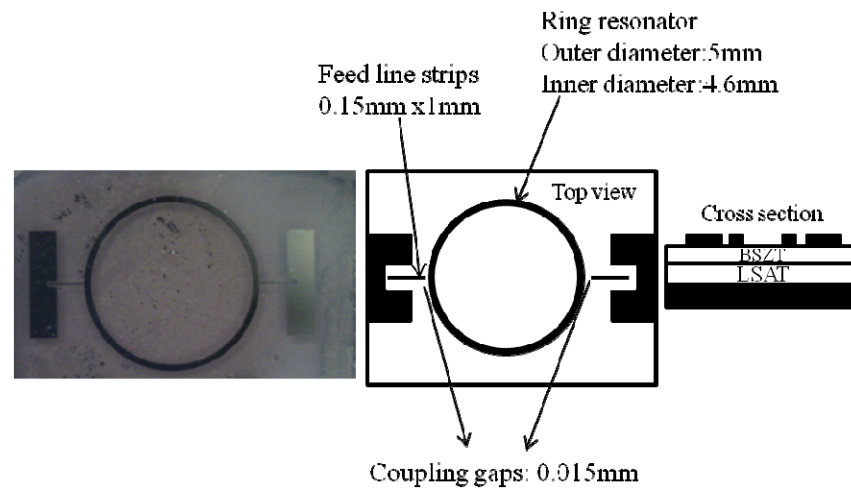


Figure 5.7 Schematic diagram of a ring resonator.

However, since the electric and magnetic field lines between the strip and the ground plate are not contained entirely in the substrate, the electric and magnetic field distribution can be viewed in Figure 5.8.

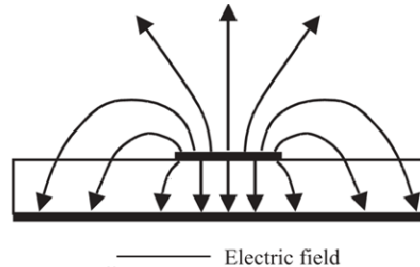


Figure 5.8 Electric field distribution on the ring resonator (Liu et al. 2004).

The propagating mode along the strip is not purely transverse electromagnetic (TEM) but quasi TEM. As a result, v is not simply inversely proportional to the square root of ϵ . Instead, it is related to the so called effective relative permittivity ϵ_{eff} , and then the equation becomes

$$2\pi r = \frac{nc}{f_r \sqrt{\epsilon_{eff}}} \quad (5.5)$$

where c is the speed of light, and ϵ_{eff} is a measure of the field confined in the region



THE HONG KONG POLYTECHNIC UNIVERSITY

underneath the strip.

The ϵ_{eff} values can be calculated using the observed f_r and

$$2\pi r = \frac{nc}{f_r \sqrt{\epsilon_{eff}}} \quad (5.6)$$

A closed form expression relating ϵ to ϵ_{eff} has been derived by Hammerstad (Hammerstad 1975) for low permittivity materials as :

$$\epsilon_{eff} = \frac{\epsilon+1}{2} + \frac{\epsilon-1}{2} \left[\left(1 + \frac{12h}{W}\right)^{-\frac{1}{2}} + 0.04 \left(1 - \frac{W}{h}\right)^2 \right] \quad (5.7)$$

where W is the width of the microstrip and h is the thickness of the substrate.

5.5.2 Ring resonators on different substrates

$(\text{Ba}_{0.55}\text{Sr}_{0.45})(\text{Zr}_{0.1}\text{Ti}_{0.9})\text{O}_3$ thin film rings were deposited on LSAT, MgO and LAO substrates by PLD. The thicknesses of the film are measured to be around 400nm. The ring resonator pattern was created by sputtering a layer of Au and then patterned by photolithography (details are shown in Chapter 4). Properties under microwave regime were measured by an Agilent 8720ES network analyzer with a pair of 150 μm pitch GSG microprobe. The transmission coefficients S_{21} were measured for the dielectric characterization. Table 5.1 shows the dimensions of the ring resonators.

Table 5.1 Dimensions of the ring resonators

Outer diameter	5mm
Inner diameter	4.6mm
Feed line strips	0.15mm x 1mm
Coupling gaps	0.015mm

For the sample with structure Au/BSZT/substrates/Au(grounding), the overall relative permittivity of the sample depends on the thin film only as the relative permittivity of the substrates are independent of frequency. Figures 5.9 – 5.11, show the transmission coefficient S_{21} as a function of frequency for the ring resonators on different substrates.

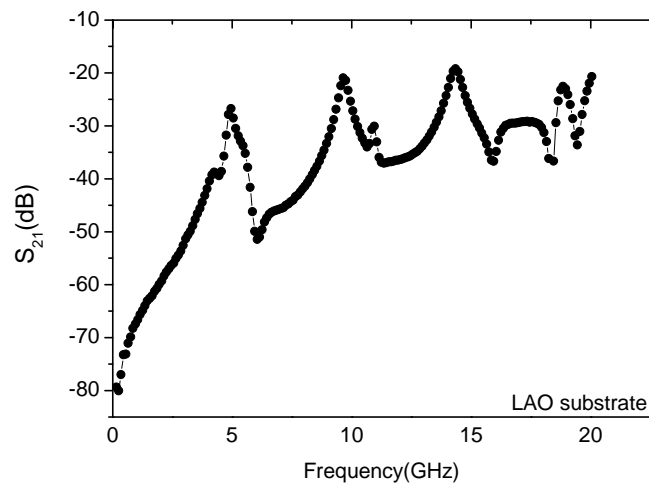


Figure 5.9 Transmission coefficient S_{21} as a function of frequency for the ring resonator on LAO substrate.

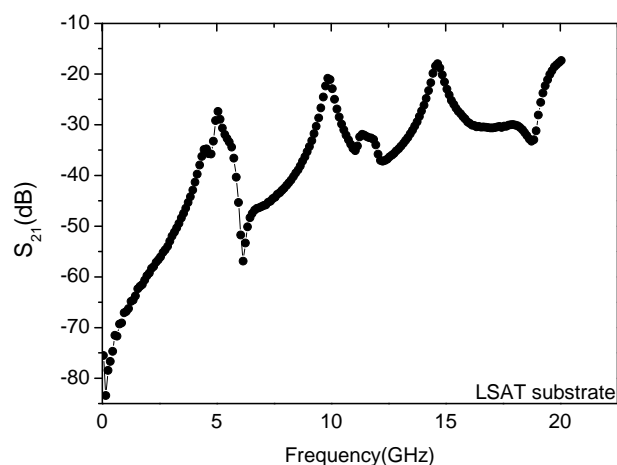


Figure 5.10 Transmission coefficient S_{21} as a function of frequency for the ring resonator on LSAT substrate.

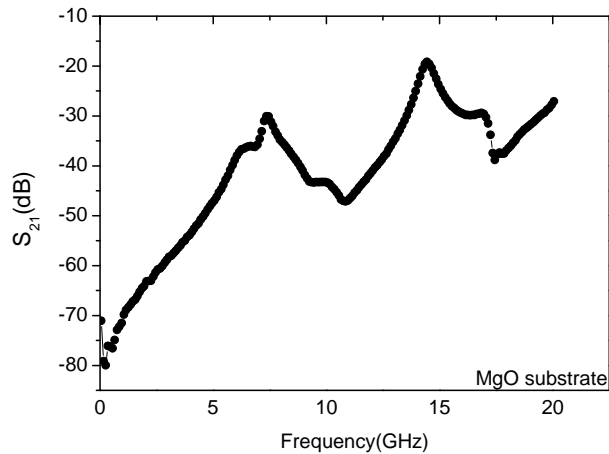


Figure 5.11 Transmission coefficient S_{21} as a function of frequency for the ring resonator on MgO substrate.

From these Figures, the resonant frequency of the ring resonator on different substrates can be obtained from the peak. For LSAT and LAO, the first resonance peaks are found to be 5.05GHz and 4.95GHz, while for MgO, the first resonance peak locates at 7.35GHz. The shape of the curves for LSAT and LAO looks similar, while the shape of the curve for MgO looks completely different compared to the other two. Since the thickness of the thin film is the same, we conclude that the difference in the shape arises from the difference in relative permittivity of the substrates.

A commercial electromagnetic simulator, Sonnet's em[®] was used to perform the full wave electromagnetic simulation. The relative permittivity of the thin film was determined by fitting the observed S_{21} spectra of the ring resonator to the simulated spectra. The software provides an open environment for many design and layout under the microwave frequency.



Table 5.2 Resonant frequencies on different substrates.

Mode number	Resonant frequency (GHz)		
	LSAT	LAO	MgO
1	5.05	4.95	7.35
2	9.85	9.65	14.45
3	14.65	14.35	-----
4	20.5	18.85	-----

The electromagnetic analysis uses a modified method of moment analysis based on Maxwell's equations to perform a true three dimensional current analysis of predominantly planar structure to compute S, Y or Z parameters, transmission line parameters (Z_0 , ϵ_{eff} and $\tan\delta$). To simulate our device performance, S_{11} and S_{21} spectra of the ring resonators were simulated. The simulated result was used to fit the experimental results in order to obtain the relative permittivity of the thin film on different substrates.

The layout of the ring resonator is drawn by AutoCAD and the files were translated to Sonnet project editor geometry format. With specific frequency range of analysis, the dielectric properties of each layer were input into the program. The circuit was subdivided into different parts to increase the speed of simulation.

From the simulation, the shape of the curves was found to be dependent on many factors, such as the relative permittivity of the thin film and substrates. The relative permittivities of the BSZT thin film on different substrates are assumed to be 350. By changing the relative permittivity of the substrates, different simulation results are

THE HONG KONG POLYTECHNIC UNIVERSITY

obtained as shown in Figures 5.11 – 5.13.

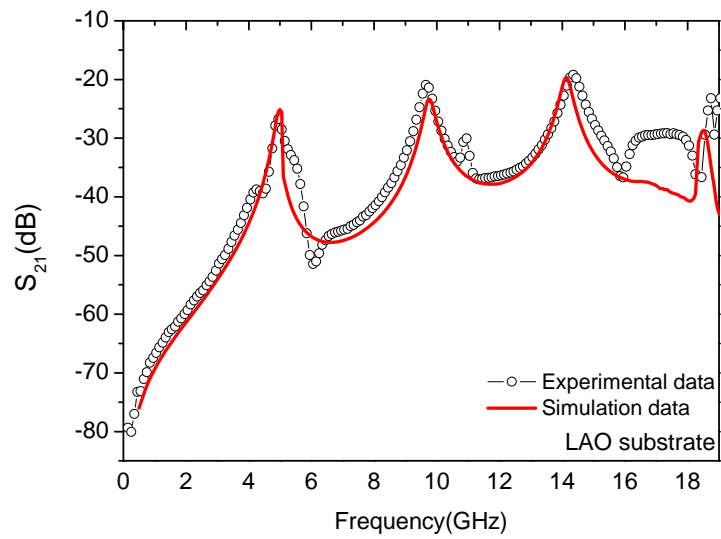


Figure 5.12 Simulation and measured result for BSZT thin film on LAO substrates.

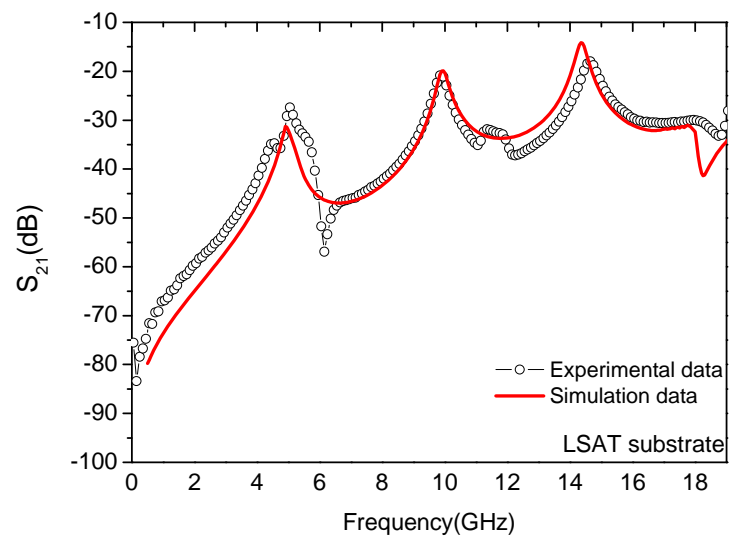


Figure 5.13 Simulation and measured result for BSZT thin film on LSAT substrates.

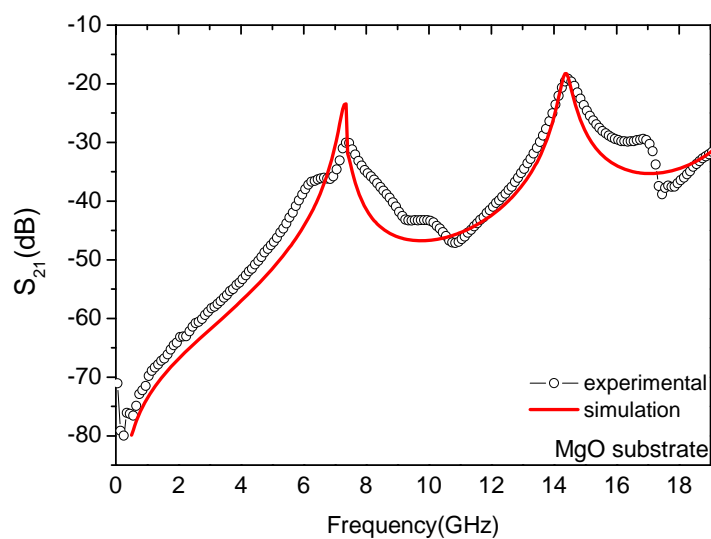


Figure 5.14 Simulation and measured result for BSZT thin film on MgO substrates.

5.6 $(\text{Ba}_{0.55}\text{Sr}_{0.45})(\text{Zr}_{0.1}\text{Ti}_{0.9})\text{O}_3$ thin film based phase shifters on different substrates

5.6.1 Introduction

Modern electronic scan phase array antenna can steer transmitted and received signals without mechanically rotating the antenna. Ferroelectric phase shifters have low power requirement as compared to the ferrite based phase shifters and also, they exhibit low loss at microwave frequencies as compared to semiconductor based phase shifters.

Phase shifters are essential in phased array antenna, radars and other microwave system. They are used for controlling the phase of the signals in microwave systems. Frequency independent phase shift in a wide frequency band, low microwave losses



THE HONG KONG POLYTECHNIC UNIVERSITY

and power consumption, high power handling capability, high tuning speed and low cost. Phase shifters with stepwise (digital), continuous (analog) and mixed digital analog tuning of the phase are considered.

Ferroelectrics based phase shifters are basically analog devices. The losses and the differential phase shift are the main parameters of the phase shifters. $(\text{Ba}_{1-x}\text{Sr}_x)\text{TiO}_3$ (BST) thin films, which is in paraelectric phase at room temperature ($x > 0.3$) are attractive candidates for tunable dielectric devices such as voltage-controlled oscillator (VCO), tunable filters, phase shifters, tunable matching network and frequency multipliers. High dielectric tunability and low dielectric loss at GHz frequency are required for microwave applications. Moreover, for impedance matching purposes the dielectric constants of the film should be low with low leakage current densities. Fabrication of phase shifter utilizing bulk BST remains unsuccessful due to high voltage requirement as well as higher relative permittivity. As discussed in Chapter 4, in thin film form the relative permittivity of the BST is low as compared to its bulk counterpart due to finer grain size as well as presence of interfacial layers. Elimination of the hysteresis in phase shift is essential in many practical microwave applications since voltage controlled oscillators and electronically steerable phase array antenna rely on accurate phase shift versus tuning voltage profiles.

To meet the low cost, energy efficient beam steering requirements, NASA in Glenn Research Centre developed phase shifters based on ferroelectrics (Miranda et al 2008, Romanofsky 2007). One of the phase shifters use coupled microstrip lines on top of about $0.4\mu\text{m}$ thick ferroelectric BST thin film. At room temperature, using Au electrodes a figure of merit $70^\circ/\text{dB}$ is demonstrated (Keuls et al. 1999). With



THE HONG KONG POLYTECHNIC UNIVERSITY

YBa₂Cu₃O_{7-x} electrodes and 2.0μm thick SrTiO₃ films, this phase shifter produces a figure of merit approaching 120°/dB at 40K (Van Keuls et al 1997). The use of YBCO instead of gold resulted in higher phase shift for the same thickness of the ferroelectric.

Most phased array antenna systems rely on ferrite. Ferrite phase shifters are slow to respond to control signals and cannot be used in applications where rapid beam scanning is required. MEMS (micro-electro-mechanical-systems) phase shifters have much faster response speeds (measure in milliseconds). However, their major drawbacks are that they have high losses at microwave frequency. Other disadvantages with MEMS phase shifters is that they have limited power handling capability (perhaps 100mW) and they may need expensive packaging to protect the movable MEMS bridges against the environment. Ferroelectric materials have the potential to overcome all the limitations of MEMS ferrite phase shifters. These circuits rely on the principle that because part or all of the microwave fields pass through the ferroelectric layer, the phase velocity of waves propagating on these structures can be altered by changing the permittivity of the ferroelectric layer.

5.6.2 Device structures and basic principle

Figure 5.14 shows the schematic representation of the eight element phase shifters. Distributed coplanar plate varactors in the form of coupled microstrip lines and Lange couplers are used in phase shifters. These devices have single pole passband filter response and provide dispersion less (flat) differential phase shift with frequency. A biasing network is also shown in the figure to apply bias voltage to each section. By applying a bias voltage between the coupled lines, one can reach large electric field

between the lines to effectively tune the relative permittivity of the ferroelectric thin film.

The propagation constant of an electromagnetic wave is a measure of the change undergone by the amplitude of the wave as it propagates in a given direction. A sketch of the coupled microstrip cross section is shown in Figure 5.15.

The propagation constant can be given by

$$\beta = \frac{\omega}{v_p} = \left(\frac{\pi}{\lambda_0}\right) \{[\varepsilon_{\text{even}}(V_{DC})]^{0.5} + [\varepsilon_{\text{odd}}(V_{DC})]^{0.5}\} \quad (5.8)$$

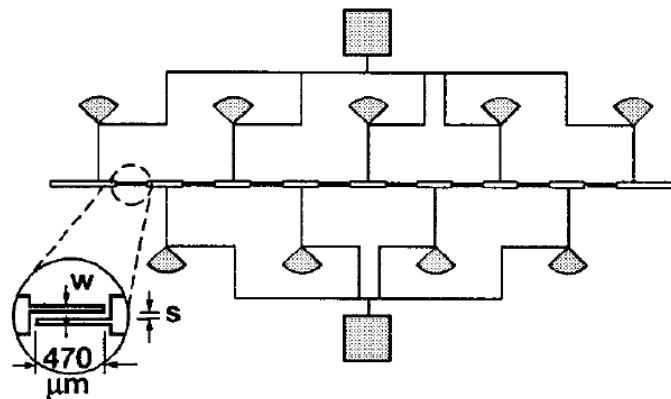


Figure 5.15 Schematic diagram of eight elements phase shifter. ($W=25\mu\text{m}$: $s=8\mu\text{m}$)

(Keuls et al. 1999).

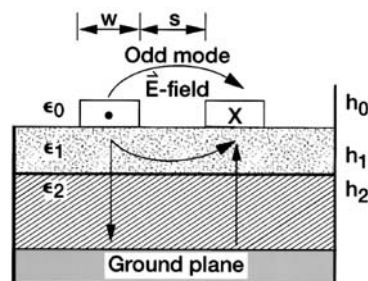


Figure 5.16 Cross section of the coupled microstripline phase shifter showing the odd mode configuration. The thickness of the ferroelectric layer is h_1 , while the host substrate has thickness h_2 .



THE HONG KONG POLYTECHNIC UNIVERSITY

where λ_0 is the free space wavelength and v_p is the phase velocity

$$\epsilon_{even} = \frac{C_e}{C_{e-air}} \quad (5.9)$$

$$\epsilon_{odd} = \frac{C_o}{C_{o-air}} \quad (5.10)$$

C_{e-air} and C_{o-air} are obtained by replacing all dielectrics with air. The ferroelectric film is most effective when the phase velocity v_p is dominated by the odd mode fields. By concentrating the field in the odd mode, the phase shift per unit length is maximized and by using the film in thin film form, the amount of phase shift can be increased by cascading coupled line sections (Romanofsky 2000).

Phase shifters are used to change the transmission phase angle (phase of S_{21}) of a network. Ideally phase shifters provide low insertion loss, high power handling, instantaneous phase change response, and approximately equal loss in all phase states. While the loss of a phase shifter is often overcome using an amplifier stage, the less the loss is, the less power that is needed to overcome it. Most phase shifters are reciprocal networks, meaning that they work effectively on signals passing in either direction.

The ferroelectric layer thickness is crucial to performance. The thicker films give greater phase shifts. However, maintaining the crystalline quality of the pulsed laser ablated film has proven to be difficult.(Romanofsky 2000) The electrode gap separation determines the degree of electromagnetic coupling and the DC potential required to tune the film.

5.6.3 Phase shifters on different substrates

The performance of the devices is measured using a HP8720ES network analyzer. The power supply 6629A Agilent with biasing voltage of 0V to 100V was used as the DC bias power source. The performance of the phase shifter was evaluated using a pair of GSG 150 μ microprobes. The performances of the phase shifter on different substrates at frequency ranges from 14GHz to 20GHz are shown in Figure 5.16 – 5.18.

The increase (decrease) of the relative permittivity of the ferroelectric layer will shift the centre frequency of the phase shifter to lower (higher) frequencies, allowing tuning of the filter.

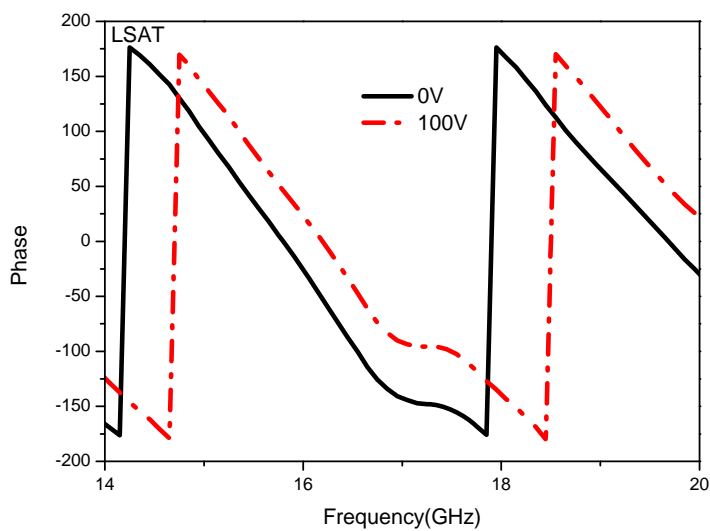


Figure 5.17 Measured S_{21} phase of the BSZT thin film based phase shifters on LSAT as a function of frequency, with two different applied biased voltages.

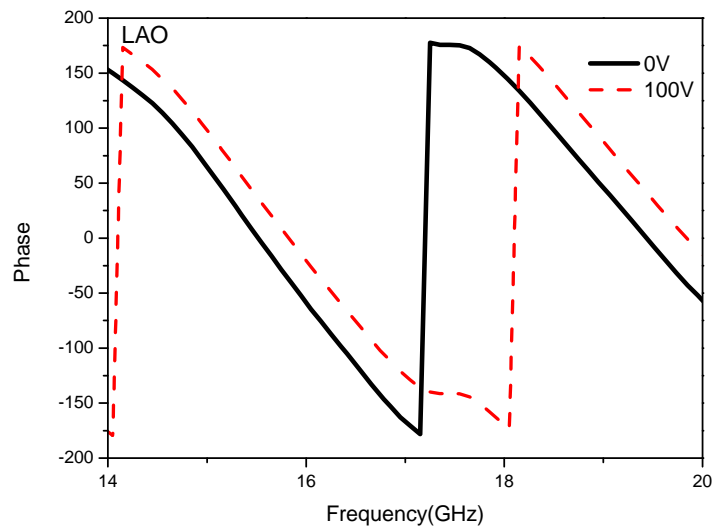


Figure 5.18 Measured S_{21} phase of the BSZT thin film based phase shifters on LAO as a function of frequency, with two different applied biased voltages.

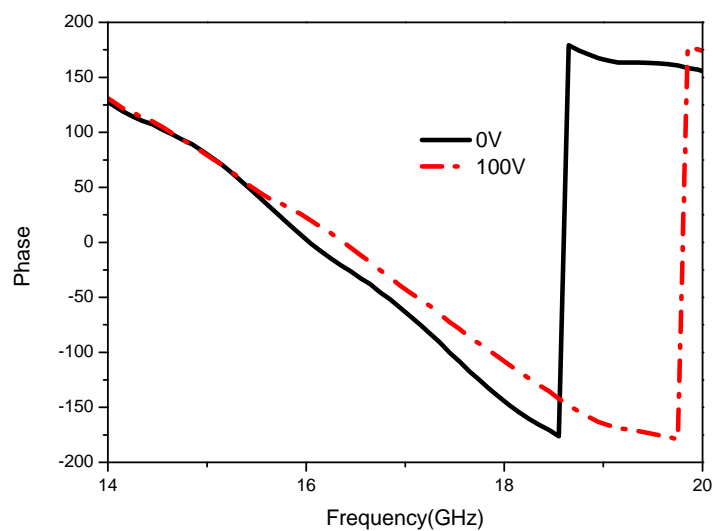


Figure 5.19 Measured S_{21} phase of the BSZT thin film based phase shifters on MgO as a function of frequency, with two different applied biased voltages.



THE HONG KONG POLYTECHNIC UNIVERSITY

The figure of merit (FOM) of the phase shifter can be defined as the quotient of differential phase shift ($\Delta\phi$) and the insertion loss α by the following equation:

$$\text{FOM} = \frac{\Delta\phi}{\alpha} \quad (5.11)$$

Table 5.3 List of operating frequency, phase shift and insertion loss of the phase shifters on different substrates.

Substrate	Operating frequency (GHz)	Differential phase shift	Insertion loss (dB)
LSAT	17.94	54°	25.1
LAO	17.25	50°	19.2
MgO	18.64	32°	20.2

Conductor losses are high in this structure due to the high dielectric constant of the ferroelectric film on which the transmission lines are fabricated.

It is noted that, the higher phase shifts in the phase shifters can be achieved by rising the DC bias voltage. Because higher electric field applied across the varactor can increase the tuning effect. However, the measurements have to be done in vacuum to protect from dielectric breakdown of the air in the large DC electric field (more than 400V) between the coupled microstrip sections.

5.7 Conclusion

In this Chapter, the IDC and ring resonator were used to investigate the dielectric properties of the $(\text{Ba}_{0.55}\text{Sr}_{0.45})(\text{Zr}_{0.1}\text{Ti}_{0.9})\text{O}_3$ thin film on different substrates. The



THE HONG KONG POLYTECHNIC UNIVERSITY

performances of the ring resonator were investigated with the aid of the commercial simulation software. The $(\text{Ba}_{0.55}\text{Sr}_{0.45})(\text{Zr}_{0.1}\text{Ti}_{0.9})\text{O}_3$ thin film based phase shifter under different DC bias were studied also. The prototype demonstrations of these components, such as small size, light weight, and low loss, as well as their demonstrated performance suggest that BSZT thin film is a potential candidate of tunable microwave applications.



CHAPTER 6

CONCLUSIONS AND SUGGESTIONS

FOR FUTURE WORK

6.1 Conclusions

The present research addresses materials engineering issues related to the integration of ferroelectric thin film into tunable microwave devices applications. In this thesis, the dielectric, ferroelectric and structural properties of $(\text{Ba}_{1-x}\text{Sr}_x)(\text{Zr}_{0.1}\text{Ti}_{0.9})\text{O}_3$ (BSZT) system in ceramics and thin film forms were studied.

BSZT ceramics were fabricated by a solid state reaction method. The structure, surface morphology, dielectric and ferroelectric properties of these ceramics were investigated. With the increase in Sr content, the following effects were observed: (1) The Curie temperature decreases linearly. (2) From the X-ray diffraction (XRD) analysis, the lattice parameter reduces. (3) Scanning electron microscopy (SEM) was used to reveal the microstructure and it was observed that the grain size decreases. (4) The polarization-electric field loop (P-E loop) shows a decrease in the remnant polarization. The piezoelectric coefficient d_{33} ($\sim 215\text{pC/N}$) and planar electromechanical coupling coefficient k_p (~ 0.271) was measured for $(\text{Ba}_{0.85}\text{Sr}_{0.15})(\text{Zr}_{0.1}\text{Ti}_{0.9})\text{O}_3$ ceramics in ferroelectric state. The BSZT ceramics has substantial tunability (more than 50% under 20kV/cm DC electric field), For $(\text{Ba}_{0.55}\text{Sr}_{0.45})(\text{Zr}_{0.1}\text{Ti}_{0.9})\text{O}_3$, figure of merit around 222.7 were calculated, which implies BSZT ceramics is a promising material for tunable microwave device applications.



Epitaxial BSZT thin films were deposited on single crystal substrates using pulsed laser deposition. Microstructures of the thin film were studied with regard to the compositional dependence by the X – ray diffraction. The thin films were grown epitaxially on the substrates. The lattice parameter of the substrate has a significant effect on the lattice parameter of the BSZT thin films. It is also found that, the lattice parameter decreases with the increase in Sr content. The a/c ratio indicates the tetragonal distortion of the films, it decreases monotonically with the increase in Sr content. As the ionic radius of Ba^{2+} (1.61Å) is larger than that of Sr^{2+} (1.44Å), more Sr^{2+} ions substituted for the Ba^{2+} ions as the Sr content increases, resulting in the decrease in lattice parameter.

The surface morphology of the films was observed using an atomic force microscope. The grain size of the thin film decreases with the increase in Sr content. $(\text{Ba}_{0.55}\text{Sr}_{0.45})(\text{Zr}_{0.1}\text{Ti}_{0.9})\text{O}_3$ films were also deposited on LSAT, LAO and MgO substrates. The roughness of the thin films on LSAT and LAO was of same order, however, the mean grains diameter of films grown on MgO is larger than that in others. This is probably due to the large lattice mismatch between the BSZT films and the MgO substrates.

The dielectric and ferroelectric properties of the BSZT thin films at room temperature were found to significantly depend on the Sr content. The Curie temperature of the thin films was measured. The Curie temperature of the thin films decreases with the increase in Sr content. PE loop measurements were performed in order to determine whether the thin films were ferroelectric and paraelectric at room temperature. In $(\text{Ba}_{0.55}\text{Sr}_{0.45})(\text{Zr}_{0.1}\text{Ti}_{0.9})\text{O}_3$ thin film deposited on LSAT substrate, the



Curie temperature is lower than room temperature ($T_c \sim 2^\circ\text{C}$) and it is in the paraelectric state.

The tunability of the $(\text{Ba}_{0.55}\text{Sr}_{0.45})(\text{Zr}_{0.1}\text{Ti}_{0.9})\text{O}_3$ thin film is measured to be 51% (10kHz) and 37% (100MHz), the dielectric loss (0.0338), resulting a FOM of 1390. For optimal performance of the tunable devices it is important to grow a material with high dielectric tunability, low dielectric losses and low voltage hysteresis, suggesting that it is a promising candidate for tunable microwave application. Beside growing $(\text{Ba}_{0.55}\text{Sr}_{0.45})(\text{Zr}_{0.1}\text{Ti}_{0.9})\text{O}_3$ thin films on LSAT substrate, $(\text{Ba}_{0.55}\text{Sr}_{0.45})(\text{Zr}_{0.1}\text{Ti}_{0.9})\text{O}_3$ thin films were also grown on MgO and LAO and the thin films exhibits different ferroelectric behaviour at room temperature. The films showed significant ferroelectric activity as the Curie temperature shifted higher.

The IDC and ring resonator were used to investigate the dielectric properties of the $(\text{Ba}_{0.55}\text{Sr}_{0.45})(\text{Zr}_{0.1}\text{Ti}_{0.9})\text{O}_3$ thin film on different substrates at microwave frequencies. The ring resonators were characterized by measuring the scattering parameter S_{21} and resonance peaks. The performance of the BSZT thin film based ring resonator on different substrates were studied with the aid of the commercial simulation Sonnet's em[®] software. Based on the S-parameter measurements and electromagnetic simulation, it was found that microwave dielectric constant of the BSZT thin film on LSAT, LAO and MgO thin films is around 350.

The $(\text{Ba}_{0.55}\text{Sr}_{0.45})(\text{Zr}_{0.1}\text{Ti}_{0.9})\text{O}_3$ thin film based phase shifter under DC bias 100V were studied also. The prototype demonstrations of these components, such as small size, light weight, and low loss, as well as their demonstrated performance suggest that



BSZT thin film is a potential candidate for tunable microwave applications.

6.2 Suggestions for Future Work

The ferroelectric thin films show great promise for microwave applications. In this work, dielectric, ferroelectric and structural properties of the BSZT thin film were studied. However, there are some suggested experiments for the future research.

- (i) An immediate attention should be given to fabricate $(\text{Ba}_{0.45}\text{Sr}_{0.55})(\text{Zr}_{0.1}\text{Ti}_{0.9})\text{O}_3$ and $(\text{Ba}_{0.35}\text{Sr}_{0.65})(\text{Zr}_{0.1}\text{Ti}_{0.9})\text{O}_3$ thin films on LSAT substrates. Investigations on these two thin films will confirm whether they can provide better tunability and lower dielectric loss.

The loss in the ferroelectric film is another important issue, especially for tunable microwave device applications. Decreasing the dielectric loss of the ferroelectric film is of crucial importance for microwave applications.

- (ii) Doping effect -- as indicated by Cui (Cui et al. 2009), in order to suppress the dielectric constant and dielectric loss of the BST ceramics, some non-ferroelectric oxides (Al_2O_3 , ZrO_2 , ZnO , MgO) may be mixed with the ceramics. The material can be also optimized by doping Mn into the ceramics to lower the dielectric loss at high frequency.
- (iii) Fabricating BSZT thin films on high-resistivity silicon substrate will be the most essential part of integration to the IC technology.



THE HONG KONG POLYTECHNIC UNIVERSITY

- (iv) To optimize the design of the phase shifter, e.g small electrode gap in the phase shifter to obtain higher electric field or apply higher electric bias (~400V) in vacuum to the phase shifter to avoid electric breakdown, which provide higher differential phase shifts.



References

A.K Tagantsev, M.Donaldson, L.Lavedan, A.Stanford and J.Pippin "A ferroelectric microwave switch "*IEEE Transactions on Micorwave Theroy and Techniques*" Vol **13**: pp. 789-793 (1965).

Ang, C., Bhalla, A. S., Guo, R. and Cross, L. E. "Dielectric loss of SrTiO₃ single crystals under direct current bias."*Applied Physics Letters*" Vol **76**(14): pp. 1929-1931 (2000).

Auciello, O., Waser, R. and North Atlantic Treaty Organization. Scientific Affairs Division. *Science and technology of electroceramic thin films*. Dordrecht ; Boston, Kluwer Academic (1995)

B.Lewis "Energy loss processes in ferroelectric ceramics."*Proceedings of the Physical Society*" Vol **73**: pp. 17-24 (1959).

Bera, J. and Rout, S. K. "Synthesis of (Ba_{1-x}Sr_x)(Ti_{0.5}Zr_{0.5})O₃ ceramics and effect of Sr content on room temperature dielectric properties."*Journal of Electroceramics*" Vol **18**(1-2): pp. 33-37 (2007).

C.Doan. "Introdcution to on wafer characterization at microwave frequencies." from http://www.macs.ece.mcgill.ca/~ktsang/downloads/On-Wafer_Characterization.pdf.



THE HONG KONG POLYTECHNIC UNIVERSITY

C.Kittel "Domain boundary motion in ferroelectric crystals and the dielectric constant at high frequency." *Physical Review* Vol **83**: pp. 458 (1951).

Canedy, C. L., Li, H., Alpay, S. P., Salamanca-Riba, L., Roytburd, A. L. and Ramesh, R. "Dielectric properties in heteroepitaxial $\text{Ba}_{0.6}\text{Sr}_{0.4}\text{TiO}_3$ thin films: Effect of internal stresses and dislocation-type defects." *Applied Physics Letters* Vol **77**(11): pp. 1695-1697 (2000).

Chen, C. L., Shen, J., Chen, S. Y., Luo, G. P., Chu, C. W., Miranda, F. A., Van Keuls, F. W., Jiang, J. C., Meletis, E. I. and Chang, H. Y. "Epitaxial growth of dielectric $\text{Ba}_{0.6}\text{Sr}_{0.4}\text{TiO}_3$ thin film on MgO for room temperature microwave phase shifters." *Applied Physics Letters* Vol **78**(5): pp. 652-654 (2001).

Chen, H. W., Yang, C. R., Fu, C. L., Shi, J., Zhang, J. H. and Leng, W. J. "Microstructure and dielectric properties of $\text{BaZr}_x\text{Ti}_{1-x}\text{O}_3$ ceramics." *Journal of Materials Science-Materials in Electronics* Vol **19**(4): pp. 379-382 (2008).

Chen, J. H., Lia, C. L., Urban, K. and Chen, C. L. "Unusual lattice distortion in a $\text{Ba}_{0.5}\text{Sr}_{0.5}\text{TiO}_3$ thin film on a LaAlO_3 substrate." *Applied Physics Letters* Vol **81**(7): pp. 1291-1293 (2002).

Chen, K. H., Chang, C. H., Chen, Y. C. and Wang, C. M. "The electrical characteristics of the $(\text{Ba}_{0.7}\text{Sr}_{0.3})(\text{Ti}_{0.9}\text{Zr}_{0.1})\text{O}_3$ thin film using oxygen plasma surface treatment." *2004 14th IEEE International Symposium on Applications of Ferroelectrics-ISAF-04* Vol: pp. 173-176, 335 (2004).



THE HONG KONG POLYTECHNIC UNIVERSITY

Chen, K. H., Tsai, Y. Z., Chen, Y. C. and Wang, C. J. "Dielectric and electrical characteristics of the barium strontium titanate zirconium thin film by RF sputtering." *Integrated Ferroelectrics* Vol **61**: pp. 129-132 (2004).

Cheng, B. L., Wang, C., Wang, S. Y., Lu, H. B., Zhou, Y. L., Chen, Z. H. and Yang, G. Z. "Dielectric properties of $(\text{Ba}_{0.8}\text{Sr}_{0.2})(\text{Zr}_x\text{Ti}_{1-x})\text{O}_3$ thin films grown by pulsed-laser deposition." *Journal of the European Ceramic Society* Vol **25**(12): pp. 2295-2298 (2005).

Cheng, H. F. "Structural and optical properties of laser deposited ferroelectric $(\text{Sr}_{0.2}\text{Ba}_{0.8})\text{TiO}_3$ thin films." *Journal of Applied Physics* Vol **79**(10): pp. 7965-7971 (1996).

Cheng, W. X., Ding, A. L., He, X. Y., Zheng, X. S. and Qiu, P. S. "Characterization of $\text{Ba}(\text{Zr}_{0.05}\text{Ti}_{0.95})\text{O}_3$ thin film prepared by sol-gel process." *Journal of Electroceramics* Vol **16**(4): pp. 523-526 (2006).

Cheung, J. T., Morgan, P. E. D., Lowndes, D. H., Zheng, X. Y. and Breen, J. "Structural and Electrical-Properties of $\text{La}_{0.5}\text{Sr}_{0.5}\text{CoO}_3$ Epitaxial-Films." *Applied Physics Letters* Vol **62**(17): pp. 2045-2047 (1993).

Choi, K. J., Biegalski, M., Li, Y. L., Sharan, A., Schubert, J., Uecker, R., Reiche, P., Chen, Y. B., Pan, X. Q., Gopalan, V., Chen, L. Q., Schlom, D. G. and Eom, C. B. "Enhancement of ferroelectricity in strained BaTiO_3 thin films." *Science* Vol **306**(5698): pp. 1005-1009 (2004).



THE HONG KONG POLYTECHNIC UNIVERSITY

Cole, M. W., Nothwang, W. D., Hubbard, C., Ngo, E. and Ervin, M. "Low dielectric loss and enhanced tunability of $Ba_{0.6}Sr_{0.4}TiO_3$ based thin films via material compositional design and optimized film processing methods." *Journal of Applied Physics* Vol **93**(11): pp. 9218-9225 (2003).

Crystec. "LaAlO₃ for Research and Development", from <http://www.crystec.de/daten/laalo3.pdf>.

Cui, J. D., Dong, G. X., Wang, Y. and Du, J. "Microstructure and dielectric properties of BST/MZO ceramic composites for tunable microwave applications." *Journal of Materials Science-Materials in Electronics* Vol **20**(5): pp. 473-478 (2009).

Cullity, B. D. *Elements of X-ray diffraction*. Reading, Mass., Addison-Wesley Pub. Co. (1956)

Detalle, M., Nguyen, T. T., Wang, G. S. and Remiens, D. "Interfacial effects on the crystallization temperature of PMN-PT films deposited on LNO or Pt bottom electrodes." *Integrated Ferroelectrics* Vol **98**: pp. 171-182 (2008).

Dixit, A., Agrawal, D. C., Mohapatra, Y. N., Majumder, S. B. and Katiyar, R. S. "Studies on the dielectric and relaxor behavior of sol-gel derived barium strontium zirconate titanate thin films." *Materials Letters* Vol **61**(17): pp. 3685-3688 (2007).

England, P., Venkatesan, T., Wu, X. D. and Inam, A. "Granular Superconductivity in



THE HONG KONG POLYTECHNIC UNIVERSITY

$R_1\text{Ba}_2\text{Cu}_3\text{O}_7$ -Delta Thin-Films. "*Physical Review B*" Vol **38**(10): pp. 7125-7128 (1988).

Fan, Y. H., Yu, S. H., Sun, R., Li, L., Yin, Y. S. and Du, R. X. "Microstructure and electrical properties of $\text{Ba}_{0.7}\text{Sr}_{0.3}(\text{Ti}_{1-x}\text{Zr}_x)\text{O}_3$ thin films prepared on copper foils with sol-gel method." *Thin Solid Films*" Vol **518**(14): pp. 3610-3614 (2010).

Fukuda, Y., Numata, K., Aoki, K. and Nishimura, A. "Origin of dielectric relaxation observed for $\text{Ba}_{0.5}\text{Sr}_{0.5}\text{TiO}_3$ thin-film capacitor." *Japanese Journal of Applied Physics Part 1-Regular Papers Short Notes & Review Papers*" Vol **35**(9B): pp. 5178-5180 (1996).

Gao Lina, Zhai Jiwei and Xi, Y. "Dielectric properties of compositionally graded $\text{Ba}_{0.90}\text{Sr}_{0.10}\text{Zr}_x\text{Ti}_{1-x}\text{O}_3$ thin films prepared by sol-gel technique." from <http://www.paper.edu.cn> TM28.

Gao, L. N., Zhai, J. W., Yao, X. and Xu, Z. K. "Dielectric properties of heterostructured BZT thin films prepared by sol-gel technique." *Materials Letters*" Vol **62**(17-18): pp. 3198-3200 (2008).

Gerblinger, J. and Meixner, H. "Electrical-Conductivity of Sputtered Films of Strontium-Titanate." *Journal of Applied Physics*" Vol **67**(12): pp. 7453-7459 (1990).

Gevorgian, S. *Ferroelectrics in microwave devices, circuits and systems : physics, modeling, fabrication and measurements*. New York, Springer (2009)



THE HONG KONG POLYTECHNIC UNIVERSITY

Gevorgian, S. S., Martinsson, T., Linner, P. L. J. and Kollberg, E. L. "CAD models for multilayered substrate interdigital capacitors." *Ieee Transactions on Microwave Theory and Techniques* Vol **44**(6): pp. 896-904 (1996).

Glocker, D. A., Shah, S. I. and Westwood, W. D. *Handbook of thin film process technology*. Bristol, UK ; Philadelphia, Institute of Physics Pub. (1995)

Gonzalo, J. A. and Jiménez, B. *Ferroelectricity: The fundamental collection*. Weinheim, Germany:, Wiley-VCH Verlag GmbH & Co. (2005)

Ha, J. Y., Choi, J. W., Kang, C. Y., Kim, J. S., Yoon, S. J., Choi, D. J. and Kim, H. J. "Improvement of dielectric loss of (Ba,Sr)(Ti,Zr)O₃ ferroelectrics for tunable devices." *Journal of the European Ceramic Society* Vol **27**(8-9): pp. 2747-2751 (2007).

Ha, J. Y., Kang, C. Y., Choi, J. W., Sim, S. H., Karmanenko, S. F., Yoon, S. J. and Kim, H. J. "Improvement in tunability and dielectric loss of BSTZ ferroelectric thin films using post-annealing." *Integrated Ferroelectrics* Vol **86**: pp. 85-94 (2006).

Haeni, J. H., Irvin, P., Chang, W., Uecker, R., Reiche, P., Li, Y. L., Choudhury, S., Tian, W., Hawley, M. E., Craigo, B., Tagantsev, A. K., Pan, X. Q., Streiffner, S. K., Chen, L. Q., Kirchoefer, S. W., Levy, J. and Schlom, D. G. "Room-temperature ferroelectricity in strained SrTiO₃." *Nature* Vol **430**(7001): pp. 758-761 (2004).

Hammerstad, E. "Equations for microstrip circuit design." *5th European Microwave*



THE HONG KONG POLYTECHNIC UNIVERSITY

Conference, Hamburg, West Germany, 1-4 Sept, 1975" Vol: pp. 268-272 (1975).

Hu, S. H., Hu, G. J., Meng, X. J., Wang, G. S., Sun, J. L., Guo, S. L., Chu, J. H. and Dai, N. "The grain size effect of the $\text{Pb}(\text{Zr}_{0.45}\text{Ti}_{0.55})\text{O}_3$ thin films deposited on LaNiO_3 coated silicon by modified sol-gel process." *Journal of Crystal Growth*" Vol **260**(1-2): pp. 109-114 (2004).

Ieee "IEEE Standard on piezoelectricity." *IEEE Transactions on Ultrasonics Ferroelectrics and Frequency Control*" Vol **43**(5): pp. A1-A54 (1996).

Jae-Dong Byun, Jung Il Yoon, Sahn Nahm and Kim, J. C. "Characterization of $(\text{Ba}_{0.65}\text{Sr}_{0.35})(\text{Ti}_{0.65}\text{Zr}_{0.35})\text{O}_3$ thin film." *Materials Research Bulletin*" Vol **35**: pp. 1755-1761 (2000).

Jaffe, B., Cook, W. R. and Jaffe, H. L. *Piezoelectric ceramics*. London, New York,, Academic Press (1971)

Johnson, K. M. "Variation of Dielectric Constant with Voltage in Ferroelectrics and Its Application to Parametric Devices." *Journal of Applied Physics*" Vol **33**(9): pp. 2826-2831 (1962).

Keuls, F. W. V., Romanofsky, R. R., Varaljay, N. D., Miranda, F. A., Canedy, C. L., Aggarwal, S., Venkatesan, T. and Ramesh, R. "A Ku-band gold/ $\text{Ba}_x\text{Sr}_{1-x}\text{TiO}_3/\text{LaAlO}_3$ conductor/thin-film ferroelectric microstrip line phase shifter for room-temperature communications applications" *Microwave and Optical Technology Letters*" Vol **20**(1):



THE HONG KONG POLYTECHNIC UNIVERSITY

pp. 53-56 (1999).

Kim, W. J., Chang, W., Qadri, S. B., Pond, J. M., Kirchoefer, S. W., Chrisey, D. B. and Horwitz, J. S. "Microwave properties of tetragonally distorted (Ba_{0.5}Sr_{0.5})TiO₃ thin films." *Applied Physics Letters* Vol **76**(9): pp. 1185-1187 (2000).

Kumar, M., Garg, A., Kumar, R. and Bhatnagar, M. C. "Structural, dielectric and ferroelectric study of Ba_{0.9}Sr_{0.1}Zr_xTi_{1-x}O₃ ceramics prepared by the sol-gel method." *Physica B-Condensed Matter* Vol **403**(10-11): pp. 1819-1823 (2008).

Laskar, J., Mukhopadhyay, R., Hur, Y., Lee, C. H. and Lim, K. "Reconfigurable RFICs and modules for cognitive radio." *2006 Topical Meeting on Silicon Monolithic Integrated Circuits in RF Systems, Digest of Papers* Vol: pp. 283-286, 397 (2006).

Lin, Y., Chen, X., Liu, S. W., Chen, C. L., Lee, J.-S., Li, Y., Jia, Q. X. and Bhalla, A. "Epitaxial nature and anisotropic dielectric properties of (Pb,Sr)TiO₃ thin films on NdGaO₃ substrates." *Applied Physics Letters* Vol **86**(14): pp. 142902 (2005).

Liu, J. Z., Kwok, K. W., Chan, H. L. W. and Choy, C. L. "Evaluation of the relative permittivity of Ba_xSr_{1-x}TiO₃ ceramics at microwave frequencies using microstrip ring resonators." *Applied Physics A* Vol **78**: pp. 1033-1036 (2004).

Majumder, S. B., Jain, M., Martinez, A., Katiyar, R. S., Van Keuls, F. W. and Miranda, F. A. "Sol-gel derived grain oriented barium strontium titanate thin films for phase shifter applications." *Journal of Applied Physics* Vol **90**(2): pp. 896-903 (2001).



THE HONG KONG POLYTECHNIC UNIVERSITY

Mohammed, M. S., Naik, R., Mantese, J. V., Schubring, N. W., Micheli, A. L. and Catalan, A. B. "Microstructure and ferroelectric properties of fine-grained $Ba_xSr_{1-x}TiO_3$ thin films prepared by metalorganic decomposition." *Journal of Materials Research* Vol **11**(10): pp. 2588-2593 (1996).

Moon, S. E., Ryu, H. C., Kwak, M. H., Kim, Y. T., Lee, S. J. and Kang, K. Y. "X-band phased array antenna using ferroelectric (Ba,Sr)TiO₃ coplanar waveguide phase shifter." *Etri Journal* Vol **27**(6): pp. 677-684 (2005).

Morris, V. J., Kirby, A. R. and Gunning, A. P. *Atomic force microscopy for biologists*. London, Imperial College Press (1999)

Moulson, A. J. and Herbert, J. M. *Electroceramics : materials, properties, applications*. West Sussex ; New York, Wiley (2003)

Murata. "FAQ of Monolithic Ceramic Capacitors." from <http://www.murata.com/products/capacitor/faq/mlcc/index.html>.

Nath, J., Ghosh, D., Maria, J. P., Steer, M. B., Kingon, A. and Stauf, G. T. "Microwave properties of BST thin film interdigital capacitors on low cost alumina substrates." *34th European Microwave Conference, Vols 1-3, Conference Proceedings* Vol: pp. 1497-1500, 1570 (2004).

Navi, N., Kim, H., Horwitz, J. S., Wu, H. D. and Qadri, S. B. "Anisotropic in-plane



THE HONG KONG POLYTECHNIC UNIVERSITY

strain in W-doped (Ba, Sr)TiO₃ thin films deposited by pulsed-laser deposition on (001)MgO." *Applied Physics a-Materials Science & Processing*" Vol **76**(5): pp. 841-846 (2003).

Ohki, Y. and Miyata, K. "Effect of Crystallinity on the Partial Discharge Resistance of Poly-L-Lactide." *Ceidy: 2009 Annual Report Conference on Electrical Insulation and Dielectric Phenomena*" Vol: pp. 59-62, 735 (2009).

Park, Y. I., Nagai, M., Miyayama, M. and Kudo, T. "Effect of composition on ferroelectric properties of sol-gel derived lead bismuth titanate (PbBi₄Ti₄O₁₅) thin films." *Journal of Materials Science*" Vol **36**(5): pp. 1261-1269 (2001).

Peterp. "The fourth mechanism: Space Charge Polarisation." from <http://www.theestory.com/posts/12343>.

Plessner, K. W. "Ageing of the dielectric properties of barium titanate ceramics." *Proceeding of the Physical Society*" Vol **69**: pp. 1261-1268 (1956).

Qin, W. F., Xiong, J., Zhu, J., Tang, J. L., Jie, W. J., Zhang, Y. and Li, Y. R. "Enhanced electrical properties of multilayer Ba(Zr_{0.2}Ti_{0.8})O₃/Ba_{0.6}Sr_{0.4}TiO₃/Ba(Zr_{0.2}Ti_{0.8})O₃ thin films for tunable microwave applications." *Journal of Materials Science*" Vol **43**(1): pp. 409-412 (2008).

Qin, Y. L., Jia, C. L., Urban, K., Hao, J. H. and Xi, X. X. "Dislocations in SrTiO₃ thin films grown on LaAlO₃ substrates." *Journal of Materials Research*" Vol **17**(12): pp.



THE HONG KONG POLYTECHNIC UNIVERSITY

3117-3126 (2002).

Ramesh, R., Inam, A., Chan, W. K., Wilkens, B., Myers, K., Remschmig, K., Hart, D. L. and Tarascon, J. M. "Epitaxial Cuprate Superconductor Ferroelectric Heterostructures." *Science* Vol **252**(5008): pp. 944-946 (1991).

Ramsey, G. H. A. J. B. "Vacuum Deposition of Dielectric and Semiconductor Films by a CO₂ Laser." *Applied Optics* Vol **8**: pp. 1115-1118 (1969).

Romanofsky, R., R.; Qureshi, A., H. "A Theoretical Model for Thin Film Ferroelectric Coupled Microstripline Phase Shifters." *National Aeronautics and Space Administration* Vol: pp. 209919 (2000).

Saito, Y., Takao, H., Tani, T., Nonoyama, T., Takatori, K., Homma, T., Nagaya, T. and Nakamura, M. "Lead-free piezoceramics." *Nature* Vol **432**(7013): pp. 84-87 (2004).

Sannikov, D. G. "Dispersion in ferroelectrics." *Soviet Physics JETP-USSR* Vol **14**: pp. 98-101 (1962).

Sawyer, C. B. and Tower, C. H. "Rochelle Salt as a Dielectric." *Physical Review* Vol **35**(3): pp. 269 (1930).

Sen, S. and Choudhary, R. N. P. "Impedance studies of Sr modified BaZr_{0.05}Ti_{0.95}O₃ ceramics." *Materials Chemistry and Physics* Vol **87**(2-3): pp. 256-263 (2004).



THE HONG KONG POLYTECHNIC UNIVERSITY

Seong, N. J., Yoon, S. G., Jo, Y. H., Jung, M. H., Cho, C. R., Yang, J. M., Park, D. J., Lee, J. W. and Lee, J. Y. "Intrinsic ferromagnetic properties of $Ti_{0.94}Fe_{0.06}O_2/Ti_{0.94}Mn_{0.06}O_2$ superlattice films for dilute magnetic semiconductor applications." *Applied Physics Letters* Vol **89**(16): pp. 162109 (2006).

Shaw, T. M., Suo, Z., Huang, M., Liniger, E., Laibowitz, R. B. and Baniecki, J. D. "The effect of stress on the dielectric properties of barium strontium titanate thin films." *Applied Physics Letters* Vol **75**(14): pp. 2129-2131 (1999).

Smith, H. M. and Turner, A. F. "Vacuum Deposited Thin Films Using a Ruby Laser." *Applied Optics* Vol **4**: pp. 147-148 (1969).

Springer-Verlag Numerical data and functional relationships in science and technology [electronic resource]. New series, Group III, Condensed matter: Ferroelectrics and related substances: subvolume A, Oxides, Berlin, New Yourk (2001)

Sura, "sura_electromagnetic_spectrum_full_chart." from

"http://www.sfu.ca/media-lab/archive/2007/387/Resources/Images/EM%20Spectrum/sura_electromagnetic_spectrum_full_chart.jpg."

Tagantsev Electroceramic-based MEMS: fabrication-technology and applications, Chapter 12, Permittivity, tunability and losses in ferroelectrics for reconfigurable high frequency electronics: In Setter N (Ed) Electroceramic Based MEMs, Springer (2005)



THE HONG KONG POLYTECHNIC UNIVERSITY

Tang, X. G., Wang, J. and Chan, H. L. W. "Dielectric properties of columnar-grained $(\text{Ba}_{0.75}\text{Sr}_{0.25})(\text{Zr}_{0.25}\text{Ti}_{0.75})\text{O}_3$ thin films prepared by pulsed laser deposition." *Journal of Crystal Growth* Vol **276**(3-4): pp. 453-457 (2005).

Troliermckinstry, S., Randall, C. A., Maria, J. P., Theis, C., Schlom, D. G., Shepard, J. and Yamakawa, K. "Size effects and domains in ferroelectric thin film actuators." *Ferroelectric Thin Films V* Vol **433**: pp. 363-374, 449 (1996).

Uchino, K. *Ferroelectric devices*. Boca Raton, CRC Press (2000)

Udayakumar, K. R., Schuele, P. J., Chen, J., Krupanidhi, S. B. and Cross, L. E. "Thickness-dependent electrical characteristics of lead zirconate titanate thin films." *Journal of Applied Physics* Vol **77**(8): pp. 3981-3986 (1995).

V.S Postnikov, V. S. P., S.A. And S.K. Turkov "Internal friction in ferroelectrics due to interaction of domain boundaries and point defects." *Journal of Physics and Chemistry of Solids* Vol **31**: pp. 1785-1791 (1970).

V.S Postnikov, V. S. P., S.A. Gridnev and S.K. Turko "Interaction between 90 degree domain walls and point defects of crystal lattice in ferroelectric ceramics." *Soviet Physics Solid State, USSR* Vol **10**: pp. 1267-1270 (1968).

Vendik, O. G., Hollmann, E. K., Kozyrev, A. B. and Prudan, A. M. "Ferroelectric tuning of planar and bulk microwave devices." *Journal of Superconductivity* Vol **12**(2): pp. 325-338 (1999).



Vispute, R. D., Wu, H. and Narayan, J. "High-Quality Epitaxial Aluminum Nitride Layers on Sapphire by Pulsed-Laser Deposition." *Applied Physics Letters* Vol **67**(11): pp. 1549-1551 (1995).

Wang, C., Cheng, B. L., Wang, S. Y., Lu, H. B., Zhou, Y. L., Chen, Z. H. and Yang, G. Z. "Improved dielectric properties and tunability of multilayered thin films of $(\text{Ba}_{0.80}\text{Sr}_{0.20})(\text{Ti}_{1-x}\text{Zr}_x)\text{O}_3$ with compositionally graded layer." *Applied Physics Letters* Vol **84**(5): pp. 765-767 (2004).

Wang, D. Y., Wang, Y., Zhou, X. Y., Chan, H. L. W. and Choy, C. L. "Enhanced in-plane ferroelectricity in $\text{Ba}_{0.7}\text{Sr}_{0.3}\text{TiO}_3$ thin films grown on $\text{MgO}(001)$ single-crystal substrate." *Applied Physics Letters* Vol **86**(21): pp. 212094 (2005).

Wang, Y., Chong, N., Cheng, Y. L., Chan, H. L. W. and Choy, C. L. "Dependence of capacitance on electrode configuration for ferroelectric films with interdigital electrodes." *Microelectronic Engineering* Vol **66**(1-4): pp. 880-886 (2003).

Waser, R. Nanoelectronics and information technology : advanced electronic materials and novel devices. Weinheim, Wiley-VCH (2005)

Watton, R. and Manning, P. "Ferroelectrics in uncooled thermal imaging." *Infrared Technology and Applications Xxiv, Pts 1-2* Vol **3436**: pp. 541-554, 986 (1998).

Wikipedia. "Atomic force microscope block diagram." from http://en.wikipedia.org/wiki/File:Atomic_force_microscope_block_diagram.svg.



Wu, T. B., Wu, C. M. and Chen, M. L. "Highly insulative barium zirconate-titanate thin films prepared by rf magnetron sputtering for dynamic random access memory applications." *Applied Physics Letters* Vol **69**(18): pp. 2659-2661 (1996).

Xiao, B., Avrutin, V., Liu, H. R., Rowe, E., Leach, J., Gu, X., Ozgur, U., Morkoc, H., Chang, W., Alldredge, L. M. B., Kirchoefer, S. W. and Pond, J. M. "Effect of large strain on dielectric and ferroelectric properties of $\text{Ba}_{0.5}\text{Sr}_{0.5}\text{TiO}_3$ thin films." *Applied Physics Letters* Vol **95**(1): pp. 012907 (2009).

Xiong, J. W., Zeng, B. and Cao, W. Q. "Investigation of dielectric and relaxor ferroelectric properties in $\text{Ba}(\text{Zr}_x\text{Ti}_{1-x})\text{O}_3$ ceramics." *Journal of Electroceramics* Vol **21**(1-4): pp. 124-127 (2008).

Xu, J., Zhou, D. Y., Menesklou, W. and Ivers-Tiffée, E. "Ferroelectric relaxor behavior and microwave dielectric properties of $\text{Ba}(\text{Zr}_{0.3}\text{Ti}_{0.7})\text{O}_3$ thin films grown by radio frequency magnetron sputtering." *Journal of Applied Physics* Vol **106**(7): pp. 074107 (2009).

Xu, W. C., Lam, K. H., Choy, S. H. and Chan, H. L. W. "A stepped horn transducer driven by lead-free piezoelectric ceramics." *Integrated Ferroelectrics* Vol **89**: pp. 87-93 (2007).

Yang, J., Chu, J. and Shen, M. "Analysis of diffuse phase transition and relaxorlike behaviors in $\text{Pb}_{0.5}\text{Sr}_{0.5}\text{TiO}_3$ films through dc electric-field dependence of dielectric



THE HONG KONG POLYTECHNIC UNIVERSITY

response." *Applied Physics Letters*" Vol **90**(24): pp. 242908 (2007).

Yang, L. H., Wang, G. S., Dong, X. L. and Remiens, D. "Perfectly (001)- and (111)-Oriented (Ba,Sr)TiO₃ Thin Films Sputtered on Pt/TiO_x/SiO₂/Si Without Buffer Layers." *Journal of the American Ceramic Society*" Vol **93**(2): pp. 350-352 (2010).

Ying, Z., Yun, P., Wang, D. Y., Zhou, X. Y., Song, Z. T., Feng, S. L., Wang, Y. and Chan, H. L. W. "Fine-grained BaZr_{0.2}Ti_{0.8}O₃ thin films for tunable device applications." *Journal of Applied Physics*" Vol **101**(8): pp. 086101 (2007).

Yoon, K. H., Sohn, J. H., Lee, B. D. and Kang, D. H. "Effect of LaNiO₃ interlayer on dielectric properties of (Ba_{0.5}Sr_{0.5})TiO₃ thin films deposited on differently oriented Pt electrodes." *Applied Physics Letters*" Vol **81**(26): pp. 5012-5014 (2002).

Yu, Z., Guo, R. Y. and Bhalla, A. S. "Dielectric polarization and strain behavior of Ba(Ti_{0.92}Zr_{0.08})O₃ single crystals." *Materials Letters*" Vol **57**(2): pp. 349-354 (2002).

Zhou, X. Y., Hong, J., Zheng, R. K., Chan, H. L. W., Choy, C. L. and Wang, Y. "Structure and dielectric properties of barium strontium titanate thin films grown on LSAT substrates." *Ferroelectrics*" Vol **357**: pp. 724-729 (2007).

Zhu, W. C., Cheng, J. R., Yu, S. W., Gong, J. and Meng, Z. Y. "Enhanced tunable properties of Ba_{0.6}Sr_{0.4}TiO₃ thin films grown on Pt/Ti/SiO₂/Si substrates using MgO buffer layers." *Applied Physics Letters*" Vol **90**(3) pp. 032907 (2007).